

# Antisymmetrized molecular dynamics studies for exotic clustering phenomena in neutron-rich nuclei

M. Kimura

*Department of Physics, Hokkaido University, Sapporo 060-0807, Japan and  
Nuclear Reaction Data Centre, Faculty of Science,  
Hokkaido University, Sapporo 060-0810, Japan*

T. Suhara

*Matsue College of Technology, Matsue 690-8518, Japan*

Y. Kanada-En'yo

*Department of Physics, Kyoto University, Kyoto 606-8502, Japan*

(Dated: Received: date / Revised version: date)

## Abstract

We present a review of recent works on clustering phenomena in unstable nuclei studied by antisymmetrized molecular dynamics (AMD). The AMD studies in these decades have uncovered novel types of clustering phenomena brought about by the excess neutrons. Among them, this review focuses on the molecule-like structure of unstable nuclei.

One of the earliest discussions on the clustering in unstable nuclei was made for neutron-rich Be and B isotopes. AMD calculations predicted that the ground state clustering is enhanced or reduced depending on the number of excess neutrons. Today, the experiments are confirming this prediction as the change of the proton radii. Behind this enhancement and reduction of the clustering, there are underlying shell effects called molecular- and atomic-orbits. These orbits form covalent and ionic bonding of the clusters analogous to the atomic molecules. It was found that this “molecular-orbit picture” reasonably explains the low-lying spectra of Be isotopes. The molecular-orbit picture is extended to other systems having parity asymmetric cluster cores and to the three cluster systems. O and Ne isotopes are the candidates of the former, while the  $3\alpha$  linear chains in C isotopes are the latter. For both subjects, many intensive studies are now in progress. We also pay a special attention to the observables which are the fingerprint of the clustering. In particular, we focus on the monopole and dipole transitions which are recently regarded as good probe for the clustering. We discuss how they have and will reveal the exotic clustering.

## I. INTRODUCTION

Atomic nuclei and symmetric nuclear matter have large incompressibility, and hence, both of the matter density and the energy density are kept almost constant in stable nuclei (saturation of energy and density). As a result, in addition to the single-particle excitations, the excitation modes that conserve the matter density are dominant in the low-lying states of stable nuclei, because the excitation modes which change the matter density (Fig. 1 (a)) require much larger energy. There may be two possible ways to excite nucleus without changing the matter density. The first is the fluctuation of nuclear shape (Fig. 1 (b)) known as collective vibrations and the other is the decomposition of nucleus into subunits (clusters) called clustering (Fig. 1 (c)). Based on the saturation of energy and matter densities, Ikeda threshold rule [1] (Fig. 2) tells that the cluster states should appear in the vicinity of the excitation energy required to decompose a nucleus into clusters. A variety of cluster states in stable nuclei has been studied in detail and experimentally identified up to  $A \simeq 20$  stable nuclei [2–4]. Today, the cluster models and experimental studies are verifying this picture in heavier nuclei up to the beginning of the  $pf$ -shell region [5–7].

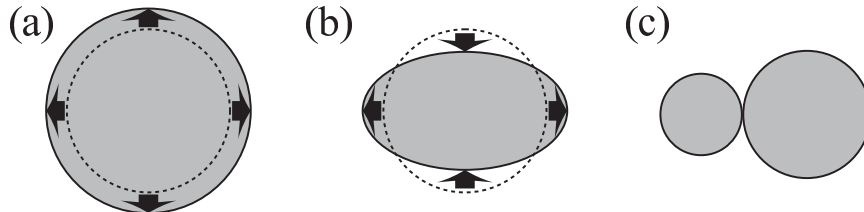


FIG. 1. (a) Nuclear excitation mode that changes the matter density. (b) Nuclear shape fluctuation and (c) Clustering are the excitation modes that conserve matter density.

In the last decades, the study of unstable nuclei has altered our basic knowledge on atomic nuclei: Both of the saturation of density and energy are broken near the neutron drip line [8, 9]. Shell structure is changed from the ordinary one and magic numbers disappear or migrate [10]. As a natural consequence, our interests to nuclear clustering are greatly renewed. Since both of the energy and matter density saturation are broken, Ikeda threshold rule cannot be straightforwardly applied to unstable nuclei and must be reconsidered. For example, an extension of Ikeda diagram to unstable nuclei called “extended Ikeda diagram” was suggested by von Oertzen [11]. Furthermore, because of the imbalance of the proton

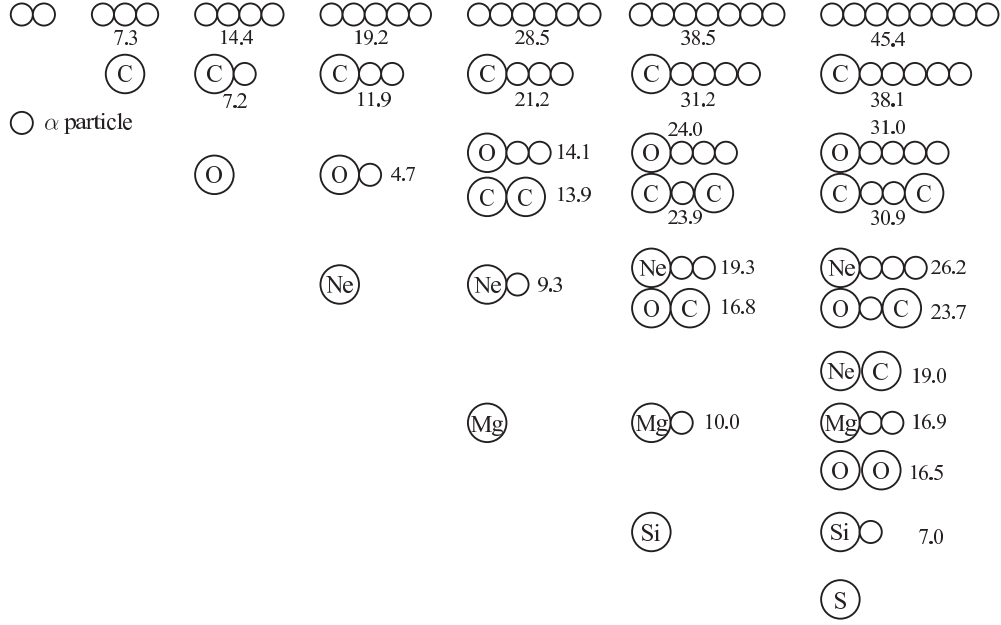


FIG. 2. Ikeda threshold rule [1] suggests that cluster states of the stable nuclei should appear approximately at the excitation energies that are required to decompose the nucleus into clusters.

and neutron numbers, the effect of the symmetry energy (difference between the proton and neutron densities) must be taken into account for the discussion of the clustering in unstable nuclei. For example, it is interesting to consider if the excess neutrons (protons) will diminish or enhance the clustering. One may consider that the clustering will be diminished to minimize the symmetry energy as illustrated in Fig. 3 (a). However, this is not the unique solution. One can also find another possibility as illustrated in Fig. 3 (b) where the nucleus is clustered to minimize the symmetry energy *locally* [12]. Thus, the evolution of the nuclear

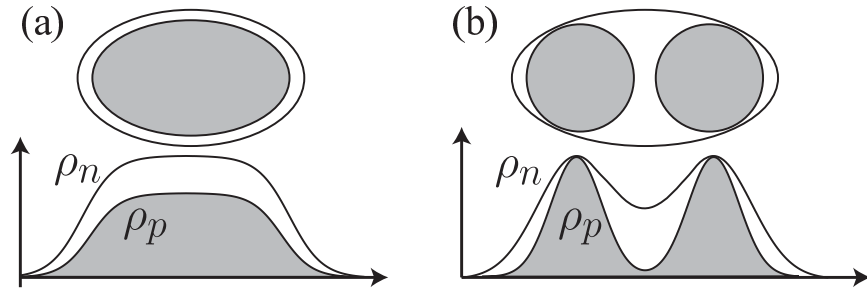


FIG. 3. (a) Density profile of neutron-rich nuclei where the symmetry energy is *globally* minimized. (b) Density profile of clustered neutron-rich nuclei where the symmetry energy is *locally* minimized.

clustering toward neutron drip line and the effect of excess neutrons to the clustering are non-trivial fascinating problems and must be examined carefully.

In the above consideration, an important ingredient, the quantum shell effect, is neglected. Since the shell structure and magic numbers are changed, the shell correction energy is different from stable nuclei and must affect the clustering of unstable nuclei. In some cases, the clustering can be enhanced with the assist of shell effect, but in some other cases it will be diminished. Furthermore, we expect that a special class of the shell structure is formed around the clustered core, which is different from the ordinary shell formed around spherical core. The possible formation of such novel type of shell structure in neutron-rich nuclei has

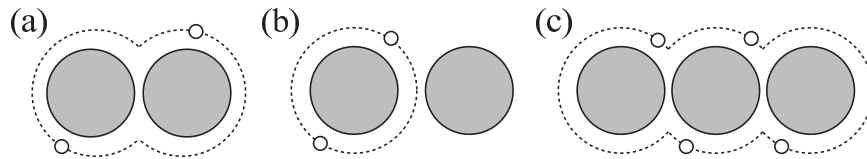


FIG. 4. (a) Molecular orbit in which excess neutron orbit around the clustered core leading to the covalent bonding of clusters. (b) Atomic orbit in which the motion of excess neutron is localized to one of clusters leading to the ionic bonding of clusters. (c) Trimer of clusters. Such exotic cluster state might be realized in neutron-rich nuclei with the assist of covalent neutrons.

long been discussed by many authors [13–18], and the orbits are, roughly speaking, classified into two types; so-called “molecular orbit” and “atomic orbit”. The former extends to the entire system leading to the covalent bonding of clusters analogous to the atomic molecules (Fig. 4 (a)), while the latter is localized to one of clusters leading to the ionic bonding of clusters (Fig. 4 (b)). With the formation of those orbits, one can imagine that very exotic cluster states which cannot be realized in stable nuclei are stabilized with the assist of excess neutrons. One such example is the linear-chain of clusters in which three or more clusters are linearly aligned (Fig. 4 (c)) [19–27]. In addition to this, formation of molecular or atomic orbits will bring about a novel type of correlations between valence neutrons. They will also yield new excitation modes where the interplay between the inter-cluster motion and excess neutrons plays the central role.

In the last decades, numerous studies have been devoted to answer those questions [17, 18, 28–30]. Today, we know that the above-mentioned phenomena do realize in many isotopes. The purpose of this article is to review those clustering phenomena in unstable nuclei from

a theoretical point-of-view provided by the studies based on antisymmetrized molecular dynamics (AMD) [28, 31–33]. The AMD studies predicted that the excess neutrons enhances the clustering in Be and B isotopes toward neutron drip line as illustrated in Fig. 3 (b), which was recently confirmed from the measurement of the proton and matter radii. A similar cluster enhancement in Ne isotopes was also predicted. Behind this enhancement of the clustering, the shell effect plays an important role. It was shown that the molecular orbits are formed in Be and Ne isotopes and it is the driving force to enhance (and reduce in some cases) the clustering. This finding is motivating the search for very exotic cluster structure of linear-chain states in neutron-rich C isotopes which is composed of linearly aligned three  $\alpha$  particles. AMD calculations predicted that the assist of the valence neutrons stabilizes the linear-chain configuration and builds a couple of rotational bands. Recently, a couple of experiments found rather convincing data for the predicted linear-chain bands in  $^{14}\text{C}$  and the discussion is going to be extended to heavier systems such as  $^{16}\text{C}$ .

This article is organized as follows. The next section gives a brief explanation of the theoretical framework of AMD on which the discussions in this review rely. In the section III, we discuss the evolution of the clustering in the ground states of light elements from Be to Ne as function of neutron number. In the section IV, the formation of molecular and atomic orbits are discussed. We first review the molecular and atomic orbits in Be and B isotopes. Then, analogous orbits in O, F and Ne isotopes are discussed. By extending the concept of molecular orbit to three cluster systems, the formation of the linear-chain configurations in C isotopes is also discussed. In the section V, we discuss the excitation modes peculiar to the clustering. We focus on the monopole and dipole excitations which are known to be sensitive to the clustering. We will see how the excess neutrons affect those excitation modes. In the last section, we summarize present status.

## II. THEORETICAL FRAMEWORK OF ANTISYMMETRIZED MOLECULAR DYNAMICS

Since AMD was firstly applied to the nuclear structure problems in 1990's [34], its framework has been continuously extended and developed. As a result, there are many different versions of AMD which are tailored for various nuclear structure and reaction problems. We here explain the most basic framework which is commonly used. The variation from this

basic framework will be explained in each section.

### A. Hamiltonian and variational wave function

In the AMD framework, we employ the microscopic  $A$ -body Hamiltonian which reads,

$$H = \sum_{i=1}^A t(i) - t_{cm} + \sum_{i<j}^A v_n(ij) + \sum_{i<j}^Z v_C(ij). \quad (1)$$

Here  $t(i)$  and  $t_{cm}$  respectively denote the kinetic energies of the  $i$ th nucleon and the center-of-mass. The center-of-mass wave function is analytically separable from the variational wave function and  $t_{cm}$  is exactly removed. Hence, the AMD framework is free from the spurious center-of-mass motion. For the nucleon-nucleon interaction  $v_n(ij)$ , various effective interactions have been utilized. In this article, the Volkov interaction [35] combined with the spin-orbit part of the G3RS interaction [36] was used in the sections III A, IV C and V B. The modified Volkov interaction [37] combined with the G3RS spin-orbit interaction was used in the sections III A, IV A, V A, and V B. The Gogny D1S interaction [38] was used in the sections III B, IV B and V A. In calculations using the Volkov and modified Volkov interactions, it is difficult to globally fit binding energies in a wide mass-number region with a fixed parametrization. Therefore, the parameters  $w$ ,  $m$ ,  $b$ , and  $h$  for the Wigner, Majorana, Bartlett, and Heisenberg terms are often modified and treated as adjustable parameters. In this article,  $w$  is set as  $w = 1 - m$ . The strength parameters  $u_1$  and  $u_2$  of the G3RS spin-orbit interaction are modified from the original values and adjusted for each central interaction to reproduce low-energy spectra. The detail of the adopted parametrization is explained in each section. The Coulomb interaction  $v_C(ij)$  is approximated by the sum of Gaussians.

The intrinsic wave function  $\Phi_{int}$  is represented by a Slater determinant of single particle wave packets,

$$\Phi_{int} = \frac{1}{\sqrt{A!}} \mathcal{A}\{\varphi_1, \varphi_2, \dots, \varphi_A\}, \quad (2)$$

where  $\varphi_i$  denotes the single nucleon wave packet expressed by a Gaussian oriented at the complex valued three dimensional vector  $\mathbf{Z}_i$ ,

$$\varphi_i(\mathbf{r}) = \left(\frac{2\nu}{\pi}\right)^{3/4} \exp\left\{-\nu\left(\mathbf{r} - \frac{\mathbf{Z}_i}{\sqrt{\nu}}\right)^2 + \frac{1}{2}Z_i^2\right\} \chi_i \xi_i. \quad (3)$$

Here  $\chi_i$  is the spinor and  $\xi_i$  is the isospin fixed to proton or neutron. The use of the Gaussian wave packets make the AMD wave function very flexible. Without any assumption for the formation of constituent clusters, multi-cluster structures can be described by the spatially localized groups of Gaussian wave packets. On the other hand, if all of the Gaussian centroids gather at the same position, the AMD wave function becomes equivalent to a harmonic oscillator shell-model wave function owing to the antisymmetrization effect. Thus, the AMD wave function is able to describe both of the shell and cluster structures in an unified way. The energy minimization explained below determines which structure, cluster or shell, is energetically favored. This advantage and feature of AMD is common to fermionic molecular dynamics (FMD) [39, 40] which also employs the Gaussian wave packets.

Instead of the spherical Gaussian, triaxially deformed Gaussian wave packet is also used as the single-particle wave packet [41],

$$\varphi_i(\mathbf{r}) = \prod_{\sigma=x,y,z} \left( \frac{2\nu_\sigma}{\pi} \right)^{1/4} \times \exp \left\{ -\nu_\sigma \left( r_\sigma - \frac{Z_{i\sigma}}{\sqrt{\nu_\sigma}} \right)^2 + \frac{1}{2} Z_{i\sigma}^2 \right\} \chi_i \xi_i. \quad (4)$$

The use of the deformed Gaussian is effective to describe the formation of the deformed mean-field in the ground states of *sd-pf*-shell nuclei.

The intrinsic wave function is projected to the eigenstate of parity and angular momentum,

$$\Phi^\pi = P^\pi \Phi_{int} = \frac{1 + \pi P_x}{2} \Phi_{int}, \quad (5)$$

$$\Phi_{MK}^{J^\pi} = P_{MK}^J \Phi^\pi = \frac{2J+1}{8\pi^2} \int d\Omega D_{MK}^{J*}(\Omega) R(\Omega) \Phi^\pi. \quad (6)$$

Here,  $P^\pi$  and  $P_{MK}^J$  are the parity and angular momentum projectors.  $D_{MK}^J(\Omega)$ ,  $P_x$  and  $R(\Omega)$  are the Wigner  $D$  function, parity and rotation operators, respectively.

## B. Energy minimization and superposition of the wave functions

The centroids of the Gaussian wave packets  $\mathbf{Z}_i$ , Gaussian width  $\nu$  and spinors  $\chi_i$  are the parameters of the variational wave function, which are determined by the energy minimization using the frictional cooling equation,

$$i\hbar \frac{d}{dt} X = (\lambda + i\mu) \frac{\partial \mathcal{H}}{\partial X^*}, \quad (7)$$



where  $X$  denotes  $\mathbf{Z}_i$ ,  $\nu$  or  $\chi_i$ .  $\lambda$  and  $\mu$  are arbitrary numbers, but  $\mu$  must have negative sign. The energy of the system  $\mathcal{H}$  is defined as

$$\mathcal{H} \equiv \begin{cases} \frac{\langle \Phi^\pi | H | \Phi^\pi \rangle}{\langle \Phi^\pi | \Phi^\pi \rangle} & \text{for VBP,} \\ \frac{\langle \Phi_{MK}^{J^\pi} | H | \Phi_{MK}^{J^\pi} \rangle}{\langle \Phi_{MK}^{J^\pi} | \Phi_{MK}^{J^\pi} \rangle} & \text{for VAP,} \end{cases} \quad (8)$$

As time  $t$  being evolved by the Eq. (7), the energy of the system is decreased and we obtain the set of parameters which minimizes the energy of the system. The calculation which employs the eigenstate of the parity  $\Phi^\pi$  to evaluate the energy is called variation before angular momentum projection (VBP), while the calculation employing the eigenstate of parity and angular momentum  $\Phi_{MK}^{J^\pi}$  is called variation after angular momentum projection (VAP) [42]. In the case of VBP, the angular momentum projection is performed after the energy minimization.

To obtain the wave functions which have the configurations different from the energy minimum, the constrained energy minimization is often performed in VBP calculations. For example, the constraint on the quadrupole deformation parameter  $\beta$  is imposed by adding the constraint potential to the energy as

$$\mathcal{H} = \frac{\langle \Phi^\pi | H | \Phi^\pi \rangle}{\langle \Phi^\pi | \Phi^\pi \rangle} + v_\beta (\langle \beta \rangle - \beta_0)^2. \quad (9)$$

Here, the magnitude of constraint potential  $v_\beta$  is chosen large enough so that the deformation parameter  $\langle \beta \rangle$  of the wave function approximately equals to  $\beta_0$  after the energy minimization. Another way to obtain the excited configurations is orthogonalization method [42] that is used in VAP calculations in which the variational wave function is orthogonalized to the energy minimum state  $\Phi_{min}$ ,

$$\tilde{\Phi}_{MK}^{J^\pi} = \Phi_{MK}^{J^\pi} - \langle \Phi_{min} | \Phi_{MK}^{J^\pi} \rangle \Phi_{min}. \quad (10)$$

By applying this procedure successively, the second, third and more excited configurations are obtained. Hereafter, the wave functions obtained by the constrained energy minimization or the orthogonalization method are denoted by  $\Phi_{MK;i}^{J^\pi}$ ,  $i = 1, 2, \dots, M$ , where  $M$  denotes the number of wave functions.

Finally, thus-obtained wave functions are superposed to take the configuration mixing into account (generator coordinate method; GCM [43]). The superposed wave function

reads

$$\Psi_{nM}^{J\pi} = \sum_{Ki} c_{Kin} \Phi_{MK;i}^{J\pi}, \quad (11)$$

where the coefficient of superposition  $c_{Kin}$  and eigenenergy  $E_n^{J\pi}$  are determined by the diagonalization of the Hamiltonian, which reduces to the generalized eigenvalue problem;

$$\sum_{Lj} H_{KiLj}^{J\pi} c_{Ljn} = E_n^{J\pi} \sum_{Lj} N_{KiLj}^{J\pi} c_{Ljn}, \quad (12)$$

$$H_{KiLj}^{J\pi} = \langle \Phi_{MK;i}^{J\pi} | H | \Phi_{ML;j}^{J\pi} \rangle, \quad (13)$$

$$N_{KiLj}^{J\pi} = \langle \Phi_{MK;i}^{J\pi} | \Phi_{ML;j}^{J\pi} \rangle. \quad (14)$$

Physical observables are calculated by using thus-obtained wave functions given in Eq. (11).

### C. Single particle levels

The single-particle configurations of a variational wave function can be investigated by the nucleon-single particle energy and orbits. In particular, it is very suggestive and useful for understanding the motion of valence neutrons in neutron-rich nuclei.

For this purpose, we construct the single-particle Hamiltonian from the intrinsic wave function obtained by the energy minimization [44]. We first transform the single particle wave packets of the intrinsic wave function  $\Phi_{int}$  to the orthonormalized basis,

$$\tilde{\varphi}_p(\mathbf{r}) = \frac{1}{\sqrt{\lambda_p}} \sum_{i=1}^A d_{ip} \varphi_i(\mathbf{r}). \quad (15)$$

Here,  $\lambda_p$  and  $d_{ip}$  are the eigenvalues and eigenvectors of the overlap matrix  $B_{ij} = \langle \varphi_i | \varphi_j \rangle$ . Using this basis, the single-particle Hamiltonian  $h_{pq}$  is constructed as,

$$\begin{aligned} h_{pq} = & \langle \tilde{\varphi}_p | t | \tilde{\varphi}_q \rangle + \sum_{r=1}^A \langle \tilde{\varphi}_p \tilde{\varphi}_r | v_n + v_C | \tilde{\varphi}_q \tilde{\varphi}_r - \tilde{\varphi}_r \tilde{\varphi}_q \rangle \\ & + \frac{1}{2} \sum_{r,s=1}^A \langle \tilde{\varphi}_r \tilde{\varphi}_s | \tilde{\varphi}_p^* \tilde{\varphi}_q \frac{\delta v_n}{\delta \rho} | \tilde{\varphi}_r \tilde{\varphi}_s - \tilde{\varphi}_s \tilde{\varphi}_r \rangle. \end{aligned} \quad (16)$$

The last term of Eq. (16) arises from the density dependent terms contained in Gogny interaction. The eigenvectors  $f_{q\alpha}$  of the single particle Hamiltonian defines the occupied

single particle orbits,

$$\begin{aligned}\phi_i(\mathbf{r}) &= \sum_{p=1}^A f_{p\alpha} \tilde{\varphi}_p(\mathbf{r}) \\ &= \sum_{i=1}^A \left( \sum_{p=1}^A d_{ip} \frac{1}{\sqrt{\lambda_p}} f_{p\alpha} \right) \varphi_i(\mathbf{r}),\end{aligned}\tag{17}$$

and the eigenvalue  $\varepsilon_p$  is the corresponding single-particle energy. In this review, we define the weakly bound neutrons as valence neutrons and remaining nucleons as the core.

### III. GROWTH OF THE GROUND STATE CLUSTERING TOWARD NEUTRON DRIP LINE

Ordinary clustering phenomena in stable nuclei are governed by the Ikeda threshold rule which is based on the saturation of the energy and density. Since these saturation properties are broken, the clustering in neutron-rich nuclei should have different aspects and obey different rule.

One of the interesting problem is the variation of the ground state clustering in an isotope chain. For example, it is well known that the ground states of  ${}^9\text{Be}$  ( $2\alpha+n$ ) and  ${}^{20}\text{Ne}$  ( $\alpha+{}^{16}\text{O}$ ) are clustered. What will happen when we add excess neutrons to these stable nuclei? AMD calculations predicted that the addition of neutrons first reduces the clustering of nuclei close to  $N = Z$  line, but then, further addition of neutrons enhances the clustering toward the neutron-drip line. Behind this enhancement of clustering, the breakdown of neutron magic numbers  $N = 8$  and  $20$  plays an important role. It also predicted that the clustering of neutron-rich B isotopes is also enhanced, although the stable nuclei  ${}^{10,11}\text{B}$  are not clustered. These predictions are experimentally supported by the recent systematic measurements of the proton radii in the isotope chains.

In this section, we summarize these AMD studies and recent data. In the section III A, we discuss how the ground state clustering in Be, B and C isotopes are varied as function of neutron number, and how it is correlated to the ground state deformation and proton, neutron and matter radii. The survey is extended to O, Ne and Mg isotopes which are discussed in the section III B.

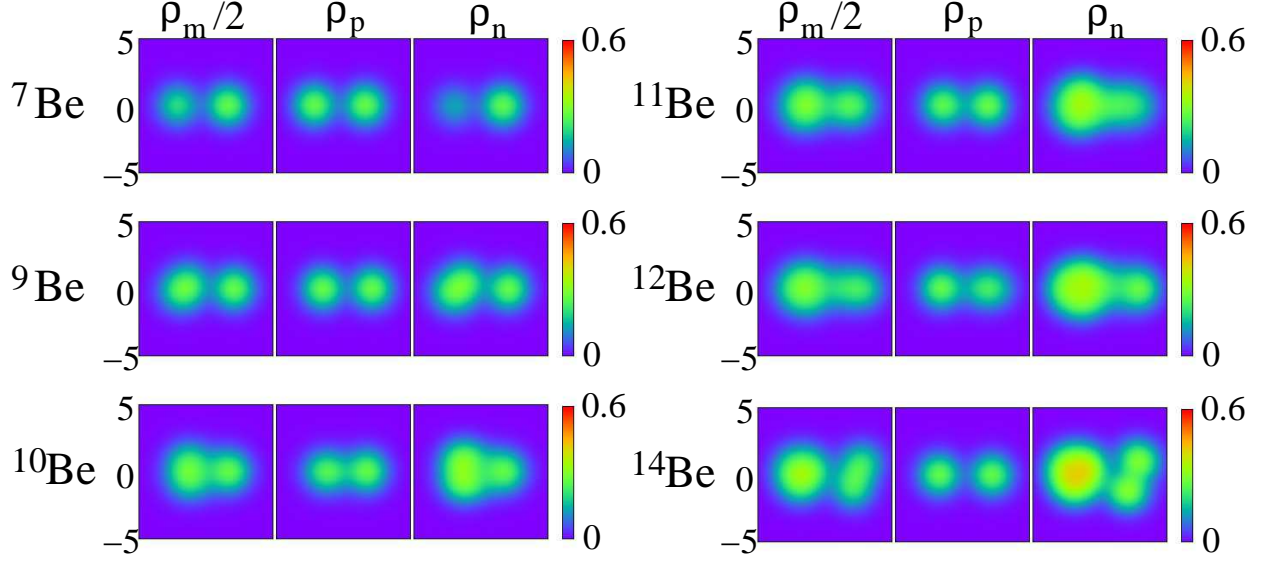


FIG. 5. (Color online) Distributions of matter (left), proton (middle), and neutron (right) densities of Be isotopes obtained by the AMD+VAP calculation using the MV1 ( $m = 0.65$ ,  $b = h = 0$ ) central and G3RS ( $u_1 = -u_2 = -3700$  MeV) spin-orbit interactions. The densities of intrinsic states are integrated with respect to the  $z$  axis and plotted on the  $x$ - $y$  plane in the unit of  $\text{fm}^{-2}$ . The axes of the intrinsic frame are chosen so as to be  $\langle x^2 \rangle \geq \langle y^2 \rangle \geq \langle z^2 \rangle$ . The figure is taken from Ref. [99].

### A. ground state clustering in Be and B isotopes

In Be isotopes, cluster structures develop in the ground and excited states [13–17, 31, 33, 44–84]. Along the series of isotopes, the cluster structure in the ground state changes rapidly depending on the neutron number  $N$ . The remarkably developed cluster structure plays an important role in the breaking of the neutron magic number  $N = 8$  in neutron-rich Be. Experimentally, the breaking of the  $N = 8$  magic number has been observed by the abnormal spin-parity  $1/2^+$  of the  $^{11}\text{Be}$  ground state and supported for  $^{12}\text{Be}$  by indirect and direct evidences [85–95]. The enhanced clustering has been theoretically predicted also in neutron-rich B isotopes such as  $^{15}\text{B}$  and  $^{17}\text{B}$  [96], whereas no development of clustering is predicted for neutron-rich C isotopes at least in the ground states [31, 97, 98]. It means that the cluster structure in the ground states sensitively depends on the neutron and proton numbers.

Figure 5 shows distributions of matter, proton, and neutron densities of the intrinsic wave functions for Be isotopes obtained by the variation after the angular-momentum and

parity projections in the framework of AMD (AMD+VAP) using the MV1 central and G3RS spin-orbit interactions [99]. The adopted interaction parameters are  $m = 0.65$ ,  $b = h = 0$ , and  $u_1 = -u_2 = -3700$  MeV, which reproduce the  $1/2_1^+$  and  $1/2_1^-$  states of  $^{11}\text{Be}$ . As seen in a dumbbell shape of proton density, the  $2\alpha$  cluster core is formed in the ground states of Be isotopes. With increase of  $N$ , the neutron structure changes rapidly. Following the rapid change of the deformation of the neutron density, the proton distribution changes showing enhancement and reduction of the  $2\alpha$  cluster structure. Namely, the  $2\alpha$  clustering is remarkably enhanced in  $^9\text{Be}$  at  $N = 5$ , but it reduces in  $^{10}\text{Be}$  because of the less deformed neutron density at  $N = 6$ . In the  $N > 6$  region, from  $^{11}\text{Be}$  to the drip-line nucleus  $^{14}\text{Be}$ , the enhanced clustering with large prolate deformations of neutron density can be seen. The largely deformed ground states of  $^{11}\text{Be}$  and  $^{12}\text{Be}$  at  $N \sim 8$  indicate the disappearance of the  $N = 8$  magic number in Be isotopes.

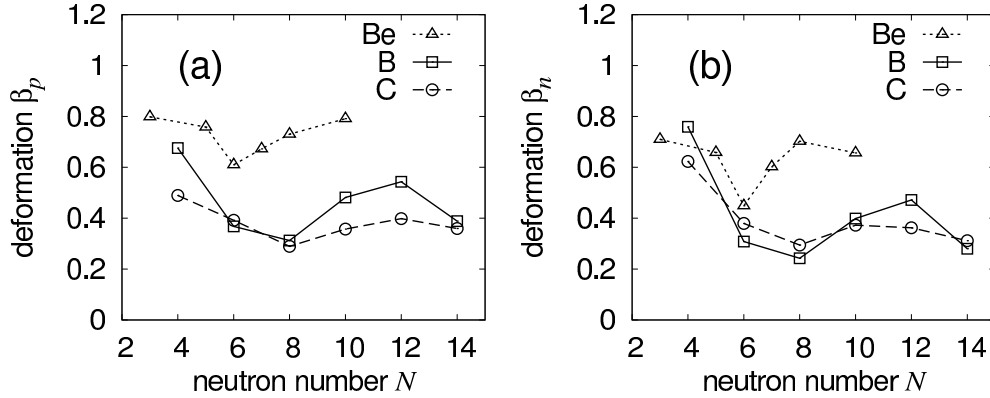


FIG. 6. Deformation parameters of Be, B, and C isotopes obtained by the AMD+VAP using the MV1 ( $m = 0.65$ ,  $b = h = 0$ ) central and G3RS ( $u_1 = -u_2 = -3700$  MeV) spin-orbit interactions for Be and B isotopes and the MV1 ( $m = 0.62$ ,  $b = h = 0$ ) central and G3RS ( $u_1 = -u_2 = -2600$  MeV) spin-orbit interactions for C isotopes.  $\beta_p(\beta_n)$  for the proton(neutron) density is shown in the left(right). The figure is modified from the original figure in Ref. [99].

For more quantitative discussion of intrinsic deformations, we show deformation parameters  $\beta_p$  and  $\beta_n$  for the proton and neutron densities in Be, B, and C isotopes calculated using the AMD+VAP in Fig. 6. The MV1 ( $m = 0.65$ ,  $b = h = 0$ ) central and G3RS ( $u_1 = -u_2 = -3700$  MeV) spin-orbit interactions are used for Be and B isotopes. For C isotopes, we use the MV1 ( $m = 0.62$ ,  $b = h = 0$ ) central and G3RS ( $u_1 = -u_2 = -2600$  MeV) spin-orbit interactions.

MeV) spin-orbit interactions which can describe systematics of the  $2_1^+$  excitation energies of C isotopes.

In Be isotopes, the neutron deformation is smallest at  $N = 6$  for  $^{10}\text{Be}$ , whereas it increases in  $^{11}\text{Be}$  and  $^{12}\text{Be}$ . Reflecting the change of the neutron deformation, the proton deformation  $\beta_p$  shows the  $N$  dependence similar to that of  $\beta_n$ . It means that, the proton deformation is smallest not at  $N = 8$  but at  $N = 6$  for  $^{10}\text{Be}$ . The coherent change of  $\beta_p$  and  $\beta_n$  indicates the enhancement and reduction of the clustering.

Also in B isotopes,  $\beta_p$  changes rapidly and shows the  $N$  dependence similar to that of  $\beta_n$  because of the enhancement and reduction of the clustering.  $\beta_p$  and  $\beta_n$  are smallest at the neutron magic number  $N = 8$  meaning the reduction of the clustering in  $^{13}\text{B}$ . This is consistent with the observed magicity of the neutron number  $N = 8$  in B isotopes differently from Be isotopes.  $^9\text{B}$  is the mirror nucleus of  $^9\text{Be}$  and has a remarkably large deformation because of the developed cluster structure. In the neutron-rich region, the deformation increases in  $^{15}\text{B}$  and  $^{17}\text{B}$  at  $N = 10$  and  $12$ , and it decreases again in  $^{19}\text{B}$  at  $N = 14$  because of the  $d_{5/2}$  sub-shell closure.

Compared with Be and B isotopes, the proton deformation in C isotopes is not so sensitive to the neutron number and no prominent clustering is seen in neutron-rich isotopes. The stability of the proton structure in the ground states of C isotopes is a feature peculiar to the proton number  $Z = 6$ , and has been discussed in relation with different deformations between proton and neutron densities in  $Z \neq N$  C isotopes [33, 98, 100].

How one can observe the structure change along the isotopes, in particular, the enhancement and reduction of the cluster structure with increase of  $N$ ? For neutron-rich B isotopes, the measurements of magnetic ( $\mu$ ) and electric quadrupole ( $Q$ ) moments have been intensively performed in 1990s [101–104]. Figure 7 shows  $\mu$  and  $Q$  moments of B isotopes. The theoretical values are those obtained by the AMD [96] and AMD+VAP calculations [99]. The  $N$  dependence of two calculations are in principle consistent with each other except for  $^{19}\text{B}$ . The calculated  $\mu$  moments reproduce well the experimental data of  $^{11-17}\text{B}$ . The deviation of  $\mu$  moments from the Schmidt value for the  $p_{3/2}$  proton is smallest at  $N = 8$  for  $^{13}\text{B}$  because of the  $N = 8$  shell closure, whereas it is relatively large for other B isotopes,  $^{11}\text{B}$ ,  $^{15}\text{B}$ , and  $^{17}\text{B}$ , because of significant contribution from the non-zero angular momentum of the core brought about by the developed clustering [96]. For the  $Q$  moments, two calculations are in reasonable agreement with the experimental values of  $^{11-17}\text{B}$ . The calculated

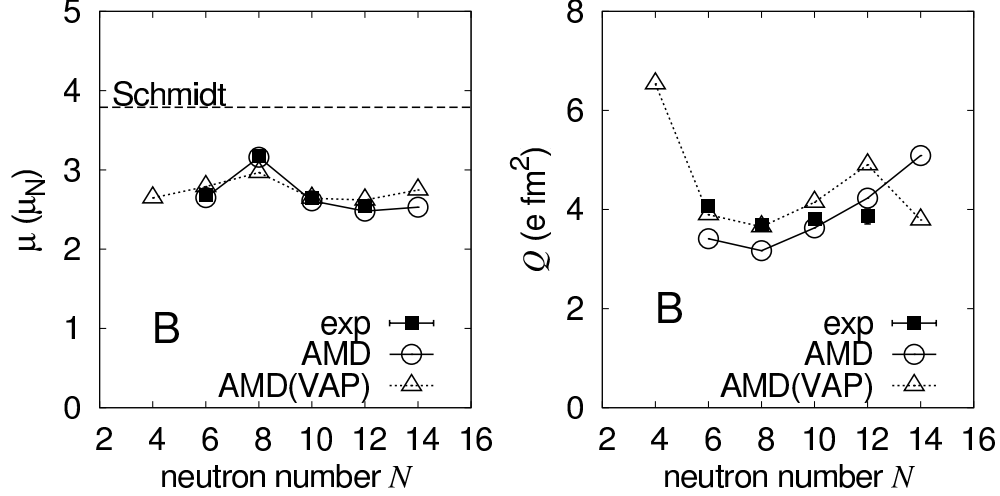


FIG. 7. The magnetic moments  $\mu$  and the electric quadrupole moments  $Q$  of B isotopes. The theoretical values calculated with the AMD in Ref. [96] and those with the AMD+VAP in Ref. [99] are shown by open circles and triangles, respectively. The dashed line in the left figure shows the Schmidt value for the  $p_{3/2}$  proton orbit. The MV1 ( $m = 0.65$ ,  $b = h = 0$ ) central and G3RS ( $u_1 = -u_2 = -3700$  MeV) spin-orbit interactions are used in the AMD+VAP calculation. For the AMD calculation, the MV1 ( $m = 0.576$ ,  $b = h = 0$ ) central interaction with mass number dependent parameters and the G3RS ( $u_1 = -u_2 = -900$  MeV) spin-orbit interaction (see Ref. [96]) are used. The experimental data shown by filled squares are taken from Refs. [101–106].

$Q$  moment is smallest at  $N = 8$  for  $^{13}\text{B}$  because of the neutron shell closure, whereas it increases in  $^{15}\text{B}$  and  $^{17}\text{B}$  because of the enhanced cluster structure. Note that, if there is no spatial development of the cluster structure, the  $Q$  moment should be largest in  $^{13}\text{B}$  and relatively small in  $^{15}\text{B}$  and  $^{17}\text{B}$  consistently with the  $N$  dependence of  $\mu$  moments as demonstrated in Ref. [96]. The experimental  $Q$  moments do not show the strong  $N$  dependence, however, slight increase of the  $Q$  moments from  $^{13}\text{B}$  to  $^{15}\text{B}$  and  $^{17}\text{B}$  might be a signature of the spatially developed clustering in  $^{15}\text{B}$  and  $^{17}\text{B}$ . For  $^{19}\text{B}$ , the simple AMD calculation in Ref. [96] suggested a prolate deformation with a remarkable clustering, whereas the latest calculation of the AMD+VAP in Ref. [99] predicted a less deformation with weak clustering. The measurement of the  $Q$  moment of  $^{19}\text{B}$  is required to determine the ground state deformation at the neutron drip line and to understand evolution of deformation (clustering) in B isotopes.

Thus, magnetic and electric moments are useful information to discuss ground state properties of odd-mass nuclei. However, they are not available for spin-zero ground states of even-even nuclei, in which moments are trivially zero. Furthermore, moments are sensitive not only to spatial development of clustering but also to the angular momentum coupling.

In contrast to the electromagnetic moments, charge radius is the observable which is directly related to the proton density distribution, and is available for both even- and odd-mass nuclei. As shown in Fig. 5, the enhancement and reduction of the cluster structure can be clearly seen in the proton density distribution. The  $N$  dependence of charge radii should reflect this change of clustering via the proton density distribution, and therefore it can be a good probe to pin down the clustering. Recently, root mean square (rms) charge radii of neutron-rich Be isotopes up to  $^{12}\text{Be}$  have been precisely measured by means of isotope shift [107, 108]. For B and C isotopes, isotope shift measurements are still limited to nuclei near the stability line. However, a new experimental approach has been recently applied to determine rms radii of point-proton density (proton radii) from charge changing interaction cross sections [109–111], and the data of proton radii of Be and B isotopes are now available.

Figure 8 shows the  $N$  dependence of proton radii in Be, B, and C isotopes combined with those of deformation parameters  $\beta_p$  and  $\beta_n$ . In Be isotopes, the proton radius is relatively large in  $^9\text{Be}$  because of the remarkable cluster structure, whereas it decreases at  $N = 6$  for  $^{10}\text{Be}$  and increases again in the  $N > 6$  region for  $^{11}\text{Be}$  and  $^{12}\text{Be}$  reflecting the reduction and enhancement with increase of  $N$ . The  $N$  dependence of proton radii is consistent with the experimental data reduced from charge radii determined by isotope shift measurements. The increase of the proton radius in  $^{12}\text{Be}$  is an experimental evidence of the  $N = 8$  shell breaking as pointed out in Ref. [108]. The  $N$  dependence of proton radii coincides with that of the proton deformation  $\beta_p$ . The minimums of  $r_p$  and  $\beta_p$  at  $N = 6$  instead of  $N = 8$  can be interpreted as the migration of the neutron magic number from  $N = 8$  to  $N = 6$  in Be isotopes.

Also in B isotopes, calculated proton radii are enhanced in  $^{15}\text{B}$  and  $^{17}\text{B}$  with the cluster development. The  $N$  dependence of the calculated proton radii is consistent with the experimental proton radii reduced from charge changing cross sections in the  $6 \leq N \leq 12$  region. For  $^{19}\text{B}$ , decrease of the proton radius was predicted by the AMD+VAP calculation because of the weak clustering.

In contrast to Be and B isotopes, calculated proton radii of C isotopes show a weaker  $N$



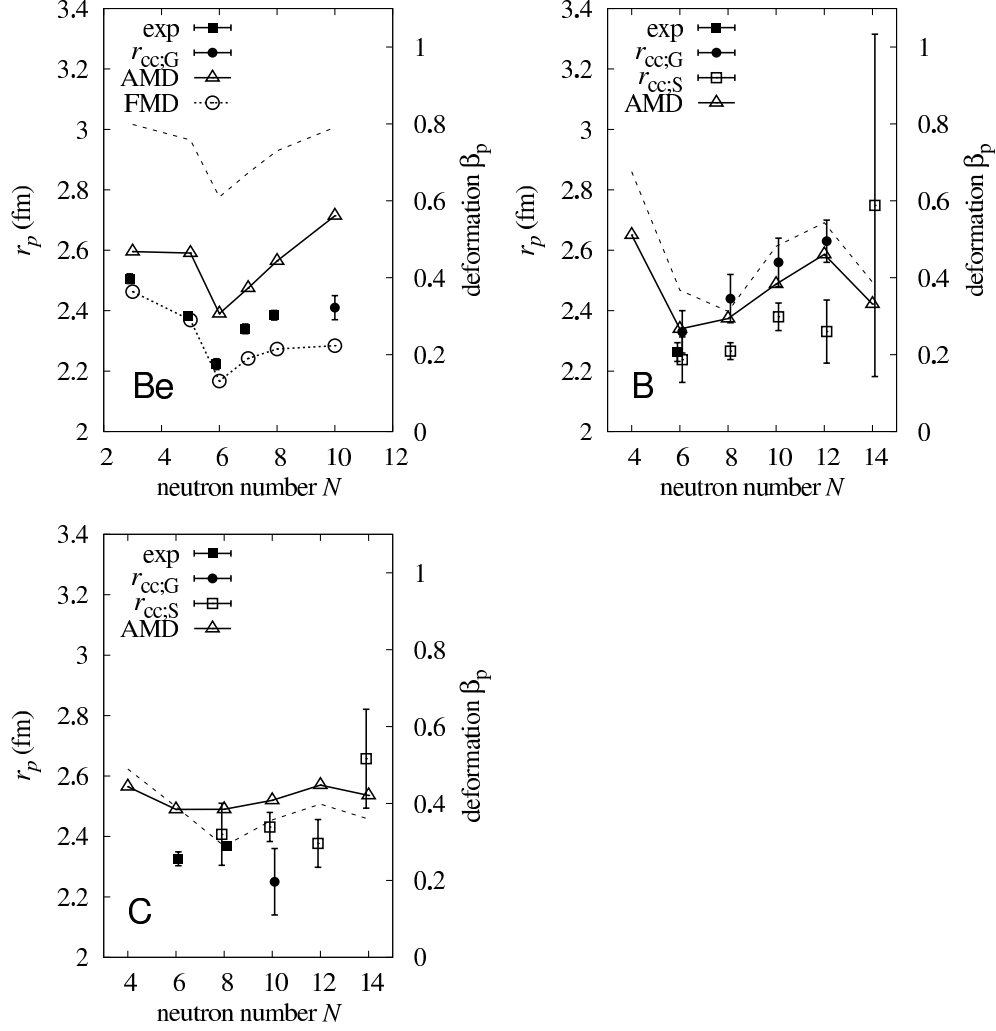


FIG. 8. Proton radii of Be, B, and C isotopes. Open triangles connected by solid lines indicate the theoretical values obtained by the AMD+VAP using the MV1 ( $m = 0.65$ ,  $b = h = 0$ ) central and G3RS ( $u_1 = -u_2 = -3700$  MeV) spin-orbit interactions for Be and B isotopes and the MV1 ( $m = 0.62$ ,  $b = h = 0$ ) central and G3RS ( $u_1 = -u_2 = -2600$  MeV) spin-orbit interactions for C isotopes. The deformation parameter ( $\beta_p$ ) of the proton density is shown by dashed lines. Experimental proton radii of  ${}^{9,10,11,12}\text{Be}$ ,  ${}^{11}\text{B}$ , and  ${}^{12,14}\text{C}$  reduced from experimental charge radii are shown by filled squares [107, 108, 112]. Experimental proton radii  $r_{\text{cc};\text{G}}$  deduced from charge changing interaction cross sections  $\sigma_{\text{cc}}$  by the Glauber analysis in Refs. [109–111] are shown by filled circles. Proton radii  $r_{\text{cc};\text{S}}$  evaluated from  $\sigma_{\text{cc}}$  in Ref. [113] using a simple ansatz are shown by open squares (see Ref. [99]). Values of FMD calculations for Be isotopes are also shown [108]. The figure is modified from the original figure in Ref. [99]

dependence. It originates in the stability of proton structure because of the less clustering in neutron-rich C isotopes. At present, the experimental data is not enough to discuss the  $N$  dependence of proton radii in the neutron-rich C isotopes.

### B. Radii and deformation of O, Ne and Mg isotopes, and the ground state clustering in Ne isotopes

As discussed for the Be, B and C isotopes, the proton and neutron radii reflect various structural characteristics such as the magnitude and pattern of deformation, the breakdown of the magic number and the formation of neutron skin or halo. In particular, the behavior of the proton radii is attributed to the enhancement and reduction of the clustering in Be and B isotopes. Therefore, it is interesting to extend the survey to heavier mass isotopes.

Ne and Mg isotopes have longer isotope chains than Be and B isotopes and are famous for the breakdown of the  $N = 20$  magic number [10, 114–116]. AMD has been also applied to the structure study of the Ne and Mg isotopes [117–119], and we here discuss what kinds of structural information can be extracted from the behavior of the proton, neutron and matter radii. We first examine how the quadrupole deformation of proton and neutron distributions shown in Fig. 9 are correlated to the behavior of the radii and reaction cross sections shown in Figs. 10 and 11.

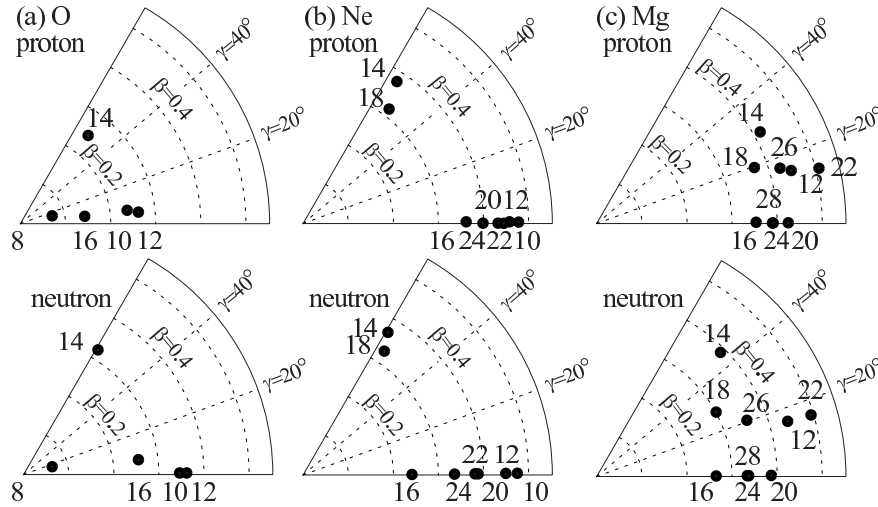


FIG. 9. Intrinsic quadrupole deformation parameters of the ground states of O, Ne and Mg isotopes obtained by AMD calculation. Numbers in the figure show neutron number.

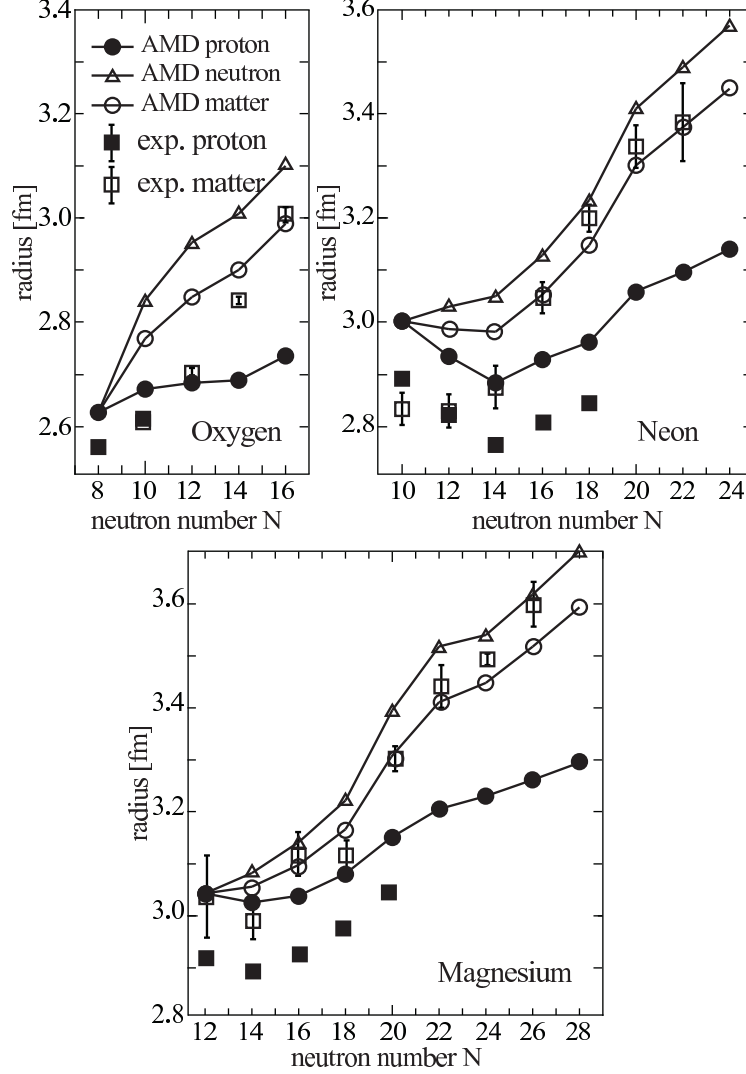


FIG. 10. Calculated and observed proton, neutron and matter radii of O, Ne and Mg isotopes. Experimental data are taken from Refs. [120–124].

The deformations of O isotopes are always small compared with Ne and Mg isotopes owing to the  $Z = 8$  proton shell closure. It is confirmed from Fig. 9 (a) that the proton deformation is always smaller than that of neutron. It is also noted that the overlap between the ground state and the spherical state  $|\langle \Phi_{g.s.} | P^{J=0} \Phi(\beta = 0) \rangle|^2$  are large and not less than 0.8 in all O isotopes. This means that all ground states are approximated well by the spherical state, and hence, deformation plays only a minor role in O isotopes. As a result, compared to other isotope chains such as Be, B, Ne and Mg, the proton radii are kept almost constant except for the drip-line nucleus  $^{24}\text{O}$  despite of the increasing neutron radii and the

formation of the neutron skin toward the neutron drip line.

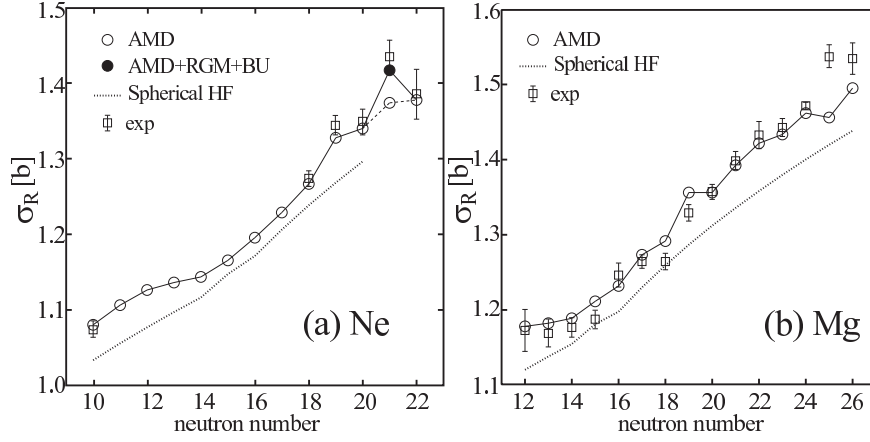


FIG. 11. Observed and calculated reaction cross sections of Ne and Mg isotopes. Open circles show the calculated cross sections by the density folding model which use the ground state density distribution obtained by AMD [125, 126], while the dotted lines use the density distributions obtained by spherical Hartree Fock. Filled circles (AMD+RGM+BU) shows the results obtained by using the density distribution of AMD+RGM [127] which is able to describe one neutron halo structure of  $^{31}\text{Ne}$  and the breakup effect is taken into account. Experimental data are taken from Refs. [120, 121].

In contrast to the O isotopes, deformation plays a major role for the structure evolution of Ne and Mg isotopes in which the breakdown of the  $N = 20$  magic number and the resultant large quadrupole deformation are well known [10, 128, 137, 138]. The stable nucleus  $^{20}\text{Ne}$  has the largest deformation among the Ne isotopes, which owes to the  $\alpha + ^{16}\text{O}$  clustering [3, 139, 140]. The addition of valence neutrons reduces deformation and changes the deformation pattern in  $^{22,24,26}\text{Ne}$ . Note that the  $d_{5/2}$  sub-shell closure leads to the oblate deformation of  $^{24}\text{Ne}$  which is common to other lighter  $N = 14$  isotones,  $^{19}\text{B}$  and  $^{20}\text{C}$ . The neutron number  $N = 18$  is also energetically favors the oblate deformation. As a result,  $^{28}\text{Ne}$  is another oblate deformed Ne isotope. Further addition of valence neutron changes the trend of deformation, because the Ne isotopes with  $N > 18$  are located in the island of inversion. Due to the breakdown of the neutron magic number  $N = 20$ , the ground state of  $^{30}\text{Ne}$  ( $N = 20$ ) is dominated by the intruder  $2\hbar\omega$  configuration and strongly deformed [117, 118, 129, 130]. The deformation of the ground state continues until the end of the isotope chain,  $^{34}\text{Ne}$ . This onset of the deformation in  $N > 18$  isotopes are experimentally

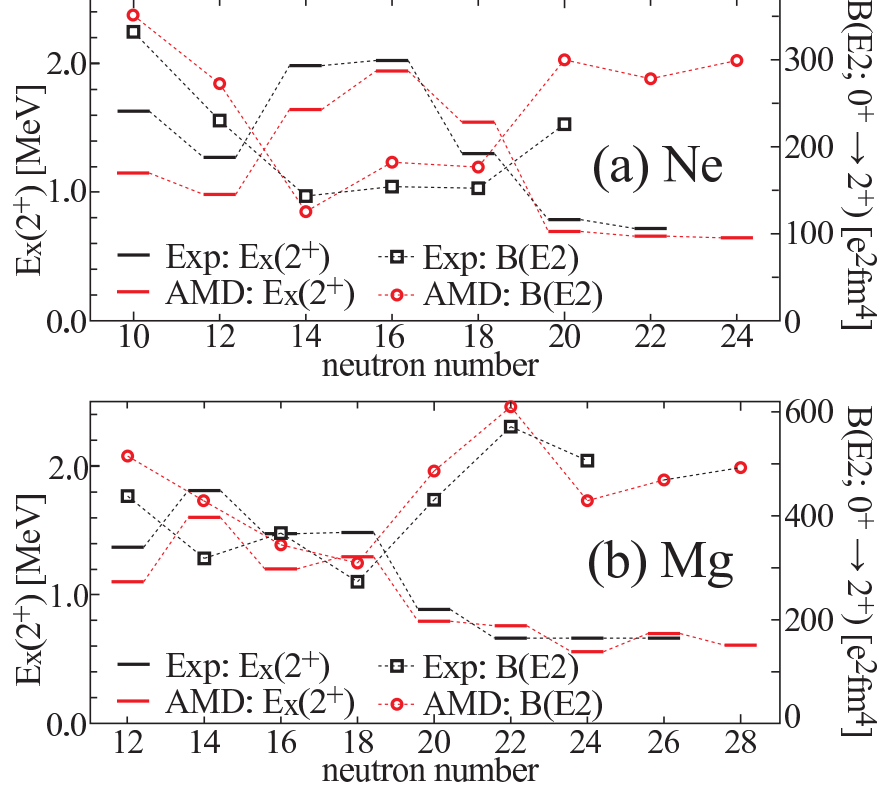


FIG. 12. Observed and calculated excitation energies of the  $2_1^+$  states and the reduced transition probabilities  $B(E2; 0_1^+ \rightarrow 2_1^+)$  in even-mass Ne and Mg isotopes. Experimental data are taken from Refs. [128–136].

confirmed from the sudden increase of  $B(E2)$  and the decrease of  $2_1^+$  energy (Fig. 12) [129–132].

Mg isotopes have similar deformation pattern to Ne isotopes: The stable nucleus  $^{24}\text{Mg}$  is strongly deformed [141–144], and the addition of valence neutrons reduces the deformation of  $N = 14, 16$  and  $18$  systems ( $^{26}\text{Mg}$ ,  $^{28}\text{Mg}$  and  $^{30}\text{Mg}$ ). The Mg isotopes with  $N > 18$  are also located in the island of inversion and their ground states are strongly deformed owing to the dominance of the intruder  $2\hbar\omega$  configurations [116, 117, 128, 129, 145]. It is interesting to note the differences of the deformation patterns between Ne and Mg isotopes. First, because the proton number  $Z = 12$  energetically favors the triaxial deformation [141–144], there are many isotopes ( $N = 12, 14, 18, 22$  and  $26$ ) exhibiting triaxial deformation. This suggests that Mg isotopes are rather soft against the  $\gamma$  deformation [146, 147]. Another point is the breakdown of the  $N = 28$  magic number. Mg isotopes have longer isotope

chain than Ne isotopes and the present calculation shows that all isotopes with  $N > 18$ , including the drip-line nucleus  $^{40}\text{Mg}$  ( $N = 28$ ), are deformed. It suggests that the island of inversion (neutron-rich  $N \simeq 20$  nuclei) and another region of nuclear deformation around  $^{42}\text{Si}$  [148–157] where the magic number  $N = 28$  is broken are merged. This is consistent with the recent observation [158, 159] which confirmed the systematic deformations of Mg isotopes toward neutron drip line.

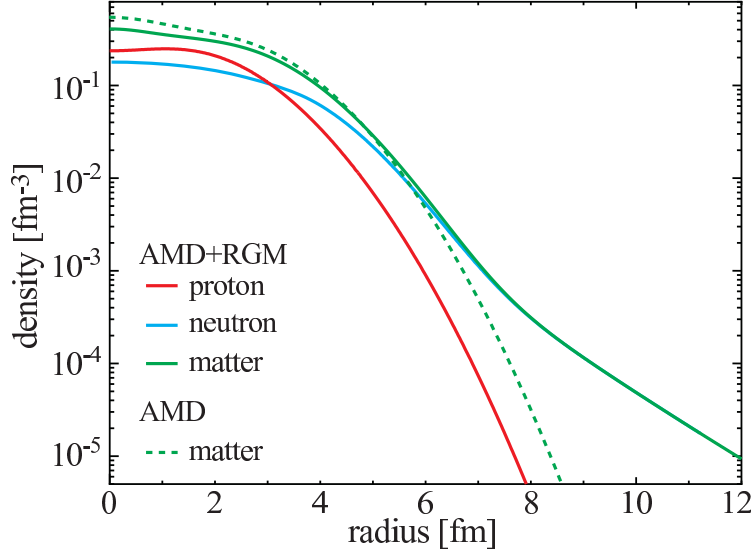


FIG. 13. Proton, neutron and matter (proton+neutron) density distributions of  $^{31}\text{Ne}$  calculated by AMD+RGM model [127]. Dashed line shows the matter density distribution obtained by ordinary AMD model. This figure is reconstructed from the data presented in Ref. [127].

The above-mentioned characteristics of Ne and Mg isotopes are reflected well to the reaction cross sections and matter radii. Figure 11 compares the observed reaction cross sections of Ne and Mg isotopes with the calculation by the density-folding model [120, 121, 125–127, 160]. To clarify the role of the nuclear deformation, the density-folding model employs two different density distributions of the ground states. The open circles show the results obtained by using the density distribution of the AMD (deformation is unrestricted), while the dotted lines show the results obtained by the density distribution of the spherical Hartree Fock (HF). It is clear that the AMD results reasonably agree with the observation indicating the importance of deformation. The differences between the AMD and spherical HF is large for  $N \simeq Z$  nuclei which are strongly deformed, but reduced for  $N = 14, 16$  and  $18$  isotones, and then, it is again enlarged for  $N > 18$  isotones. In both isotope chains, the large

deviation between AMD and spherical HF continues until the neutron drip line, which is common to the trend of the deformation pattern shown in Fig. 9, the  $2_1^+$  energies and  $B(E2)$  values shown in Fig. 12. It must be noted that the observed and calculated (AMD) cross sections are discontinuously increased from  $N = 18$  to 19 isotones, which clearly indicates that the west end of the island of inversion is at  $N = 19$  [119]. We also note that the AMD results considerably underestimate the cross sections of  $^{31}\text{Ne}$  and  $^{37}\text{Mg}$  [126, 160]. This implies the formation of neutron halo in these nuclei, because the ordinary AMD employs the Gaussian wave function and cannot describe the long-range part of the neutron halo wave function. To describe the halo structure, an extended version of AMD denoted by AMD+RGM was developed which combines the AMD with the resonating group method (RGM). By adopting AMD+RGM [160], the long-tail of the neutron density distribution of  $^{31}\text{Ne}$  is properly described as shown in Fig. 13 and the huge cross section of  $^{31}\text{Ne}$  is reasonably reproduced.

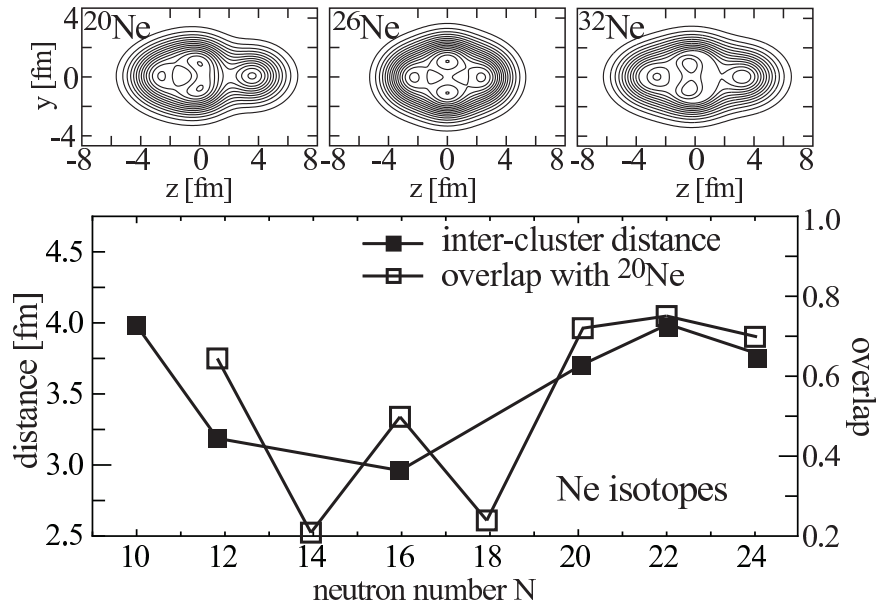


FIG. 14. Upper panels show the intrinsic proton density distributions of  $^{20}\text{Ne}$ ,  $^{26}\text{Ne}$  and  $^{32}\text{Ne}$ . Lower panel show the overlap between the proton wave functions of  $^{20}\text{Ne}$  and other Ne isotopes. It also shows an estimation of the distances between  $\alpha$  and  $^{16}\text{O}$  clusters. The inter-cluster distances in  $^{24}\text{Ne}$  and  $^{28}\text{Ne}$  were not evaluated because of too small overlap.

Now, we examine how the fingerprints of clustering can be seen in the radii. Similar to the Be and B isotopes, the behavior of proton radii of Ne isotopes can be attributed

to the clustering. The global behavior of proton radii in Ne and Mg isotope chains are similar to each other: They continue to increase in  $N > 18$  isotopes because of the large deformation. However, in addition to the deformation change, the reduction and growth of the clustering occurs in Ne isotopes. As confirmed from the density distribution shown in Fig. 14,  $^{20}\text{Ne}$  shows the  $\alpha + ^{16}\text{O}$  clustering. The additional neutrons reduce or vanish this clustering from  $^{22}\text{Ne}$  to  $^{28}\text{Ne}$ . But further addition of valence neutrons revives the clustering in Ne isotopes located in the island of inversion where the strong deformation of neutron distribution induces the clustering of proton distribution. As a result, the proton radius is reduced from  $^{22}\text{Ne}$  to  $^{28}\text{Ne}$  compared to  $^{20}\text{Ne}$ , and increases in neutron-rich Ne isotopes. Therefore, in Fig. 10, one sees that the proton radius of  $N = 10 \sim 24$  isotopes changes more largely in Ne isotopes than in Mg isotopes.

To evaluate this reduction and growth of  $\alpha + ^{16}\text{O}$  clustering more quantitatively, we calculated the overlap of the proton wave functions between  $^{20}\text{Ne}$  and other Ne isotopes [118]. Here, the overlap of the proton wave functions are defined and calculated as follows. First, we choose a single intrinsic wave function  $\Phi_{int}$  that has the largest squared overlap with the GCM wave function of the ground state  $\Psi_{gs}(^A\text{Ne})$ , and calculate the single-particle orbits  $\phi_i$ . Then, we pickup only the proton orbits and construct the antisymmetrized product of ten proton orbits,

$$\Psi_p(^A\text{Ne}) = \mathcal{A} \{ \phi_1 \phi_2, \dots, \phi_{10} \}. \quad (18)$$

The overlap of proton wave function  $\mathcal{O}$  is defined as the overlap between  $^{20}\text{Ne}$  and  $^A\text{Ne}$ ;

$$\mathcal{O} = | \langle \Psi_p(^{20}\text{Ne}) | \Psi_p(^A\text{Ne}) \rangle |^2. \quad (19)$$

We also estimated the inter-cluster distance  $d$  between  $\alpha$  and  $^{16}\text{O}$  clusters, which is calculated as follows. We first construct Brink-Bloch wave function [161] for  $^{20}\text{Ne}$  in which  $\alpha$  and  $^{16}\text{O}$  are placed with inter-cluster distance  $d$ ;

$$\Psi_{BB}(d) = \mathcal{A} \{ \phi_\alpha(-\frac{16}{20}\mathbf{d}) \phi_{^{16}\text{O}}(\frac{4}{20}\mathbf{d}) \}, \mathbf{d} = (0, 0, d), \quad (20)$$

where  $\phi_\alpha(-\frac{16}{20}\mathbf{d})$  and  $\phi_{^{16}\text{O}}(\frac{4}{20}\mathbf{d})$  are the wave functions of the  $\alpha$  and  $^{16}\text{O}$  clusters. They are assumed to have the double closed-shell configurations described by Harmonic oscillator wave functions and placed at  $-\frac{16}{20}\mathbf{d}$  and  $\frac{4}{20}\mathbf{d}$ , respectively. Using the same procedure explained above, we construct the antisymmetrized product of proton wave functions from  $\Psi_{BB}(d)$ ,



and calculate the overlap,

$$\mathcal{O}(d) = |\langle \Psi_{BB;p}(d) | \Psi_p({}^A\text{Ne}) \rangle|^2. \quad (21)$$

We regard that the value of  $d$  which maximizes the overlap  $\mathcal{O}(d)$  as the inter-cluster distance. Thus-obtained overlap and the inter-cluster distance are given in Fig. 14. They clearly show that the  $\alpha + {}^{16}\text{O}$  clustering is reduced in  $N = 12, 14, 16$  and 18 isotopes, but enhanced in the island of inversion. Note that this reduction and enhancement of the clustering is correlated well with the proton radii of Ne isotopes. Experimentally, charge radii of Ne and Mg isotopes are measured by the isotope shift up to  ${}^{28}\text{Ne}$  and  ${}^{32}\text{Mg}$  [122, 123]. Although the AMD calculation systematically overestimates the data, it nicely describes the neutron number dependence.

#### IV. CLUSTERS IN THE EXCITED STATES

Behind the variation of the ground state clustering discussed in the previous section, the shell effect of excess neutrons is playing an essential role. It was suggested that a special class of the shell structure called molecular orbits is formed around the clustered core in Be isotopes. The AMD calculations proved the existence of the molecular orbits without *a priori* assumptions.

Theoretical calculations including AMD showed that the molecular orbits naturally explain the variation of the ground state clustering. In addition to this, they also showed that not only the ground states but also the excited states are explained and predicted by the molecular orbits. Thus, the study of neutron-rich Be isotopes revealed a novel type of clustering; the clustered core with covalent neutrons. In this decade the study is extended to highly excited states where the atomic orbits are formed and ionic bonding dominates over the covalent bonding. The studies of Be and B isotopes by AMD are summarized in the section IV A.

This success of the molecular orbits strongly motivated the extension of the concept to other nuclei. The highlights of the extension is summarized as follows; (1) Universality of the concept: It is of interest and importance to investigate if the concept of the molecular orbit applies to other nuclei universally and if it yields a novel type clustering in a broader region of the nuclear chart. (2) Molecular orbits in the asymmetric systems: The molecular

orbits formed around the parity asymmetric cluster core should have different nature from those of Be isotopes. (3) Extension to the multi-cluster systems: Since the valence neutrons in the molecular orbits play a glue-like role, we expect that the multi-cluster systems such as  $n\alpha$  cluster systems may be stabilized by the addition of the valence neutrons. In the section IV B, we examine the points (1) and (2) by using O, F and Ne isotopes as examples. The point (3) is discussed in the section IV C focusing on the  $3\alpha$  cluster states in C isotopes.

## A. Molecular orbits and di-cluster resonances in Be isotopes

### 1. Overview of cluster structures in Be isotopes

As already discussed in the previous section, the ground states of Be isotopes have cluster structures, which play an important role in the shell breaking mechanism of neutron-rich Be. In these decades, cluster structures in the ground and excited states of Be isotopes have been intensively investigated by many theoretical works [13–15, 17, 31, 33, 44–66]. Low-lying states of neutron-rich Be isotopes are described well by molecular orbit models assuming valence neutrons in molecular orbits surrounding the  $2\alpha$  core. In the highly excited states near and above the  $\alpha$ -decay threshold energy, dinuclear-type He+He cluster resonances (di-cluster resonances) have been predicted by two-body cluster models [52, 53, 63] and more generalized cluster models [57, 59–61, 64, 66]. Appearance of such cluster structure in neutron-rich Be isotopes has been theoretically verified by the AMD, FMD and no-core shell model approaches [45, 58, 62, 162], which do not rely on *a priori* assumption of existence of any clusters.

In order to understand cluster features of low-lying states of neutron-rich Be isotopes, the molecular orbit (MO) is a useful picture, which has been applied for  $^9\text{Be}$  [163–165] and extended to neutron-rich Be isotopes [13–15, 17, 49, 50]. As already mentioned, the  $2\alpha$  core is formed in neutron-rich Be isotopes as a result of many-body correlation in  $A$ -nucleon dynamics. In the  $2\alpha$  systems with valence neutrons, molecular orbits around the  $2\alpha$  core are constructed by linear combination of  $p$ -orbits around  $\alpha$  clusters and are occupied by valence neutrons. Schematic figures of molecular orbits are shown in Fig. 15. Negative-parity orbits called " $\pi_{3/2}$ -orbit" and " $\pi_{1/2}$ -orbit" are the lowest nodal orbits with one node in the transverse direction corresponding to  $p$ -orbits in the spherical shell model limit. The

$\pi_{3/2}$ -orbit is an  $ls$ -favored orbit and the lowest orbit in the  $2\alpha$  system. The positive-parity orbits denoted by " $\sigma_{1/2}$ -orbit" and " $\pi_{3/2}^*$ -orbit" are higher nodal orbits. Since the  $\sigma_{1/2}$ -orbit is a longitudinal orbit having two nodes along the  $\alpha$ - $\alpha$  direction, its kinetic energy reduces as the  $2\alpha$  cluster develops. Consequently, valence neutrons in the  $\sigma_{1/2}$ -orbit push two  $\alpha$ s outward keeping them at a moderate distance, and enhance the cluster structure of neutron-rich Be isotopes. Moreover, in a developed cluster structure, the lowered  $\sigma_{1/2}$ -orbit eventually comes down below the  $ls$ -unfavored  $\pi_{1/2}$ -orbit, and induces the breaking of the  $N = 8$  shell closure.

In a cluster state with a  $\sigma_{1/2}$ -orbit configuration,  $2\alpha$  clusters are tightly bonded at a moderate distance by the valence neutrons in the  $\sigma_{1/2}$ -orbit. We call this structure with  $\sigma_{1/2}$ -orbit neutrons "the MO  $\sigma$ -bond structure". However, in the asymptotic region of large inter-cluster distance, the system approaches di-cluster states of He+He, in which valence neutrons occupy atomic orbits around either of  $\alpha$  clusters instead of molecular orbits to gain correlation energy between valence neutrons. Owing to inter-cluster excitations in the di-cluster structure, He+He cluster resonances (called di-cluster resonances) appear in highly excited region. For instance,  ${}^6\text{He}+{}^4\text{He}$  and  ${}^{6(8)}\text{He}+{}^{6(4)}\text{He}$  cluster resonances have been predicted in  ${}^{10}\text{Be}$  and  ${}^{12}\text{Be}$ , respectively. It means that two kinds of remarkable cluster structures coexist in neutron-rich Be isotopes. One is the MO  $\sigma$ -bond states in the strong coupling regime, and the other is the di-cluster resonances in the weak coupling regime. The latter usually appears in relatively higher energy region than the MO  $\sigma$ -bond states. In order to unify these two kinds of cluster states, the MO  $\sigma$ -bond and the di-cluster resonance states, Ito and his collaborators developed a method of the generalized two-center cluster model (GTCM), which successfully describes the cluster structures of  ${}^{10}\text{Be}$  and  ${}^{12}\text{Be}$ , and showed transition of valence neutron configurations from molecular orbits to atomic orbits. Motivated by the theoretical predictions, many experimental studies have been achieved to search for rotational band members of the MO  $\sigma$ -bond states and di-cluster resonances.

## 2. Band structures of ${}^{10}\text{Be}$ , ${}^{11}\text{Be}$ , and ${}^{12}\text{Be}$

Let us discuss the band structures of  ${}^{10}\text{Be}$ ,  ${}^{11}\text{Be}$ , and  ${}^{12}\text{Be}$  based on the AMD+VAP results using the MV1 central and G3RS spin-orbit interactions [48, 55, 56, 166]. Calculated energy levels are shown in Fig. 16 compared with experimental ones. Energy levels of  ${}^{10}\text{Be}$  are

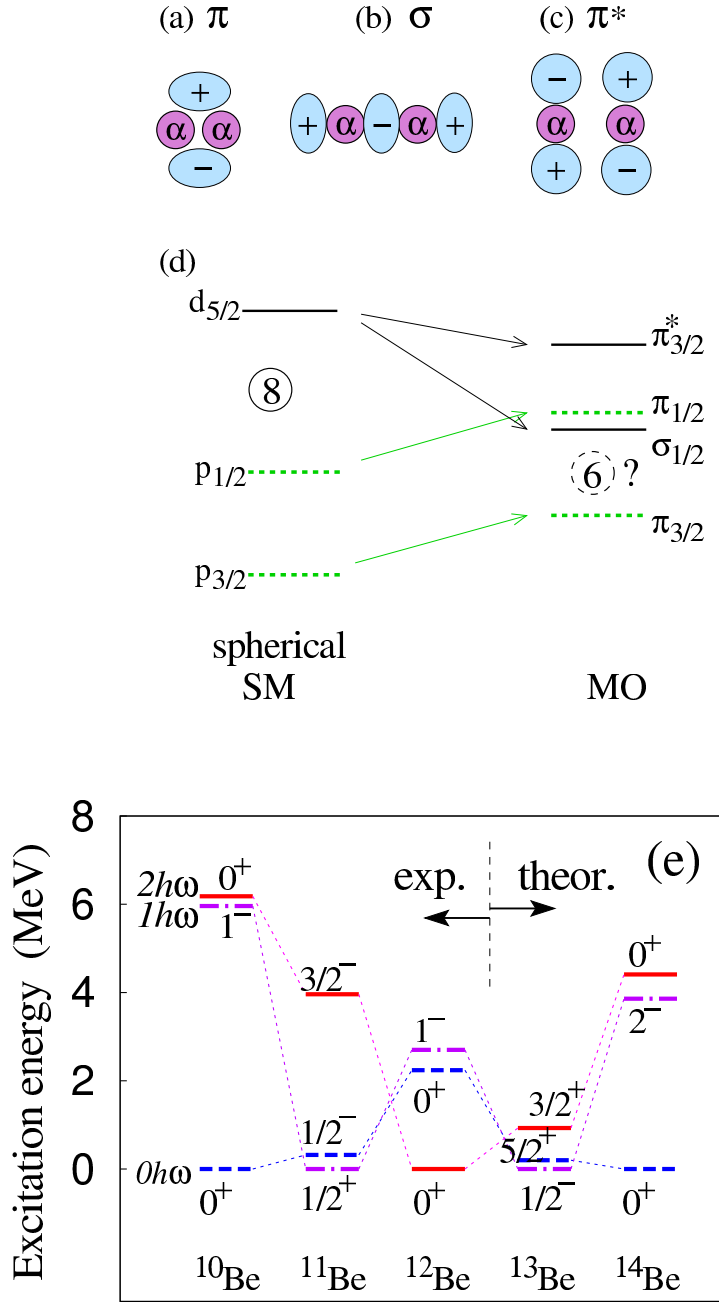
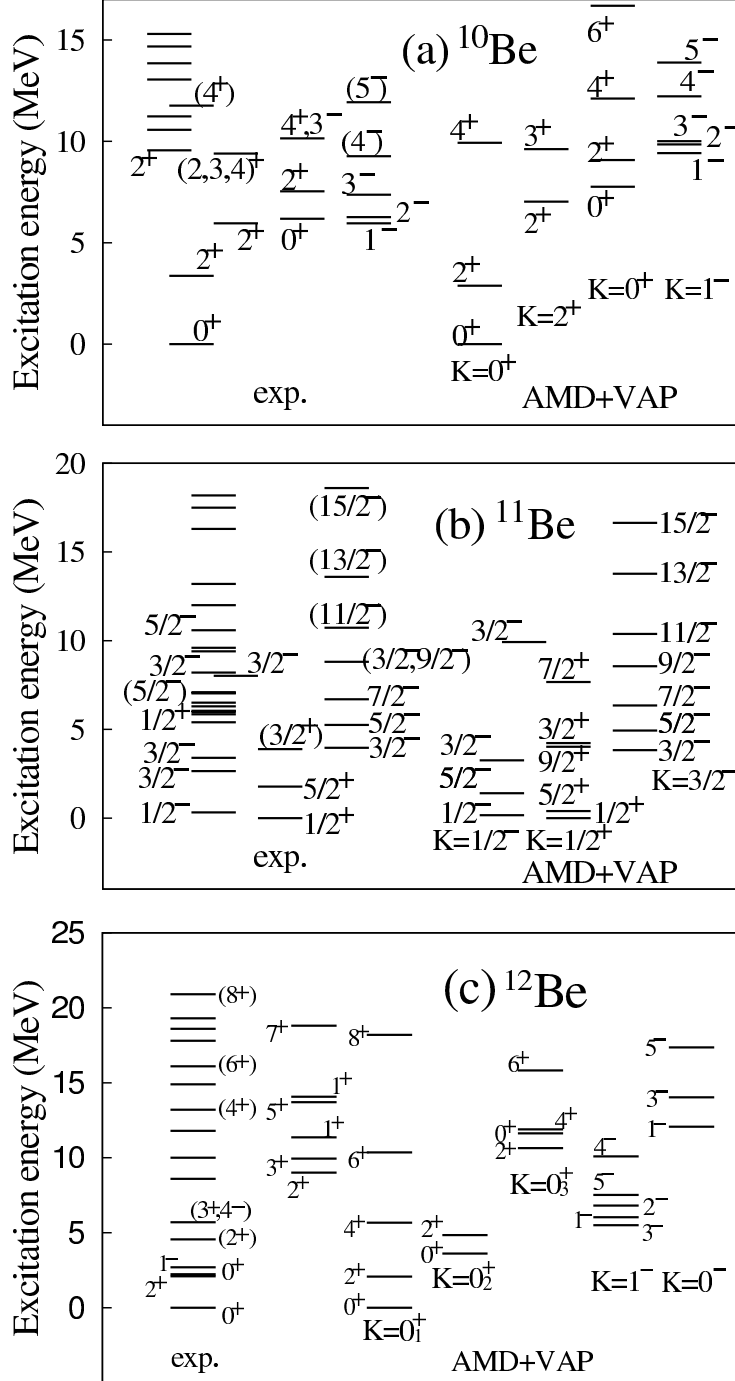


FIG. 15. (a)(b)(c) Schematic figures of molecular orbits around the  $2\alpha$  core in Be isotopes. (d) A schematic figure of evolution of single-particle energies from spherical shell-model orbits to molecular orbits. (e) Experimental energy levels assigned to band-head states in low-lying spectra of  $^{10}\text{Be}$ ,  $^{11}\text{Be}$ , and  $^{12}\text{Be}$ , and theoretical ones of  $^{13}\text{Be}$  and  $^{14}\text{Be}$  obtained by the AMD+VAP calculations using the MV1 ( $m = 0.65$ ,  $b = h = 0$ ) central and G3RS ( $u_1 = -u_2 = -3700$  MeV) spin-orbit interactions [54, 65]. Figures are modified from the original ones in Ref. [65].



classified into four rotational bands,  $K^\pi = 0_1^+, 2^+, 0_2^+$ , and  $1^-$ , consisting of band members  $J^\pi = (0_1^+, 2_1^+, 4_1^+)$ ,  $(2_2^+, 3_1^+)$ ,  $(0_2^+, 2_3^+, 4_2^+, 6_1^+)$ , and  $(1^-, 2^-, 3^-, 4^-, 5^-)$ , respectively. The band-head states of these bands are assigned to the experimentally observed states,  $0_1^+$ ,  $2_2^+$  (5.96 MeV),  $0_2^+$  (6.18 MeV), and  $1_1^-$  (5.96 MeV). Various kinds of cluster structures are found in the intrinsic states of these bands. The ground state of  $^{10}\text{Be}$  has the normal neutron configuration  $(\pi_{3/2}^2)$  with the  $2\alpha$  core. The  $K^\pi = 2^+$  band is regarded as a side band of the ground band arising from two neutron correlation, in other words, a triaxial intrinsic structure as discussed in Refs. [51, 62]. The  $K^\pi = 0_2^+$  band has a MO  $\sigma$ -bond structure with a remarkably developed cluster structure, in which  $2\alpha$  clusters are bonded by two valence neutrons in the  $\sigma_{1/2}$ -orbit (the  $\sigma_{1/2}^2$  configuration). The  $K^\pi = 1^-$  band is a negative-parity band with a  $\pi_{3/2}$ -orbit neutron and a  $\sigma_{1/2}$ -orbit neutron (the  $\pi_{3/2}\sigma_{1/2}$  configuration). Because of the  $\sigma_{1/2}$ -orbit neutron, the intrinsic state has a moderately developed cluster structure and constructs the rotational band.

Many experiments have been performed to discover new states and confirm band structures, in particular, coexistence of the ground  $K^\pi = 0_1^+$  band and the MO  $\sigma$ -bond  $K^\pi = 0_2^+$  band [67–75, 77]. In Fig. 17, the observed positive-parity energy levels of  $^{10}\text{Be}$  are plotted as functions of  $J(J+1)$  compared with theoretical energy spectra of the AMD+VAP [48],  $\beta$ - $\gamma$  AMD [62],  $^6\text{He}+\alpha$  cluster model [169], AMD+DC [170], and 4-body  $2\alpha + 2n$  calculations [59].

In the AMD+VAP result, the MO  $\sigma$ -bond structure having the enhanced cluster structure constructs the  $K^\pi = 0_2^+$  band up to  $J = 6$  with a large moment of inertia. Experimental studies have revealed a  $2^+$  state at 7.54 MeV and a  $4^+$  state at 10.2 MeV, which likely possess a  $^6\text{He}+\alpha$  cluster structure [73, 74]. These  $2^+$  and  $4^+$  states are candidates of the  $K^\pi = 0_2^+$  band members starting from the  $0_2^+$  (6.18 MeV). This assignment is consistent with the energy slope of the calculated  $K^\pi = 0_2^+$  band. Other theoretical calculations, the  $\beta$ - $\gamma$  AMD [62],  $^6\text{He}+\alpha$  cluster model [169], AMD+DC [170], and 4-body  $2\alpha + 2n$  calculations [59], as well as the  $^6\text{He}+\alpha$  GCM [53] give almost consistent results for these bands with the AMD+VAP result.

Another interesting problem in  $^{10}\text{Be}$  is whether di-cluster resonances of  $^6\text{He}+^4\text{He}$  exist. Theoretical calculations predicted  $0^+$  states a few MeV higher than the  $0_2^+$  state as shown in Fig. 17. The AMD+DC and  $^6\text{He}+\alpha$  cluster models predicted  $^6\text{He}(0^+)+^4\text{He}$  cluster resonances, whereas the GTCM predicted the  $^6\text{He}(0^+)+^4\text{He}$  state as a broad continuum state

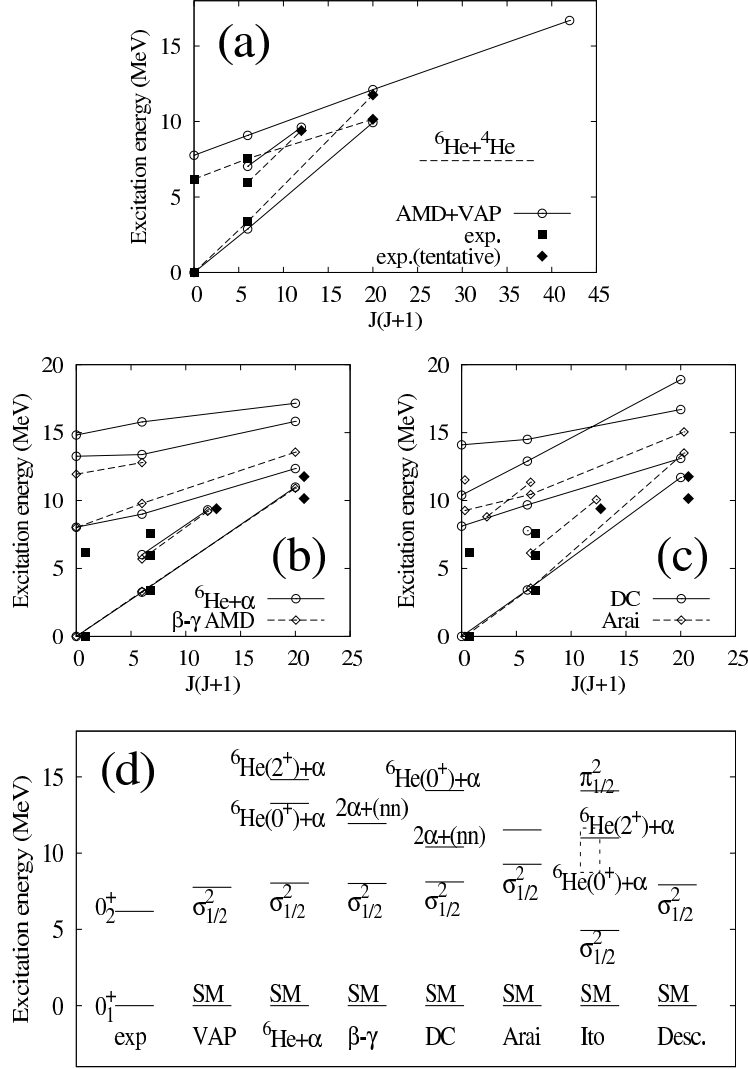


FIG. 17. (a)(b)(c): Energy spectra of positive parity states in  $^{10}\text{Be}$ . (d): excitation energies of  $0^+$  states in  $^{10}\text{Be}$ . Theoretical energies are those obtained by the AMD+VAP using the MV1 ( $m = 0.62$ ,  $b = h = 0$ ) central and G3RS ( $u_1 = -u_2 = -3000$  MeV) spin-orbit interactions [48], the  $^6\text{He}+\alpha$  cluster model in Ref. [169], the  $\beta\text{-}\gamma$  constraint AMD [62], the dineutron condensation(DC)+AMD model [170], the stochastic variational method of  $2\alpha + 2n$  by Arai *et al.* [59], the generator coordinate method of  $^6\text{He}+\alpha$  by Descouvemont *et al.* [53], and the generalized two-center cluster model by Ito *et al.* [66]. The effective nuclear interactions used in Refs. [62, 169, 170] are the Volkov No.2 ( $m = 0.6$ ,  $b = h = 0.125$ ) central and G3RS ( $u_1 = -u_2 = -1600$  MeV) spin-orbit interactions. For other theoretical calculations, spectra calculated by the Minnesota central interaction [171] supplemented by spin-orbit interaction of Refs. [53, 59] and those using the Volkov No.2 ( $m = 0.643$ ,  $b = h = 0.125$ ) central and G3RS ( $u_1 = -2000$  MeV,  $u_2 = 3000$  MeV) spin-orbit interactions of Ref. [66] are shown. The experimental data are those from Ref. [105] and references therein.

(the dashed line in Fig. 17(d)). Moreover,  ${}^6\text{He}(2^+)+{}^4\text{He}$  cluster resonances and a three-cluster resonance of  $2\alpha + nn$  have been theoretically predicted. A very broad  $0^+$  state of the  ${}^6\text{Li}(T=1)+\alpha$  resonance, which was recently observed at 11 MeV in  ${}^{10}\text{B}$  [172], is a candidate of the isobaric analog state of a  ${}^6\text{He}+\alpha$  cluster resonance.

For  ${}^{11}\text{Be}$  (Fig. 16(b)), we obtain three rotational bands, the  $K^\pi = 1/2^+$ ,  $K^\pi = 1/2^-$ , and  $K^\pi = 3/2^-$  bands. In the AMD+VAP calculation, the effective nuclear interaction is adjusted to reproduce the parity inversion of the  $1/2_1^-$  and  $1/2_1^+$  states in  ${}^{11}\text{Be}$  [55]. The  $K^\pi = 1/2^-$  is the normal state with the  $\pi_{3/2}^2\pi_{1/2}$  configuration corresponding to the  $0\hbar\omega$   $p$ -shell configuration. The  $K^\pi = 1/2^+$  is a MO  $\sigma$ -bond state with two neutrons in the  $\pi_{3/2}$ -orbit and the last neutron in the  $\sigma_{1/2}$ -orbit (the  $\pi_{3/2}^2\sigma_{1/2}$  configuration). This corresponds to the intruder  $1\hbar\omega$  state with one particle in the higher shell ( $sd$ -shell) in terms of the spherical shell model. The ground state is the band-head  $1/2^+$  state of the  $K^\pi = 1/2^+$  band constructed by the MO  $\sigma$ -bond structure. The abnormal spin-parity  $1/2^+$  of the ground state in  ${}^{11}\text{Be}$  has been known as the breaking of the  $N = 8$  magic number. Because of one neutron in the  $\sigma_{1/2}$ -orbit, the  $K^\pi = 1/2^+$  band has the moderately developed cluster structure. In the calculation, another type of MO  $\sigma$ -bond structure with two  $\sigma_{1/2}$ -orbit neutrons (the  $\pi_{3/2}\sigma_{1/2}^2$  configuration) is obtained as an excited band. Because of two neutrons in the  $\sigma_{1/2}$ -orbit, the cluster structure is developed further and it constructs the  $K^\pi = 3/2^-$  band up to high spin states with small level spacing, *i.e.*, a large moment of inertia. The existence of the MO  $\sigma$ -bond band with the  $\sigma_{1/2}^2$  configuration has been suggested by von Oertzen *et al.* (Ref. [16] and references therein). Candidates for  $K^\pi = 3/2^-$  band members have been experimentally observed by two-neutron transfer reactions [16, 78, 79]. The theoretical energy spectra of the  $K^\pi = 3/2^-$  band obtained by the AMD+VAP is consistent with the experimental assignment of the  $K^\pi = 3/2^-$  band starting from  $3/2^-$  state at 3.96 MeV.

The ground and excited states of  ${}^{12}\text{Be}$  have been calculated using the same effective nuclear interaction as that used for  ${}^{11}\text{Be}$ . The calculated energy levels of  ${}^{12}\text{Be}$  are classified into three positive-parity bands ( $K^\pi = 0_1^+, 0_2^+$ , and  $0_3^+$ ) and two negative-parity bands ( $K^\pi = 1^-$  and  $0^-$ ) (Fig. 16(c)). The low-lying  $K^\pi = 0_1^+$ ,  $0_2^+$ , and  $1^-$  bands are understood as molecular  $\pi$ - and  $\sigma$ -orbit configurations, whereas the  $K^\pi = 0_3^+$  and  $0^-$  bands in the high-energy region are He+He di-cluster resonances.

The ground band ( $K^\pi = 0_1^+$ ) has a MO  $\sigma$ -bond structure with two  $\sigma_{1/2}$ -orbit neutrons (the  $\pi_{3/2}^2\sigma_{1/2}^2$  configuration), which corresponds to the intruder  $2\hbar\omega$  configuration (2 particles



in the  $sd$  shell) indicating the breaking of the  $N = 8$  shell. The  $K^\pi = 0_2^+$  band is dominated by the  $\pi_{3/2}^2\pi_{1/2}^2$  configuration corresponding to a normal  $0\hbar\omega$  configuration with the neutron  $p$ -shell closure. The band-head state of the  $K^\pi = 0_2^+$  band is assigned to the experimental  $0_2^+$  state at 2.1 MeV. As a result of the inversion between the normal and intruder configurations, the ground state of  $^{12}\text{Be}$  has a large deformation with the cluster structure enhanced by two  $\sigma_{1/2}$ -orbit neutrons even though  $^{12}\text{Be}$  is an  $N = 8$  nucleus. The intruder configuration and large deformation of the ground state have been experimentally supported by weak  $\beta$  decays to  $^{12}\text{B}$  [85, 86], strong  $E2$  transitions in the ground band [89, 90, 94], and other experiments [87, 88, 92, 95], and more directly evidenced by  $1n$ -knockout reactions [91, 93]. The  $K^\pi = 1^-$  band is constructed by a MO  $\sigma$ -bond structure with the  $\pi_{3/2}^2\pi_{1/2}\sigma_{1/2}$  configuration. This band has a moderately enhanced cluster structure with a  $\sigma_{1/2}$ -orbit neutron.

In the progress of experimental and theoretical investigations of  $^{12}\text{Be}$  in the recent past years, He+He di-cluster resonances in highly excited states are being revealed [17, 52, 56, 61, 63, 64, 66, 79–84]. Many excited states have been observed above the He+He threshold energies by  $^6\text{He}+^6\text{He}$  and  $^8\text{He}+^4\text{He}$  break-up reactions [81–84]. They are considered to be He+He di-cluster resonances. For the theoretical side, He+He resonances have been predicted near and above the threshold energies by the GCM [52, 63], AMD+VAP [56, 166], and GTCM calculations [61, 64, 66]. The theoretical rotational band structures of  $^{12}\text{Be}$  are shown in Fig. 18. The results of low-lying levels for the  $K^\pi = 0_1^+$  and  $K^\pi = 0_2^+$  bands obtained by the AMD+VAP and GTCM are qualitatively consistent with each other, and they reproduce well the experimental low-energy spectra. In the energy region above the He+He thresholds, the GTCM predicts the  $^6\text{He}+^6\text{He}$  di-cluster resonance band and also the  $^8\text{He}+^4\text{He}$  di-cluster resonance band. The di-cluster resonances have been also predicted by the GCM calculations, however, the  $^6\text{He}+^6\text{He}$  and  $^8\text{He}+^4\text{He}$  components are mixed in the  $K^\pi = 0_3^+$  rotational band, that is, the  $0^+$  state has the dominant  $^6\text{He}+^6\text{He}$  component while the  $2^+$  and  $4^+$  states contain mixed components of two channels. The AMD+VAP calculation shows a di-cluster resonance feature in the  $K^\pi = 0_3^+$  band, in which the structure changes as the increase of  $J$  from the  $^6\text{He}+^6\text{He}$  structure to the strong coupling cluster structure, probably containing mixed components of  $^6\text{He}+^6\text{He}$  and  $^8\text{He}+^4\text{He}$ . The side-band,  $K^\pi = 2^+$  band associated with the  $K^\pi = 0_3^+$  band, is also predicted.

In addition to the positive-parity bands, the GCM calculations [52, 63] and the AMD+VAP calculation [166] predict a negative-parity band  $K^\pi = 0^-$  of  $^8\text{He}+^4\text{He}$  di-cluster resonances

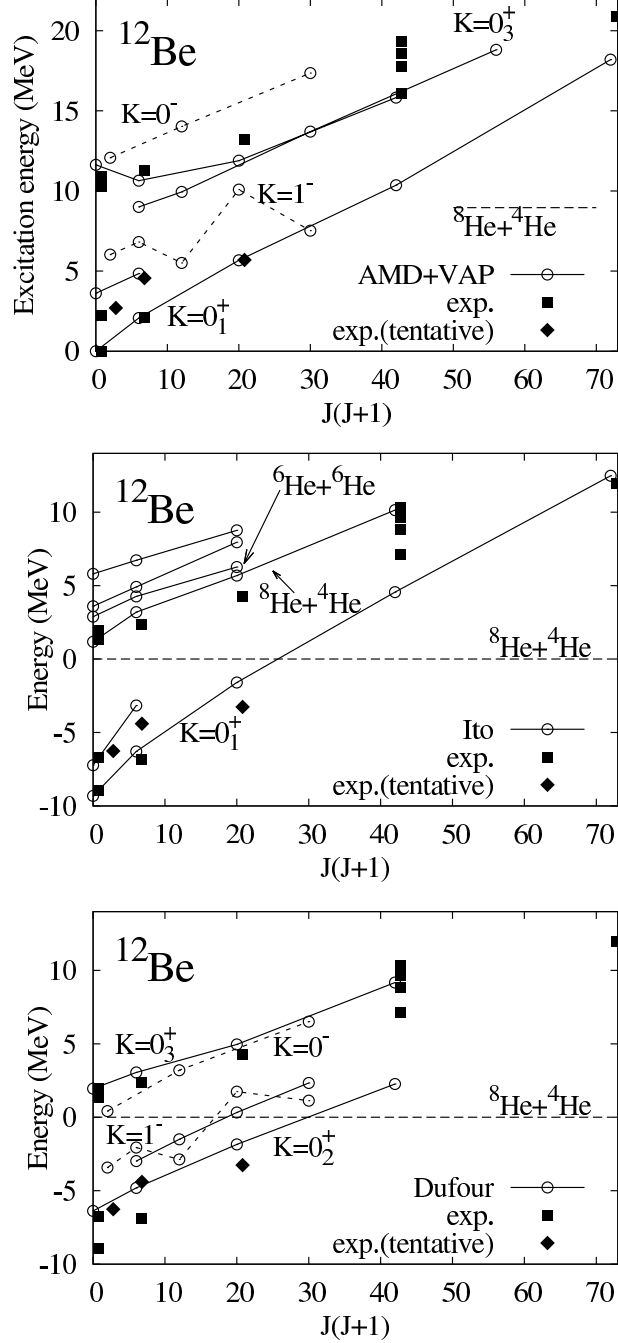


FIG. 18. Energy spectra of positive- and negative-parity rotational bands in  $^{12}\text{Be}$ . Excitation energies obtained by the AMD+VAP using the MV1 ( $m = 0.65$ ,  $b = h = 0$ ) central and G3RS ( $u_1 = -u_2 = -3700$  MeV) spin-orbit interactions [56, 166] are shown in the top panel. Energies from the  $\alpha$ -decay threshold calculated with the generalized two-center cluster model by Ito *et al.* [61], and those with the GCM of  $^6\text{He} + ^6\text{He}$  and  $^8\text{He} + \alpha$  by Dufour *et al.* [63] are shown in the middle and bottom panels, respectively. The Volkov No.2 central interactions and the spin-orbit interactions are used in those calculations of Refs. [61, 63]. Experimental data of spin-assigned energy levels from Refs. [81–84, 88, 106, 168] are shown by filled symbols. Energy levels with tentative spin assignment are shown by filled diamonds.

consisting of  $1^-$ ,  $3^-$ , and  $5^-$  states. Considering that a reflection asymmetric intrinsic structure of the ground  $K^\pi = 0_1^+$  band having  $^8\text{He}+^4\text{He}$  clustering, the  $K^\pi = 0^-$  band can be interpreted as the parity partner of the  $K^\pi = 0_1^+$  band caused by the negative-parity excitation of  $^8\text{He}-^4\text{He}$  motion, and is associated with the well-known parity doublet  $K^\pi = 0^-$  band in  $^{20}\text{Ne}$ . It means that negative-parity excitations in the two bands,  $K^\pi = 1^-$  and  $K^\pi = 0^-$ , of  $^{12}\text{Be}$  are different. The former is a single-particle excitation between  $\pi_{1/2}$ - and  $\sigma_{1/2}$ -orbits, and the latter is an excitation of the inter-cluster motion. It should be pointed out that the energy cost for the single-particle excitation in the MO configuration is small because of vanishing of the  $N = 8$  shell gap in the developed cluster system. This is a reason why the  $K^\pi = 1^-$  band appears in the low-energy region. Intense experimental efforts are being made to establish band structures of  $^{12}\text{Be}$  including the low-lying MO  $\sigma$ -bond states and the high-lying di-cluster resonances.

### 3. Systematics of low-lying states of Be isotopes from molecular orbit picture

As discussed previously, the molecular orbits play an important role in cluster structures of low-lying states of neutron-rich Be isotopes. In particular,  $\sigma_{1/2}$ -orbit neutrons enhance the cluster structure to form the MO  $\sigma$ -bond structure. Moreover, the lowering mechanism of the  $\sigma_{1/2}$ -orbit in developed cluster structures is essential for the vanishing of the  $N = 8$  magic number in  $^{11}\text{Be}$  and  $^{12}\text{Be}$ . Looking into systematics of low-lying states in the series of Be isotopes, we here discuss evolution of the clustering in relation to the vanishing of the  $N = 8$  magic number from the molecular orbit picture.

Let us briefly review again the molecular orbits proposed by Seya *et al.* and von Oertzen *et al.* In the molecular orbit model for  $2\alpha$  cluster systems, molecular orbits given by the linear combinations of  $p$ -orbits around  $\alpha$  clusters are considered for valence neutron configurations. As shown in Refs. [14, 15, 17, 173], single-particle energy levels are smoothly connected from the one-center to the two-center limits as functions of  $\alpha$ - $\alpha$  distance. The orbits in a moderate distance region correspond to molecular orbits. We call negative-parity orbits constructed by  $p$ -orbits perpendicular to the  $\alpha$ - $\alpha$  direction “ $\pi$ -orbits”, and a positive-parity orbit from  $p$ -orbits parallel to the  $\alpha$ - $\alpha$  direction “ $\sigma$ -orbit” in analogy to covalent orbits of electrons in molecules (see Figs. 15 (a) and (b)). We call the other positive-parity orbit given by  $p$ -orbits perpendicular to the  $\alpha$ - $\alpha$  direction “ $\pi^*$ -orbit” (Fig. 15(c)). In addition

to the spatial configurations ( $\pi$ ,  $\sigma$ , and  $\pi^*$ ), molecular orbits are specified by the angular momentum  $\Omega \equiv j_z$  projected on to the symmetry axis  $z$ . With the label  $\Omega$ , we use the notations,  $\pi_{3/2,1/2}$ ,  $\sigma_{1/2}$ , and  $\pi_{3/2,1/2}^*$ . Here, the  $\pi_{3/2(1/2)-}$  and  $\pi_{3/2(1/2)}^*$ -orbits are  $ls$ -favored (unfavored) orbits. Note that the present notations,  $\pi_{3/2}$ ,  $\pi_{1/2}$ ,  $\sigma_{1/2}$ , and  $\pi_{3/2}^*$  correspond to the labels  $\pi_{3/2}^-(g)$ ,  $\sigma_{1/2}^-(g)$ ,  $\sigma_{1/2}^+(u)$ , and  $\pi_{3/2}^+(u)$  in Ref. [17], and the labels  $(3u, 1)$ ,  $(1u, 2)$ ,  $(1g, 2)$ , and  $(1g, 2)$  in Ref. [13], respectively. In the spherical shell model limit, the  $\pi_{3/2-}$  and  $\pi_{1/2-}$ -orbits become the  $p_{3/2-}$  and  $p_{1/2-}$ -orbits, respectively, whereas the  $\sigma_{1/2-}$  and  $\pi_{3/2}^*$ -orbits become the  $d_{5/2}$ -orbits (see Fig. 15(d)). As the  $\alpha$ - $\alpha$  distance increases, the energy of the  $\sigma_{1/2}(\pi_{3/2,1/2}^*)$ -orbit with two nodes (one node) along the longitudinal ( $z$ ) axis decreases because of the kinetic energy reduction, whereas the energies of the  $\pi_{3/2,1/2}$ -orbits with no node rise up. Consequently, the inversion of the  $\pi_{1/2-}$  and  $\sigma_{1/2-}$ -orbits occurs in the developed cluster system. It is also important that  $\sigma_{1/2-}$  and  $\pi_{3/2}^*$ -orbit neutrons enhance the cluster structure because of the lowering mechanism, however,  $\pi_{3/2,1/2}$ -orbit neutrons tend to suppress the cluster structure to gain the potential energy.

We summarize the molecular orbit configurations of the band-head states of Be isotopes in Table I. The matter density distributions of the intrinsic states are shown in Fig. 19, and the single-particle densities are shown in Fig. 20. Strictly speaking, realistic Be states do not have pure molecular orbit configurations but they are given by mixed configurations. As shown in Figs. 19 and 20, most of the intrinsic states of Be obtained by the AMD+VAP show reflection asymmetry indicating that single-particle wave functions somewhat deviate from the ideal molecular orbits, which should be reflection symmetric. The asymmetry is caused by many-body correlations between valence neutrons. In the strong correlation limit in the asymptotic region, valence neutrons are distributed around either of 2  $\alpha$ s and molecular orbit configurations change into atomic orbit configurations as discussed by Ito *et al.* [57, 61, 66]. In a transient region, the molecular orbit structures somewhat couple with two-body He+He di-cluster components. The assignment of molecular orbit configurations in Table I is based on dominant features such as nodal structures and percentages of positive- and negative-parity components of single-particle wave functions obtained by the AMD+VAP calculations [48, 54–56, 65]. As already described,  $^{10}\text{Be}(0_1^+)$ ,  $^{10}\text{Be}(1^-)$ , and  $^{10}\text{Be}(0_2^+)$  are understood as the  $\pi_{3/2}^2$ ,  $\pi_{3/2}\sigma_{1/2}$ , and  $\sigma_{1/2}^2$ , respectively. In a similar way,  $^{11}\text{Be}(1/2^+)$ ,  $^{11}\text{Be}(1/2^-)$ , and  $^{11}\text{Be}(3/2_2^-)$  states are described by the  $\pi_{3/2}^2\sigma_{1/2}$ ,  $\pi_{3/2}^2\pi_{1/2}$  and  $\pi_{3/2}\sigma_{1/2}^2$  configurations, and  $^{12}\text{Be}(0_1^+)$ ,  $^{12}\text{Be}(0_2^+)$ , and  $^{12}\text{Be}(1_1^-)$  states correspond to  $\pi_{3/2}^2\sigma_{1/2}^2$ ,

TABLE I. Molecular orbit configurations of band-head states of low-lying states in Be isotopes. Neutron configurations around the  $2\alpha$  core are listed. The  $0\hbar\omega$ ,  $1\hbar\omega$ , and  $2\hbar\omega$  excitations of the shell model (SM) configurations are also shown based on the correspondence of negative-parity orbits ( $\pi_{3/2}, \pi_{1/2}$ ) and positive-parity orbits ( $\sigma_{1/2}, \pi_{3/2}^*$ ) to the  $p$ - and  $sd$ -orbits in the spherical limit, respectively. The numbers ( $n_\pi, n_\sigma, n_{\pi^*}$ ) of  $\pi$ -,  $\sigma$ -,  $\pi^*$ -orbit neutrons are also listed. The assignment of the SM and MO configurations are based on Ref. [65]. (The configuration for  $^{13}\text{Be}(5/2^+)$  is tentative.)

	SM	MO config.	$n_\pi, n_\sigma + n_{\pi^*}$
$^{10}\text{Be}(0_1^+)$	$0\hbar\omega$	$\pi_{3/2}^2$	2,0
$^{10}\text{Be}(1^-)$	$1\hbar\omega$	$\pi_{3/2}\sigma_{1/2}$	1,1
$^{10}\text{Be}(0_2^+)$	$2\hbar\omega$	$\sigma_{1/2}^2$	0,2
$^{11}\text{Be}(1/2^+)$	$1\hbar\omega$	$\pi_{3/2}^2\sigma_{1/2}$	3,0
$^{11}\text{Be}(1/2^-)$	$0\hbar\omega$	$\pi_{3/2}^2\pi_{1/2}$	2,1
$^{11}\text{Be}(3/2^-)$	$2\hbar\omega$	$\pi_{3/2}\sigma_{1/2}^2$	1,2
$^{12}\text{Be}(0_1^+)$	$2\hbar\omega$	$\pi_{3/2}^2\sigma_{1/2}^2$	2,2
$^{12}\text{Be}(0_2^+)$	$0\hbar\omega$	$\pi_{3/2}^2\pi_{1/2}^2$	4,0
$^{12}\text{Be}(1^-)$	$1\hbar\omega$	$\pi_{3/2}^2\pi_{1/2}\sigma_{1/2}$	3,1
$^{13}\text{Be}(1/2^-)$	$1\hbar\omega$	$\pi_{3/2}^2\pi_{1/2}\sigma_{1/2}^2$	3,2
$^{13}\text{Be}(5/2^+)$	$0\hbar\omega$	$(\pi_{3/2}^2\pi_{1/2}^2\sigma_{1/2})$	4,1
$^{13}\text{Be}(3/2^+)$	$2\hbar\omega$	$\pi_{3/2}^2\sigma_{1/2}^2\pi_{3/2}^*$	2,2+1
$^{14}\text{Be}(0_1^+)$	$0\hbar\omega$	$\pi_{3/2}^2\pi_{1/2}^2\sigma_{1/2}^2$	4,2
$^{14}\text{Be}(2^-)$	$1\hbar\omega$	$\pi_{3/2}^2\pi_{1/2}\sigma_{1/2}^2\pi_{3/2}^*$	3,2+1
$^{14}\text{Be}(0_2^+)$	$2\hbar\omega$	$\pi_{3/2}^2\sigma_{1/2}^2\pi_{3/2}^{*2}$	2,2+1

$\pi_{3/2}^2\pi_{1/2}^2$  and  $\pi_{3/2}^2\pi_{1/2}\sigma_{1/2}^1$ , respectively. These assignments are consistent with the results of molecular orbit models [17, 49] and those of cluster models [57, 59–61, 66]. For  $^{13}\text{Be}$  and  $^{14}\text{Be}$ , excited bands with developed cluster structures have been theoretically predicted by the AMD+VAP calculations [54, 65]. The band-head states,  $^{13}\text{Be}(1/2^-)$ ,  $^{13}\text{Be}(3/2^+)$ , and  $^{13}\text{Be}(5/2^+)$ , are regarded as  $\pi_{3/2}^2\pi_{1/2}\sigma_{1/2}^2$ ,  $\pi_{3/2}^2\sigma_{1/2}^2\pi_{3/2}^*$  and  $\pi_{3/2}^2\pi_{1/2}^2\sigma_{1/2}$ . And  $^{14}\text{Be}(0_1^+)$ ,

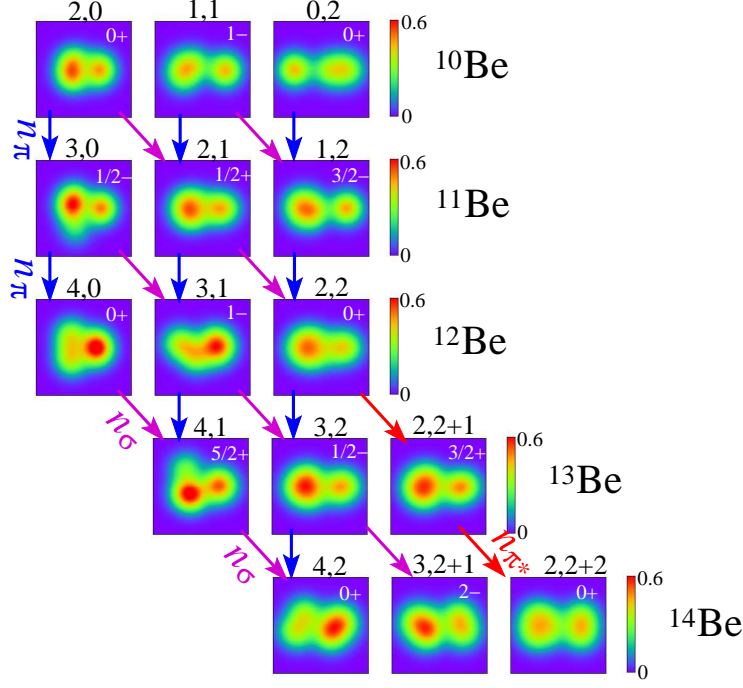


FIG. 19. Matter density distributions in the band-head states of Be isotopes obtained by the AMD+VAP using the MV1 ( $m = 0.65$ ,  $b = h = 0$ ) central and G3RS ( $u_1 = -u_2 = -3700$  MeV) spin-orbit interactions [48, 54–56, 65]. For  $^{10}\text{Be}$ , the results obtained using the MV1 ( $m = 0.62$ ,  $b = h = 0$ ) central and G3RS ( $u_1 = -u_2 = -3000$  MeV) spin-orbit interactions are shown. Panels for the states with  $\sigma_{1/2}^0$ ,  $\sigma_{1/2}^1$ ,  $\sigma_{1/2}^2$ ,  $\sigma_{1/2}^2\pi_{3/2}^*$ , and  $\sigma_{1/2}^2(\pi_{3/2}^*)^2$  configurations are aligned in the first, second, third, fourth, and fifth columns from the left based on the dominant MO configurations listed in Table I. The neutron numbers ( $n_\pi, n_\sigma + n_{\pi^*}$ ) in the  $\pi_{3/2,1/2^-}$ ,  $\sigma_{1/2^-}$ ,  $\pi_{3/2}^*$ -orbits are shown above each panel. Down arrows indicate the increase of  $\pi_{3/2,1/2^-}$ -orbit neutrons, and down-right arrows stand for the increase of the  $\sigma_{1/2^-}$  and  $\pi_{3/2}^*$ -orbit neutrons. The densities of intrinsic states are integrated with respect to the  $z$  axis and plotted on the  $x$ - $y$  plane in the unit of  $\text{fm}^{-2}$ . The axes of the intrinsic frame are chosen so as to be  $\langle x^2 \rangle \geq \langle y^2 \rangle \geq \langle z^2 \rangle$ .

$^{14}\text{Be}(2^-)$ , and  $^{14}\text{Be}(0_2^+)$  are described by the  $\pi_{3/2}^2\pi_{1/2}^2\sigma_{1/2}^2$ ,  $\pi_{3/2}^2\pi_{1/2}\sigma_{1/2}^2\pi_{3/2}^*$ , and  $\pi_{3/2}^2\sigma_{1/2}^2\pi_{3/2}^*$  configurations, respectively. Experimental data are not enough to assign band structures of  $^{13}\text{Be}$  and  $^{14}\text{Be}$ .

To see how the cluster structure is enhanced (suppressed) by  $\sigma(\pi)$ -orbit neutrons, we show density distributions of the intrinsic states in Fig. 19. The numbers ( $n_\pi, n_\sigma, n_{\pi^*}$ ) of

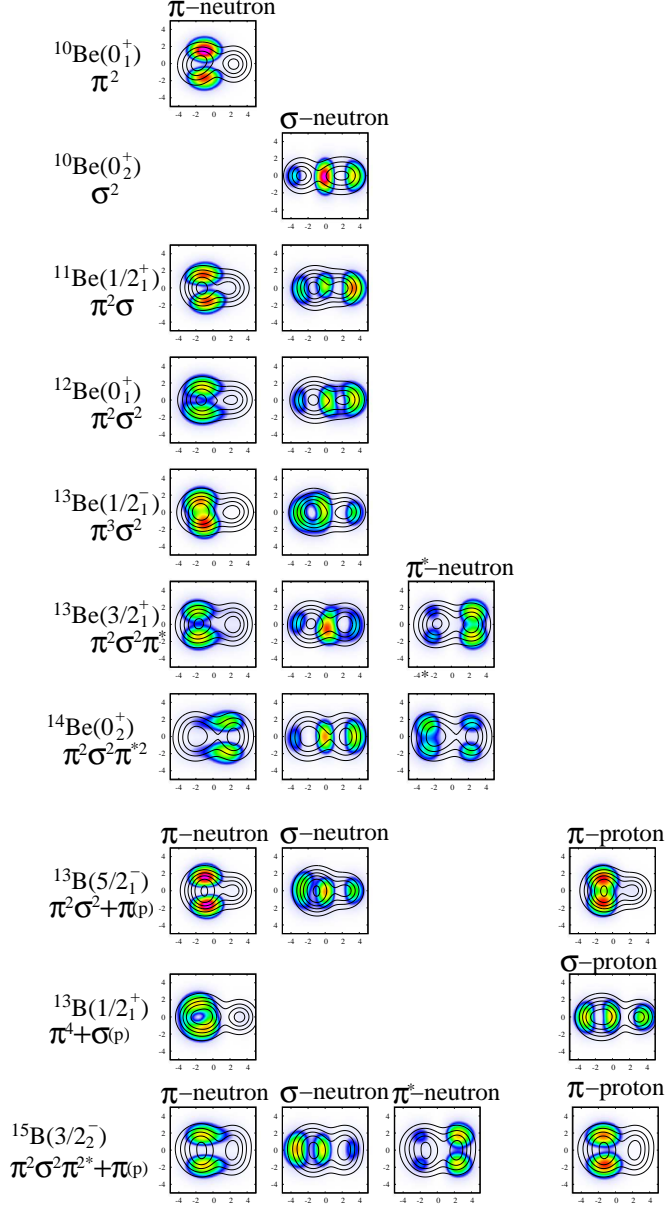


FIG. 20. Single-particle wave functions of valence neutrons in the MO  $\sigma$ -bond structures in Be and B isotopes as well as those in the  $^{10}\text{Be}(0_1^+)$  obtained by the AMD+VAP using the MV1 ( $m = 0.65$ ,  $b = h = 0$ ) central and G3RS ( $u_1 = -u_2 = -3700$  MeV) spin-orbit interactions [48, 54–56, 65, 174]. For  $^{10}\text{Be}$ , the results obtained using the MV1 ( $m = 0.62$ ,  $b = h = 0$ ) central and G3RS ( $u_1 = -u_2 = -3000$  MeV) spin-orbit interactions are shown. Single-particle wave functions in the band-head states are shown (except for  $^{13}\text{B}(5/2_1^-)$ ). The  $^{13}\text{B}(5/2_1^-)$  state is the band member of  $K^\pi = 3/2^-$  starting from the  $3/2_2^-$  state. The densities of intrinsic states are integrated with respect to the  $z$  axis and plotted on the  $x$ - $y$  plane. The single-particle densities of the molecular orbits are displayed in color maps. The total matter densities are shown by contour lines.

$\pi$ -,  $\sigma$ -,  $\pi^*$ -orbit neutrons are shown in the figure corresponding to the configurations listed in Table I. As clearly seen,  $\sigma$ -orbit and  $\pi^*$ -orbit neutrons enhance the cluster structure, whereas  $\pi$ -orbit neutrons suppress the cluster structure: the cluster structure is enhanced by  $n_\sigma$  increasing and enhanced further by  $n_\pi^*$  increasing, whereas it is suppressed as  $n_\pi$  increases.

Finally, we discuss energy levels of the band-head states labeled by the molecular orbit configurations. Figure 15 shows experimental excitation energies of  $^{10-12}\text{Be}$  and theoretical values of  $^{13}\text{Be}$  and  $^{14}\text{Be}$ . In the spherical shell model limit,  $0\hbar\omega$  configurations are the lowest, whereas  $1\hbar\omega$  and  $2\hbar\omega$  are excited configurations. The inversion between  $0\hbar\omega$ ,  $1\hbar\omega$ , and  $2\hbar\omega$  occurs in  $^{11-13}\text{Be}$ , and the energy spectra seem to be out of the normal ordering of the spherical shell model configurations. However, in the molecular orbit configurations in the developed cluster structure, the  $\sigma_{1/2}$ - and  $\pi_{1/2}$ -orbits almost degenerate (see Fig. 15(d)) and they compose the major shell on the top of the  $N = 6$  shell gap. It means that  $^{10}\text{Be}$  is regarded as a closed MO-shell ( $\pi_{3/2}$ -orbit) nucleus, whereas,  $^{11-13}\text{Be}$  are open MO-shell ( $\pi_{1/2}$ - and  $\sigma_{1/2}$ -orbits) nuclei, in which the neutron Fermi level exists at the major  $\sigma_{1/2}$ - $\pi_{1/2}$  shell. In the molecular orbit picture,  $^{10}\text{Be}(0_1^+)$ ,  $^{11}\text{Be}(1/2^+)$ ,  $^{11}\text{Be}(1/2^-)$ ,  $^{12}\text{Be}(0_1^+)$ ,  $^{12}\text{Be}(0_2^+)$ ,  $^{12}\text{Be}(1^-)$ ,  $^{13}\text{Be}(1/2^-)$ , and  $^{14}\text{Be}(0_1^+)$  are “normal” states described by major MO-shell configurations, and therefore, it is not surprising that they appear in low-energy regions. On the other hand,  $\pi_{3/2}$ -orbit holes and  $\pi_{3/2}^*$ -orbit particles are interpreted as particle-hole excited states in the molecular orbit configurations. For instance,  $^{10}\text{Be}(1^-)$ ,  $^{11}\text{Be}(3/2^-)$ ,  $^{14}\text{Be}(2^-)$  and  $^{14}\text{Be}(0_2^+)$  have excited molecular orbit configurations and they exist in relatively higher energy regions ( $E_x = 4 \sim 6$  MeV). The  $^{13}\text{Be}(3/2^+)$  state is the exception that the excited molecular orbit configuration is obtained in the low-energy region, probably, because of many-body correlations.

For  $^{13}\text{Be}$ , which is an unbound nucleus, experimental spectra and spin-parity assignments in the low-energy region are still controversial [80, 175–184]. An experimental report of a low-lying resonance with the abnormal spin-parity  $J^\pi = 1/2^-$  supports the breaking of the  $N = 8$  magic number [175].



#### 4. Analogous molecular orbit states in B isotopes

In excited states of B isotopes, MO  $\sigma$ -bond structures analogous to those of Be isotopes have been predicted. In B isotopes, the MO  $\sigma$ -bond structures are not so favorable as Be isotopes because of an additional proton, and therefore, they appear in excited states. For instance, AMD+VAP calculations predicted  $K^\pi = 3/2^-$  bands in highly excited states of  $^{13}\text{B}$  and  $^{15}\text{B}$  [54, 174]. These states are dominated by  $\pi^2\sigma^2$  and  $\pi^2\sigma^2\pi^{*2}$  neutron configurations, respectively, and regarded as analogous states of  $^{12}\text{Be}(0_1^+)$  and  $^{14}\text{Be}(0_2^+)$  with an additional proton in the  $\pi$ -orbit. Moreover,  $^{13}\text{B}(1/2^+)$  with an exotic cluster structure having a proton in the  $\sigma$ -orbit has been predicted. It is surprising that the molecular  $\sigma$ -orbit appears also in the proton configuration despite that protons are rather deeply bound in the neutron-rich systems.  $^{13}\text{B}(1/2^+)$  has a remarkably large deformation with  $^8\text{He}$  and  $\alpha$  clusters bonded by the  $\sigma$ -orbit proton, and it constructs the  $K^\pi = 1/2^+$  rotational band with a large moment of inertia. Intrinsic structures of these excited states of B isotopes are shown in Fig. 20. In the figure, the density distributions of single-particle wave functions are illustrated together with the total matter density. Also for  $^{11}\text{B}$ , cluster structures in excited states can be understood by the molecular orbit picture as discussed in Ref. [185].

#### B. Molecular orbitals in O, Ne and F isotopes

The success of the molecular orbit in Be isotopes strongly motivated the extension of this concept to other nuclei. One of the motivation of the extension is the universality of the molecular orbits. It is of interest and importance to investigate if the molecular orbit appears in other nuclei universally.

O, F and Ne isotopes are the good candidates of the molecular orbit, because the clustering of their stable nuclei  $^{16}\text{O}$ ,  $^{19}\text{F}$  and  $^{20}\text{Ne}$  are well known [3, 4, 139, 140, 186–188]. Different from Be isotopes, these isotopes can have the parity asymmetric cores,  $\alpha + ^{12}\text{C}$ ,  $\alpha + ^{15}\text{N}$  and  $\alpha + ^{16}\text{O}$ , respectively. Therefore, they should have new aspects caused by this asymmetry. In addition to this, these isotopes have much longer isotope chain than Be isotopes, and hence, have more valence neutrons. Here, after a short introduction of the clustering in stable  $^{16}\text{O}$ ,  $^{19}\text{F}$  and  $^{20}\text{Ne}$ , we summarize the AMD studies for neutron-rich O, Ne and F isotopes.

1.  $\alpha$  clustering in  $^{16}\text{O}$ ,  $^{20}\text{Ne}$  and  $^{19}\text{F}$

For a better understanding of the clustering in O, Ne and F isotopes, it is useful to review the clustering of their stable isotopes  $^{16}\text{O}$ ,  $^{20}\text{Ne}$  and  $^{19}\text{F}$ .

$^{16}\text{O}$  and  $^{20}\text{Ne}$  are famous for their asymmetric cluster structures of  $\alpha + ^{12}\text{C}$  and  $\alpha + ^{16}\text{O}$ . Because of the parity asymmetric configuration, they must constitute the parity doublet (a pair of the positive- and negative-parity bands) [139]. Many theoretical and experimental studies have been devoted to study the clustering in  $^{16}\text{O}$  and  $^{20}\text{Ne}$ , and the cluster band assignment is established well as summarized in Fig. 21 [189–191]. The ground state of

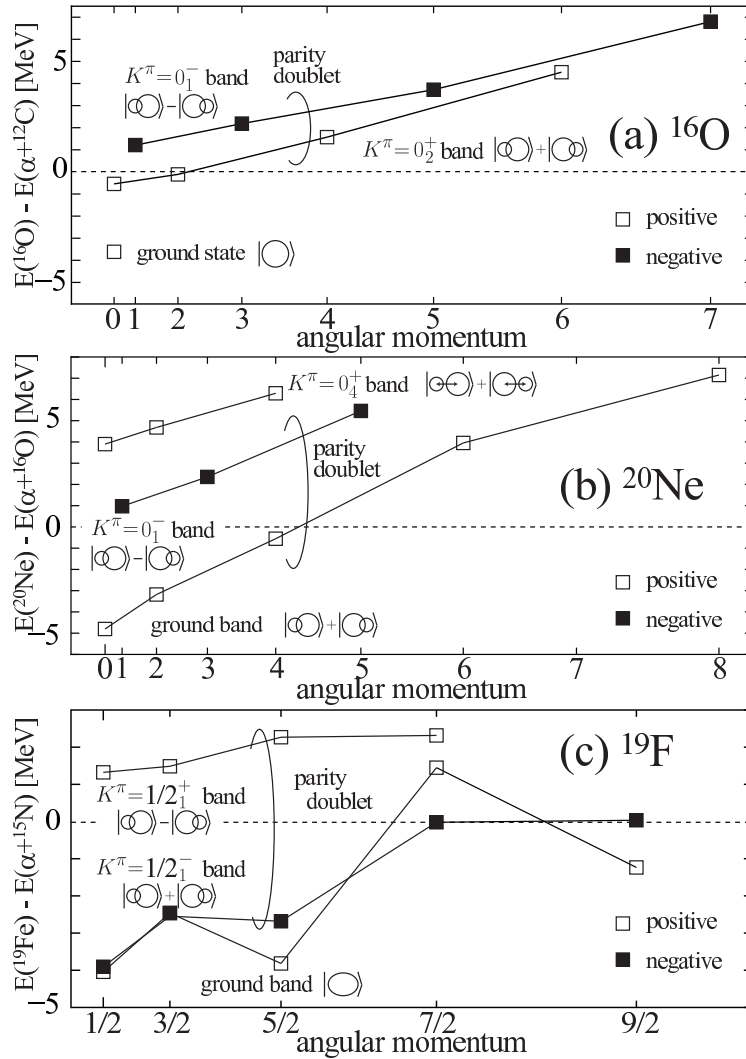


FIG. 21. Observed cluster bands in  $^{16}\text{O}$ ,  $^{20}\text{Ne}$  and  $^{19}\text{F}$ . Experimental data are taken from Ref. [189–191].

$^{16}\text{O}$  has the doubly closed shell configuration, but the  $0_2^+$  and  $1_2^-$  states at 6.0 and 9.6 MeV have prominent  $\alpha + ^{12}\text{C}(0_1^+)$  cluster structure. Two rotational bands with positive- and negative-parity ( $K^\pi = 0_2^+$  and  $0_1^-$  bands) are built on these states and constitute the parity doublet. In the case of  $^{20}\text{Ne}$ , the ground band and the  $K^\pi = 0_1^-$  band built on the  $1^-$  state at 5.8 MeV are regarded as the parity doublet. In addition to them, another cluster band ( $K^\pi = 0_4^+$  band), in which the relative motion between clusters is excited by  $2\hbar\omega$ , is built on the  $0_4^+$  state around 8.7 MeV.

Here, let us note the difference between  $^{20}\text{Ne}$  and lighter nuclei such as  $^{12}\text{C}$  and  $^{16}\text{O}$ . To understand the difference, the energies of the  $0_2^+$  state of  $^{12}\text{C}$  ( $3\alpha$  cluster state), the parity doublets of  $^{16}\text{O}$  and  $^{20}\text{Ne}$  and the ground states of those nuclei are summarized in Fig. 22. In this figure, since the ground state of  $^{20}\text{Ne}$  is assigned as the cluster state, one sees that

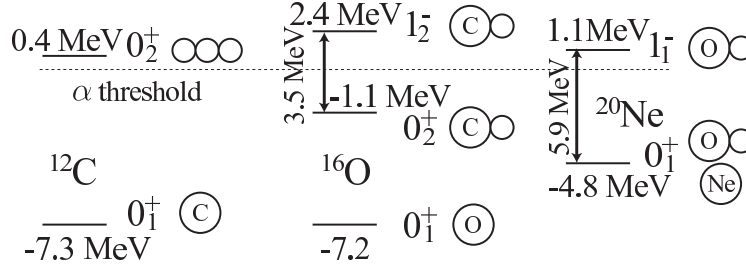


FIG. 22. Systematics of  $\alpha$  cluster states in  $^{12}\text{C}$ ,  $^{16}\text{O}$  and  $^{20}\text{Ne}$ . Numbers in the figure show the energy measured from the  $\alpha$  threshold.

the  $0^+$  state of  $^{20}\text{Ne}$  having shell structure illustrated in Fig. 2 looks missing in  $^{20}\text{Ne}$ , while it exists as the ground states in  $^{12}\text{C}$  and  $^{16}\text{O}$  (compare Fig. 22 with Fig. 2). This suggests the transient nature of the ground state of  $^{20}\text{Ne}$ . Namely, the ground state of  $^{20}\text{Ne}$  is not a pure  $\alpha$  cluster state but a mixture of the shell and  $\alpha$  cluster configurations. This transient nature is confirmed in another way. The energy of the  $\alpha$  cluster states of  $^{12}\text{C}$  (+0.4 MeV) and  $^{16}\text{O}$  (-1.1 MeV) are close to the  $\alpha$  threshold energy, but the ground state of  $^{20}\text{Ne}$  (-4.8 MeV) is much deeper than the  $\alpha$  threshold indicating stronger attraction between  $\alpha$  and  $^{16}\text{O}$  clusters. This stronger attraction induces the distortion of clusters leading to the mixing between cluster and shell configurations. Yet another evidence of the transient nature is the energy splitting of the parity doublets. As explained in Ref. [139], the energy splitting becomes smaller for enhanced cluster state, while it is enlarged for modest cluster state. It is clear that the splitting is enlarged in  $^{20}\text{Ne}$  (5.9 MeV) compared with that in  $^{16}\text{O}$  (3.5

MeV) indicating the reduction of clustering in the  $^{20}\text{Ne}$  ground state. The highlight of the discussion on  $^{22}\text{Ne}$  made in the following section is how this transient nature of the  $\alpha + ^{16}\text{O}$  clustering is affected and modified by the excess neutrons. It will alter the systematics of the  $\alpha$  clustering and change the energy splitting of the parity doublet.

$^{19}\text{F}$  can be regarded as the nucleus in which a proton hole is coupled to  $^{20}\text{Ne}$ . In the ground state, this proton hole occupies the  $sd$ -shell, *i.e.* three nucleons occupy  $sd$ -shell on top of  $^{16}\text{O}$  core as illustrated in Fig. 23 (a). Since the valence nucleons cannot form  $\alpha$

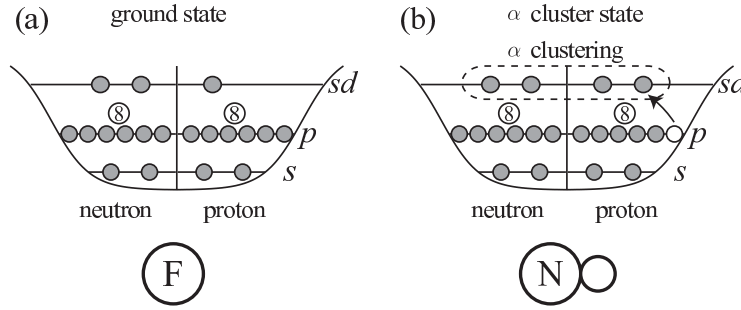


FIG. 23. Particle-hole configurations in the ground and the first excited states of  $^{19}\text{F}$ .

particle, the cluster correlation in the ground state is rather weak and the shell model gives reasonable description [187], although the contribution from the  $t + ^{16}\text{O}$  is not negligible. If a proton hole occupies  $p$ -shell as illustrated in Fig. 23 (b), in other words, a proton is excited from  $p$ - to  $sd$ -shell across  $Z = 8$  shell gap, valence nucleons in  $sd$ -shell form an  $\alpha$  particle to generate the  $\alpha + ^{15}\text{N}$  cluster state [4]. Since the energy gain owing to the  $\alpha$  clustering is large enough to compensate the energy loss due to the proton excitation, the energy of this proton hole configuration is comparable with the ground state. As a result, the excitation energy of the first excited state having this configuration ( $1/2_1^-$  state) is as small as 110 keV. The  $\alpha$  cluster bands in  $^{19}\text{F}$  have been also studied in detail and assigned as shown in the lower panel of Fig. 21 [190]. Thus, it is reminded that a proton excitation across  $Z = 8$  shell gap triggers the clustering in the case of F isotopes.

## 2. $\alpha$ clustering in $^{22}\text{Ne}$

One of the earliest extension of the molecular-orbit picture to the nuclei other than Be isotopes was suggested for Ne isotopes by von Oertzen [11, 17]. His idea is based on the

threshold energies in Ne isotopes shown in Fig. 24. In  $^{21}\text{Ne}$ , one sees that the  $^5\text{He}^*(3/2^-) +$

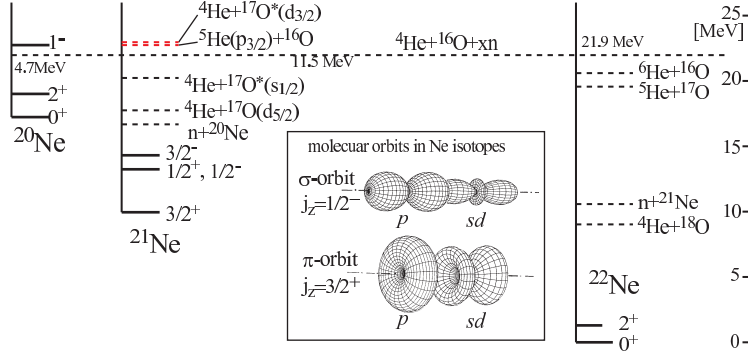


FIG. 24. Solid lines show the ground and excited states of  $^{20}\text{Ne}$ ,  $^{21}\text{Ne}$  and  $^{22}\text{Ne}$ , while dashed lines show threshold energies. Figure in the inset shows the molecular orbits that are composed from the  $p_{3/2}$  orbit around  $^4\text{He}$  and the  $d_{3/2}$  orbit around  $^{16}\text{O}$ . This figure is reconstructed from Ref. [11].

$^{16}\text{O}$  and  $^4\text{He} + ^{17}\text{O}^*(3/2^+)$  thresholds energies are almost degenerated at approximately 1 MeV above the  $^4\text{He} + ^{16}\text{O} + n$  threshold. This implies that the valence neutron occupying  $sd$ -orbit around  $^{16}\text{O}$  cluster and that occupying  $p$ -orbit around  $^4\text{He}$  cluster can be shared by these two clusters forming the molecular orbit. One also sees similar near degeneracy of the  $^5\text{He} + ^{17}\text{O}$  and  $^4\text{He} + ^{18}\text{O}$  thresholds in  $^{22}\text{Ne}$ . Note that this matching of the threshold energy is inevitable for symmetric clusters such as Be isotopes, but not for the asymmetric clusters. In an analogous way to Be isotopes, the parallel and transverse alignment of these two orbits generate  $\sigma$ - and  $\pi$ -orbits as illustrated in the inset of Fig. 24. By considering the combinations of these molecular orbits, he suggested a possible assignment of cluster bands in  $^{21}\text{Ne}$  and  $^{22}\text{Ne}$  [11, 192].

To test whether the suggested molecular orbits are really formed in Ne isotopes and to identify the cluster bands, AMD calculation was performed for  $^{22}\text{Ne}$  [198] using the Gogny D1S effective interaction. The band assignment by the AMD calculation is summarized in Fig. 25 together with the observed candidates of the cluster bands. The result is summarized as follows. (1) In the ground band, the valence neutrons reduces the  $\alpha + ^{16}\text{O}$  clustering and make the structure more like shell model state. (2) On the other hand, in the excited state, valence neutrons occupy the  $\sigma$ -orbit and enhance the  $\alpha + ^{16}\text{O}$  clustering. Three rotational bands around the  $\alpha + ^{18}\text{O}$  threshold are regarded as the cluster bands with covalent bonding,

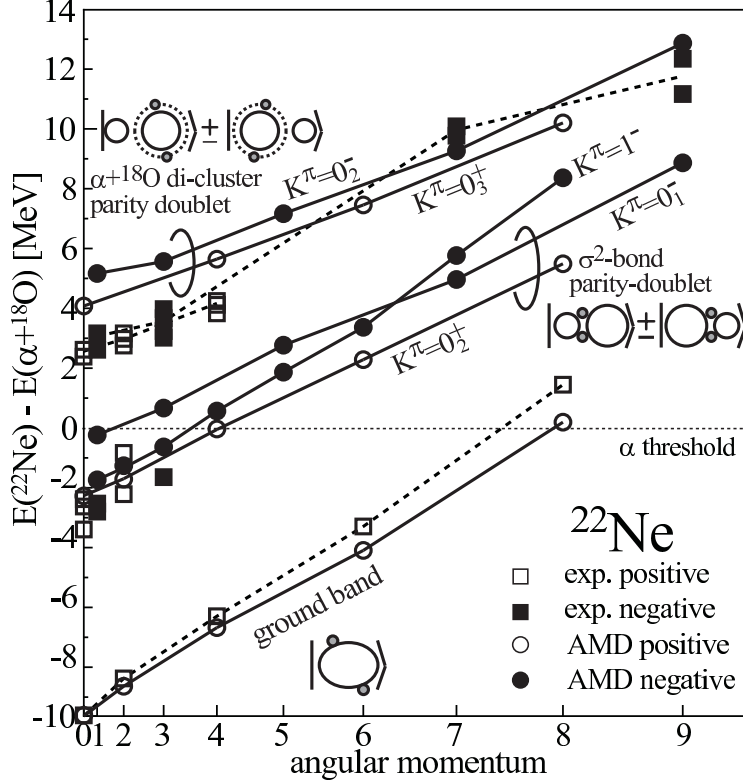


FIG. 25. Calculated and observed cluster states in  $^{22}\text{Ne}$ . Boxes show the experimental data [193–197], while the circles show the AMD result. This figure is reconstructed from the data presented in Ref. [198].

which we denote by  $\sigma$ - and  $\sigma^2$ -bond bands. (3) Another group of cluster bands appears at approximately 5 MeV above the  $\alpha + ^{18}\text{O}$  threshold. In those bands the valence neutrons orbit only around  $^{16}\text{O}$ , and hence, regarded as the ordinary two cluster system having  $\alpha + ^{18}\text{O}$  di-cluster configuration. We denote them by di-cluster bands. Because of the parity asymmetric intrinsic structure, the  $\sigma$ -,  $\sigma^2$ -bond bands and di-cluster bands constitute the parity doublet.

The structure of the ground band and  $\sigma$ -,  $\sigma^2$ -bands become clear by looking at the core and valence neutron densities shown in Fig. 26. Here, we define the most weakly bound two neutrons as valence neutrons and the remaining 20 nucleons as the  $^{20}\text{Ne}$  core which are plotted by color plot and contour lines, respectively. In the ground state, the valence neutrons occupy the orbit which have a node along the symmetry axis (Fig. 26 (a)). This orbit has  $sd$ -shell nature and may correspond to the  $\pi$ -orbit illustrated in Fig. 24. However, the system has the parity symmetric shape and the  $\alpha$  clustering of  $^{20}\text{Ne}$  core is lost indicating

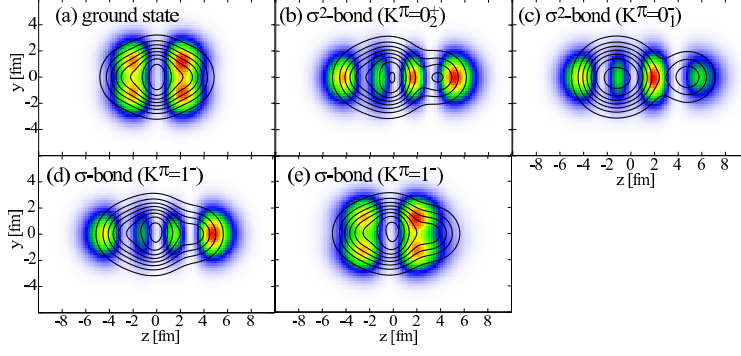


FIG. 26. Intrinsic density distributions of  $^{22}\text{Ne}$  for the band head states of (a) the ground band, (b)  $K^\pi = 0_2^+$   $\sigma^2$ -bond band, (c)  $K^\pi = 0_1^-$   $\sigma^2$ -bond band, and (d)(e)  $K^\pi = 1^-$   $\sigma$ -bond band. Solid lines show the density distribution of the  $^{20}\text{Ne}$  core, while the color plots show that of valence neutrons. This figure is reconstructed from the data presented in Ref. [198].

the deformed mean-field nature of the ground state. Indeed, the calculated properties of this valence neutron orbit listed in Tab. II is in good accordance with the Nilsson orbit with the asymptotic quantum number of  $[Nn_zm_l\Omega^\pi] = [211\ 3/2^+]$ . Here, the amount of the positive-parity component  $p^+$  and the angular momenta of the valence neutron orbit  $\phi_i$  are defined as

$$p^+ = |\langle \phi_i | \frac{1 + P_x}{2} | \phi_i \rangle|^2, \quad (22)$$

$$j(j+1) = \langle \phi_i | \hat{j}^2 | \phi_i \rangle, \quad \Omega = \sqrt{\langle \phi_i | \hat{j}_z^2 | \phi_i \rangle}, \quad (23)$$

$$l(l+1) = \langle \phi_i | \hat{l}^2 | \phi_i \rangle, \quad m_l = \sqrt{\langle \phi_i | \hat{l}_z^2 | \phi_i \rangle}. \quad (24)$$

In other words, when the valence neutrons occupy  $\pi$ -orbit, they diminish the  $\alpha$  clustering of the core and the system exhibit the deformed mean-field nature. Because of this symmetric shape, we have not obtained the negative-parity partner of the ground band that constitutes the parity doublet. As already discussed in the section III B, the reduction of  $\alpha$  clustering in the ground state can also be observed as the reduction of the  $B(E2)$  and the proton radius.

When the valence neutrons are excited, the structure is drastically changed. In the  $\sigma^2$ -bond bands with positive parity (Fig. 26 (b)), two valence neutrons occupy the orbit having three nodes along the symmetry axis which exhibits  $pf$ -shell nature. This valence neutron orbit induces strong  $\alpha$  clustering as clearly observed in the core density shown in Fig. 26 (b). Interestingly, because of the strong asymmetry of the core, this valence neutron orbit is a

TABLE II. Properties of the valence neutron orbits shown in Fig. 26 (a)-(e). The single-particle energy  $\varepsilon$  is given in MeV, and other quantities are defined by Eq. (22)-(24). The Nilsson asymptotic quantum numbers  $[Nn_zm_l\Omega^\pi]$  deduced from these properties are also given. The data is taken from Ref. [198].

orbit	$\varepsilon$	$p^+$	$j$	$l$	$m_l$	$\Omega$	$[Nn_zm_l\Omega^\pi]$
(a)	-8.9	0.94	2.5	2.0	1.1	1.5	$[211\ 3/2^+]$
(b)	-5.6	0.36	2.9	2.4	0.2	0.5	
(c)	-6.5	0.49	2.8	2.3	0.1	0.5	
(d)	-3.4	0.21	2.8	2.4	0.2	0.5	
(e)	-7.9	0.90	2.3	2.1	1.0	1.6	$[211\ 3/2^+]$

mixture of the positive- and negative-parity components (Tab. II) and cannot be interpreted as a single Nilsson orbit. It is noteworthy that the molecular-orbit picture ( $\sigma$ -orbit shown in Fig. 24) [11] gives a natural and reasonable interpretation of this orbit. Because of the parity asymmetry, the negative-parity states ( $K^\pi = 0_1^-$  band) shown in Fig. 26 (c) accompany with the positive-parity states to constitute the  $\sigma^2$ -bond parity doublet. It is interesting to note that the valence neutron density shown in Fig. 26 (c) indicates that the probability is largest in between  $^4\text{He}$  and  $^{16}\text{O}$  clusters to bond them, namely covalency. Thus, we are able to conclude that the valence neutrons in  $\pi$ -orbit ( $sd$ -shell) diminish the clustering, while those in  $\sigma$ -orbit induce it. This is confirmed from the structure of the  $K^\pi = 1^-$  band with  $\sigma$ -bond shown in Fig. 26 (d) and (e) in which a valence neutron occupies the  $\pi$ -orbit and the other occupies  $\sigma$ -orbit. A valence neutron in  $\sigma$ -orbit induces the moderate clustering of the core but not as prominent as the  $\sigma^2$ -bond ( $K^\pi = 0^\pm$ ) bands because another valence neutron in  $\pi$ -orbit reduces it. Above these molecular-orbit bands, we also obtained the atomic-orbit bands ( $K^\pi = 0_3^+$  and  $0_2^-$ ) as similar to the  $\alpha + ^8\text{He}$  di-cluster states in  $^{12}\text{Be}$ . In these bands, two valence neutrons orbit only around the  $^{16}\text{O}$  cluster analogous to the ionic bonding of atomic molecule.

We also note the energy splitting of the parity doublets (the energy difference between the positive- and negative-parity states which constitute the doublet). In  $^{22}\text{Ne}$ , the splitting of the  $\sigma^2$ -bond bands is approximately 2 MeV and that of the  $\alpha + ^{18}\text{O}$  di-cluster bands is



approximately 1 MeV, which are much smaller than the 6 MeV splitting in  $^{20}\text{Ne}$ . The small splitting of the  $\alpha + ^{18}\text{O}$  di-cluster bands is due to their much enhanced clustering compared to the  $^{20}\text{Ne}$  doublet. In the case of the  $\sigma^2$ -bond bands, the valence neutrons in  $\sigma$ -orbit prevent the reduction of the inter-cluster distance between  $\alpha$  and  $^{16}\text{O}$  clusters, because it enlarges the kinetic energy of the valence neutrons. As a result, the splitting of the  $\sigma^2$ -bond bands is also kept small.

As shown in Fig 25, the candidates of these cluster bands are reported by the experiments [193–197, 199, 200]. Several states below the  $\alpha$  threshold energy are reported as the candidates of the  $\alpha$  cluster states by the  $\alpha$  transfer reaction on  $^{18}\text{O}$  [193, 194]. They have tens times larger  $\alpha$  reduced width amplitude ( $\alpha\text{RWA}$ ) than the ground state. Since the  $\alpha\text{RWAs}$  of the molecular-orbit states with  $\sigma$ - and  $\sigma^2$ -bond by AMD show the qualitative agreement with the observation, the observed  $\alpha$  cluster states should correspond to the molecular-orbit states with  $\sigma$ - and  $\sigma^2$ -bond discussed above. They will also have large  $^6\text{He}$  reduced width amplitude to be confirmed by the experiment, because of covalent nature of the  $\sigma$  orbit. Above these  $\sigma$ -bond bands, the di-cluster bands are confirmed by the  $\alpha$  resonant scattering. AMD results and also other theoretical calculations [201–203] show good agreement with the observed energies, moment of inertia and  $\alpha\text{RWA}$  [195–197, 200].

### 3. $\alpha$ clustering in O isotopes

The structure of neutron-rich O isotope gives us a good insight to the relationship between the molecular-orbit and atomic-orbit bands. Figure 27 summarizes the assignment of the cluster bands in  $^{18}\text{O}$  and  $^{20}\text{O}$  obtained by the AMD study [204]. In  $^{18}\text{O}$ , a pair of the positive- and negative-parity cluster bands are built on the  $0_2^+$  and  $1_1^-$  states 2.2 MeV below and 2.4 MeV above the  $\alpha$  threshold, respectively. The intrinsic density distribution of these band-head states are shown in Fig. 28 (b) and (c). Compared to the ground state (Fig. 28 (a)), it is clear that those states have pronounced  $\alpha$  cluster structure, and positive- and negative-parity states have similar intrinsic structure to constitute the parity doublet. It must be noted that the valence neutrons are well confined around  $^{12}\text{C}$  cluster differently from the  $\sigma$ -orbit of  $^{22}\text{Ne}$  shown in Fig. 26 (c). In other words, these states are regarded as the atomic orbit state or an ordinary di-cluster state with  $\alpha + ^{14}\text{C}$  configuration. In Ref. [204], it was also shown that energy of the molecular-orbit-like configuration is higher than the

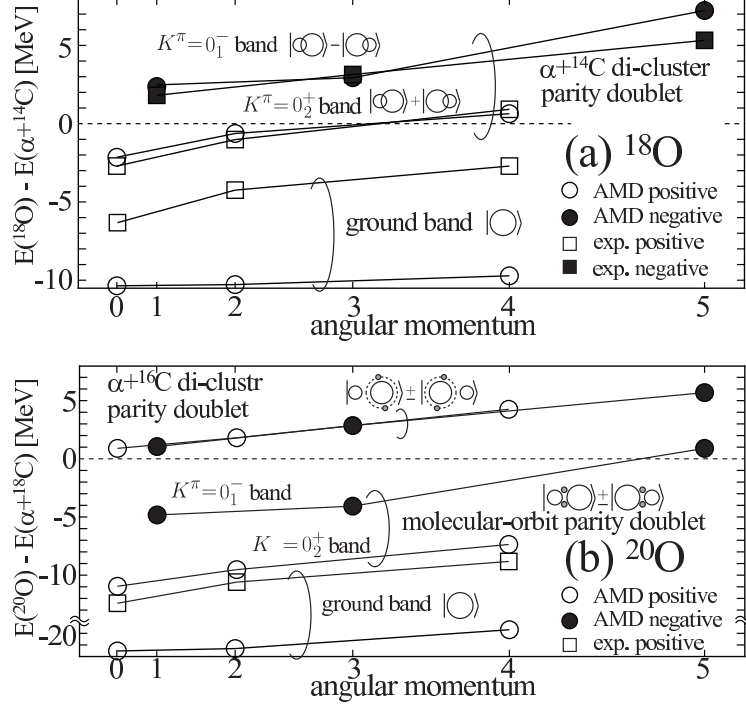


FIG. 27. Calculated and observed cluster states in  $^{18}\text{O}$  and  $^{20}\text{O}$ . Boxes show the experimental data, while the circles show the AMD result. Energy is measured from the  $\alpha$  threshold. This figure is reconstructed from the data presented in Ref. [204].

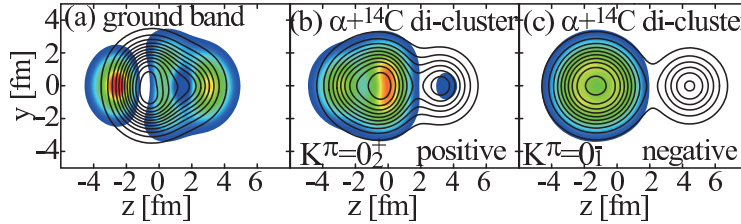


FIG. 28. Intrinsic density distributions of  $^{18}\text{O}$  for the band head states of (a) the ground band, (b) the  $K^\pi = 0_2^+$  band with  $\alpha + ^{14}\text{C}$  clustering and (c) the  $K^\pi = 0_1^-$  band that is paired with the  $K^\pi = 0_2^+$  band. Solid lines show the density distribution of the  $^{16}\text{O}$  core, while the color plots show that of valence neutrons. This figure is reconstructed from the data presented in Ref. [204].

$\alpha + ^{14}\text{C}$  configuration and located at approximately 10 MeV above the  $\alpha$  threshold. Thus, the order of the molecular-orbit and atomic-orbit bands are inverted in  $^{18}\text{O}$ . The origin of this inversion is attributed to the shell effect of  $^{14}\text{C}$  cluster. Because of the magicity of the neutron number  $N = 8$ , the last two neutrons in  $^{14}\text{C}$  are tightly bound and are

hardly picked out from  $^{14}\text{C}$  cluster. As a result, the  $\alpha + ^{14}\text{C}$  cluster states appear at smaller excitation energies than the molecular-orbit configurations.

Above explanation is verified by investigating the clustering systematics of  $^{20}\text{O}$ . Since the last two neutrons in  $^{16}\text{C}$  are much weakly bound than those of  $^{14}\text{C}$ , we expect that the order of molecular-orbit and atomic-orbit bands is reverted and becomes the same order with the  $^{22}\text{Ne}$  case. This expectation is confirmed in the results for  $^{20}\text{O}$  summarized in Fig. 27 (b) and Fig. 29.  $^{20}\text{O}$  has a parity doublet of molecular-orbit configuration of  $\alpha + ^{14}\text{C} + 2n$  whose band-head

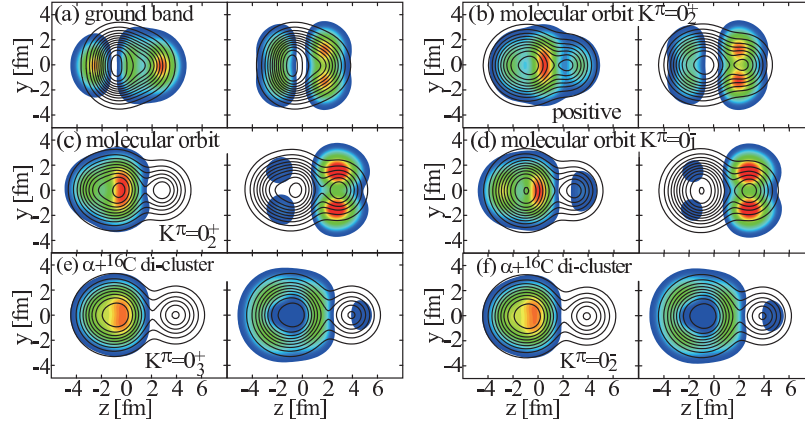


FIG. 29. Intrinsic density distributions of  $^{20}\text{O}$  for the band head states of (a) the ground band, (b)(c) the  $K^\pi = 0_2^+$  molecular orbit band, (d) the  $K^\pi = 0_1^-$  molecular orbit band that is paired with the  $K^\pi = 0_2^+$  band, and a pair of the atomic orbit bands (e)  $K^\pi = 0_3^+$  and (f)  $K^\pi = 0_2^-$ . Solid lines show the density distribution of the  $^{16}\text{O}$  core, while the color plots show that of valence neutrons. In each panel, the left side shows the density distribution of the second weakly bound two neutrons and the right side shows the most weakly bound two neutrons. This figure is reconstructed from the data presented in Ref. [204].

energies are approximately 10 and 5 MeV below the  $\alpha$  threshold, respectively. The positive-parity states are the admixture of the molecular-orbit and atomic-orbit configurations which are respectively shown in Fig. 29 (b) and (c). The configuration (b) does not have prominent clustering of the core ( $\alpha + ^{14}\text{C}$ ), but the last two valence neutrons (right panel of Fig. 29 (b)) are distributed to the entire system showing molecular-orbit-like bonding. Another configuration shown in Fig. 29 (c) has more developed cluster core. The last two neutrons are localized around the  $\alpha$  cluster and another two are around the  $^{12}\text{C}$  cluster, hence it appears more like  $^6\text{He} + ^{14}\text{C}$  di-cluster system. The negative-parity partner of molecular-

orbit band denoted by  $K^\pi = 0_1^-$  band in Fig. 27 is easily identified, because it is dominated by the configuration shown in the panel (d) which looks almost identical to the panel (c).

Above these molecular-orbit-like doublet, the atomic-orbit doublet having  $\alpha + {}^{16}\text{C}$  configuration appears in the vicinity of the  $\alpha$  threshold. The intrinsic configurations of the positive- and negative-parity states shown in the panels (e) and (f) look almost identical to each other. Four valence nucleons are almost confined in the atomic orbit around the  ${}^{12}\text{C}$  cluster indicating the formation of the  $\alpha + {}^{16}\text{C}$  configuration. This energetical order of molecular-orbit and atomic-orbit bands is common to those of  ${}^{22}\text{Ne}$  and  $\text{Be}$  isotopes showing that the underlying shell effect influences the formation of the molecular- and atomic-orbits and clustering systematics. Experimentally, the cluster states of  ${}^{18}\text{O}$  have been investigated by many authors based on the  $\alpha$ -transfer, resonant scattering and enhanced  $E1$  transitions [200, 205–213]. Fig. 27 (a) shows that present results reasonably agree with these experimental candidates, supporting the above-mentioned clustering systematics. Unfortunately, the experimental information for  ${}^{20}\text{O}$  is rather obscure [214–217], and we expect further experimental studies will reveal the clustering systematics and the relationship between the molecular-orbit and atomic-orbit states.

#### 4. $\alpha$ clustering in neutron-rich $F$ isotopes

The neutron drip line of  $F$  and  $\text{Ne}$  isotopes are extended beyond  $N = 20$  shell gap where the magicity of neutron number  $N = 20$  is lost and the shell gap between  $sd$  and  $pf$ -shells is quenched. Since the  $2\alpha$  clustering in neutron-rich  $\text{Be}$  isotopes is also closely related to the breakdown of the  $N = 8$  magic number, it is very interesting to investigate how the clustering in  $F$  and  $\text{Ne}$  isotopes are affected by the breakdown of the neutron magic number  $N = 20$ . In the section III B, it was already discussed that the ground state clustering in neutron-rich  $\text{Ne}$  isotopes are enhanced owing to the breakdown of the  $N = 20$  magic number. Here, we discuss how the breakdown of the  $N = 20$  magic number affects the excited states of  $F$  isotopes.

As already explained above, the  $\alpha$  cluster state of  ${}^{19}\text{F}$  must have a proton hole in  $p$ -shell. Therefore, we here discuss how the proton hole states of neutron-rich  $F$  isotopes evolve as function of neutron number [218]. Figure 30 shows the calculated partial level scheme of (a)  ${}^{21}\text{F}$  and (b)  ${}^{23}\text{F}$  where the disconnected circles show the states without proton hole, while

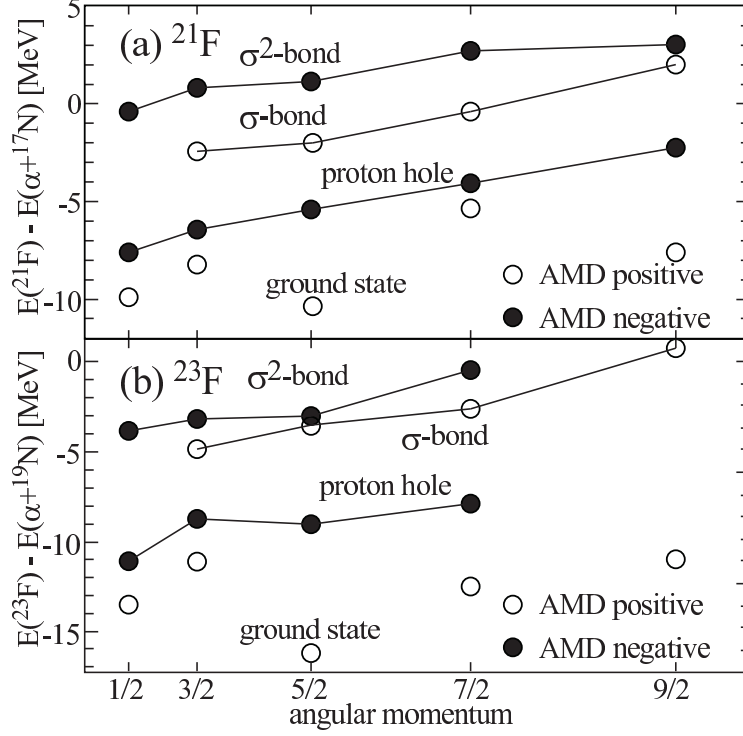


FIG. 30. Calculated partial level scheme of  $^{21}\text{F}$  and  $^{23}\text{F}$ . Disconnected circles show the states in which a proton and all valence neutrons are occupying the  $sd$ -shell. Connected circles show the rotational band denoted by “proton hole”, “ $\sigma$ -bond” and “ $\sigma^2$ -bond” in which a proton is excited from  $p$ -shell to  $sd$ -shell. This figure is reconstructed from the data presented in Ref. [218].

the connected circles show the proton hole states which are classified into three rotational bands denoted by “proton hole”, “ $\sigma$ -bond” and “ $\sigma^2$ -bond”. For the understanding of their structures, Fig. 31 schematically shows the single-particle configurations of  $^{21}\text{F}$ , and Fig. 32 shows their core and valence-neutron density distributions. While the ground state of  $^{21}\text{F}$  has no proton hole in  $p$ -shell, the rotational band denoted by “proton hole” has it as illustrated in Fig. 31 (a) and (b). Different from the case of  $^{19}\text{F}$ , the proton excitation from  $p$  to  $sd$ -shell does not induce the clustering as seen from the density distribution shown in Fig. 32 (b). This is due to the two valence neutrons occupying the  $sd$ -shell which energetically unfavour the deformation caused by the clustering. This role of valence neutrons is the same as the cases of the ground states of  $^{10}\text{Be}$  and  $^{22}\text{Ne}$ . When one or two valence neutrons are promoted into  $pf$ -shell together with the proton excitation, the result is very different. The  $\sigma$ -bond and  $\sigma^2$ -bond rotational bands have one and two valence neutrons in  $pf$ -shell (Fig.

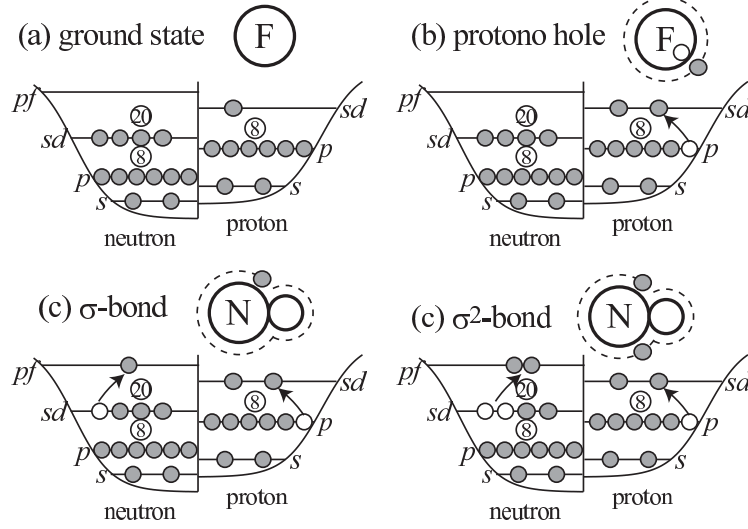


FIG. 31. Configurations of the ground state, proton hole,  $\sigma$ -bond and  $\sigma^2$ -bond rotational bands of  $^{21}\text{F}$  in terms of the single particle orbit.

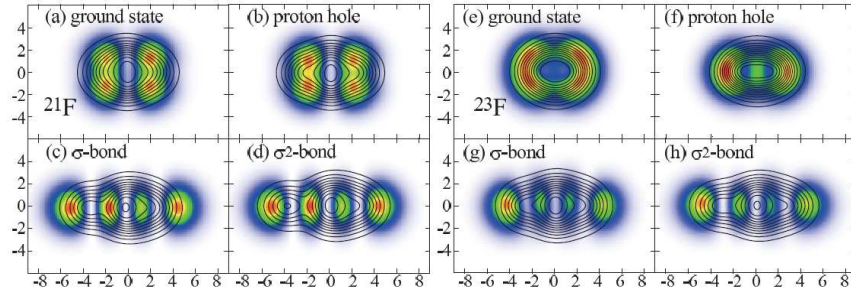


FIG. 32. Density distributions of the  $^{19}\text{F}$  core (contour plot) and those of the last valence neutron (color plot) in the ground state, proton hole,  $\sigma$ -bond and  $\sigma^2$ -bond rotational bands of  $^{21}\text{F}$  and  $^{23}\text{F}$ . This figure is reconstructed from the data presented in Ref. [218].

31 (c) and (d)), respectively. As clearly seen in their density distributions (Fig. 32 (c) and (d)), these neutron excitation induce the clustering of the  $^{19}\text{F}$  core. It is also noted that the clustering is more enhanced as the number of valence neutron in this orbit increases. Hence, we recognize that this valence neutron orbit is quite analogous to the  $\sigma$ -orbit in  $^{22}\text{Ne}$ ; They have similar density distribution and induce the clustering. The situation is common to  $^{23}\text{F}$ , where the proton hole,  $\sigma$ - and  $\sigma^2$ -bond bands also appear, and the clustering of the core is also induced as seen in their density distributions shown in Fig. 32 (e)-(h).

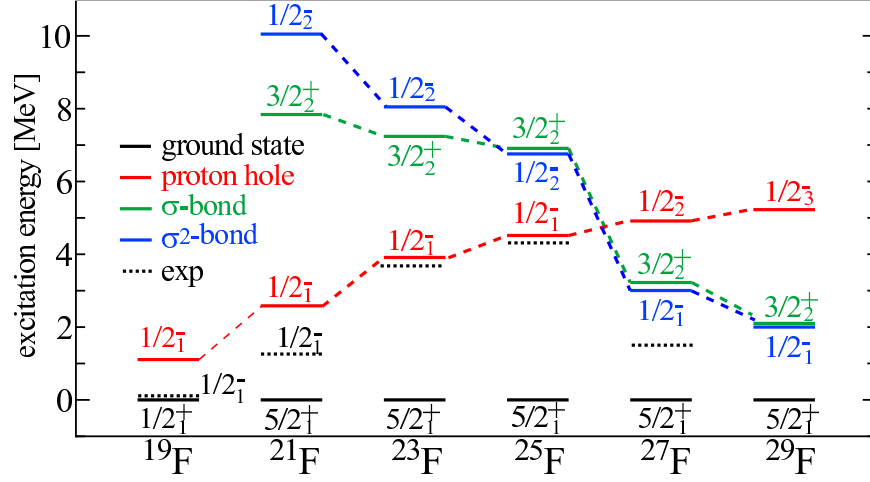


FIG. 33. Excitation energies of the band head states of the proton hole,  $\sigma$ -bond and  $\sigma^2$ -bond rotational bands in neutron-rich F isotopes as function of the neutron number. This figure is reconstructed from the data presented in Ref. [218].

Similar calculations were performed up to  $^{29}\text{F}$  and it was found that the proton hole,  $\sigma$ - and  $\sigma^2$ -bond bands always appear in the isotopes. Figure 33 shows the energies of the band-head states of these bands. It is interesting that the energies of the  $\sigma$ - and  $\sigma^2$ -bond bands dramatically decrease toward neutron drip line, while those of the proton hole band gradually increase. This characteristic behavior of the molecular-orbit bands is closely related to the breakdown of  $N = 20$  magic number explained in the previous section, and summarized as follows. (1) As one approaches to the neutron-drip line, the neutron Fermi level naturally goes up, which reduces the excitation energy that costs to promote neutron from  $sd$  to  $pf$ -shell or  $\sigma$ -orbit. (2) In addition to this, in the vicinity of the island of inversion, the  $N = 20$  shell gap is quenched or disappears, that further reduces the energy needed for neutron excitation. (3) Once the neutrons are promoted into  $pf$ -shell or  $\sigma$ -orbit, it induces the clustering of the core. This brings about the additional binding energy which compensates the energy used for neutron excitation. At the same time, the clustering brings about the large deformation that further reduces the energy of the  $pf$ -shell. Owing to these cooperative effects, the calculation predicts the great energy reduction of the molecular-orbit states near the neutron drip line of F isotopes.

Up to now, the experimental data is rather obscure for F isotopes. However, there are several possible candidates are reported. The proton hole  $1/2^-$  states in  $^{19}\text{F}$  and  $^{21}\text{F}$  are well

identified at 0.1 and 1.1 MeV, respectively [219, 220]. By several experiments, the candidates of the  $1/2^-$  states are reported at 3.4 MeV in  $^{23}\text{F}$  [221, 222] and 4.2 MeV in  $^{25}\text{F}$  [223, 224]. Those excitation energies are gradually going up as neutron number increases and agree with the trend of the calculated proton hole states. An experiment [225] reports the possible low-lying negative-parity state in  $^{27}\text{F}$  at 1.3 MeV. The energies of the  $1/2^-$  candidates look discontinuously dropping at  $^{27}\text{F}$  which agrees with the level crossing between the proton hole band and  $\sigma^2$ -bond band predicted by the present calculation. Although the present data does not enough to identify the molecular-orbit bands, it is enough to motivate further theoretical and experimental studies. For example, the proton knockout reaction from  $^{30}\text{Ne}$  is very interesting and useful to identify the molecular states of  $^{29}\text{F}$ . Since the dominance of the neutron  $2\hbar\omega$  configuration (two neutrons in  $pf$ -shell) is experimentally established well, we can expect that a proton knockout from  $p$ -shell will strongly populates the  $\sigma^2$ -bond band of  $^{29}\text{F}$ .

### C. Three center systems

In this section, we discuss the linear-chain states in C isotopes, which are the most famous exotic structures expected in three cluster systems.

About 60 years ago, Morinaga suggested that the Hoyle state (the  $0_2^+$  state of  $^{12}\text{C}$ ) has the linear-chain structure, in which three  $\alpha$  clusters are linearly aligned [19, 20]. However, the cluster model studies [226–229] revealed that the Hoyle state is not a linear-chain state but a dilute gas-like state, where three  $\alpha$  clusters are very weakly interacting and do not have definite spatial configuration. In addition to this, the AMD [230] and FMD [58] calculations showed that the linear-chain of  $3\alpha$  particles is unstable against the bending motion (deviation from the linear alignment). As a result, they found that the highly excited  $0^+$  state above the Hoyle state has a bent-armed shape. Although the recent study based on the concept of the non-localized clustering [231] shed a new insight into the linear-chain, up to now, no positive evidence was observed for the linear-chain formation in  $^{12}\text{C}$ .

In these decades, the success of the molecular-orbit in Be isotopes strongly motivated the search for the linear chain in neutron-rich C isotopes [232], because the glue-like role of excess neutrons may stabilize the linear chain. Itagaki *et al.* [22] discussed the stability of linear-chain structures based on the molecular-orbit model. They found that the combination



of the excess neutrons in the  $\pi$  and  $\sigma$  orbits stabilizes the linear-chain structure against both of the breathing and bending motions, and concluded that the  $^{16}\text{C}^*$  with  $\pi_{3/2}^2\sigma_{1/2}^2$  configuration is the most promising candidate of the linear-chain state. Also, in other neutron-rich C isotopes, many theoretical studies predict the linear-chain formation.  $^{13}\text{C}$  was investigated using  $3\alpha+n$  cluster model and a bent linear-chain band was suggested [233, 234]. Relativistic Hartree and non-relativistic Hartree-Fock calculations were also performed for  $^{15,16}\text{C}$  and  $^{20}\text{C}$  [24, 235] which confirmed the stability of the linear chain within the mean-field approximation.

Compared to these theoretical models, AMD has several advantages. It can investigate the linear-chain formation without any *a priori* assumption on the clustering. It enables quantitative discussions, because it can provide a reliable predictions for the excitation energies and the  $\alpha$  decay widths. Up to now, the AMD calculations have been performed for  $^{14}\text{C}$  [23, 236, 237] and for  $^{16}\text{C}$  [25]. Recently, rather promising data that imply the formation of linear-chain states in  $^{14}\text{C}$  [26, 27, 238, 239] and  $^{16}\text{C}$  [240, 241] were reported. They show good agreement with the prediction of AMD studies. Here, we mainly focus on  $^{14}\text{C}$  and introduce the AMD calculation in Ref. [23].

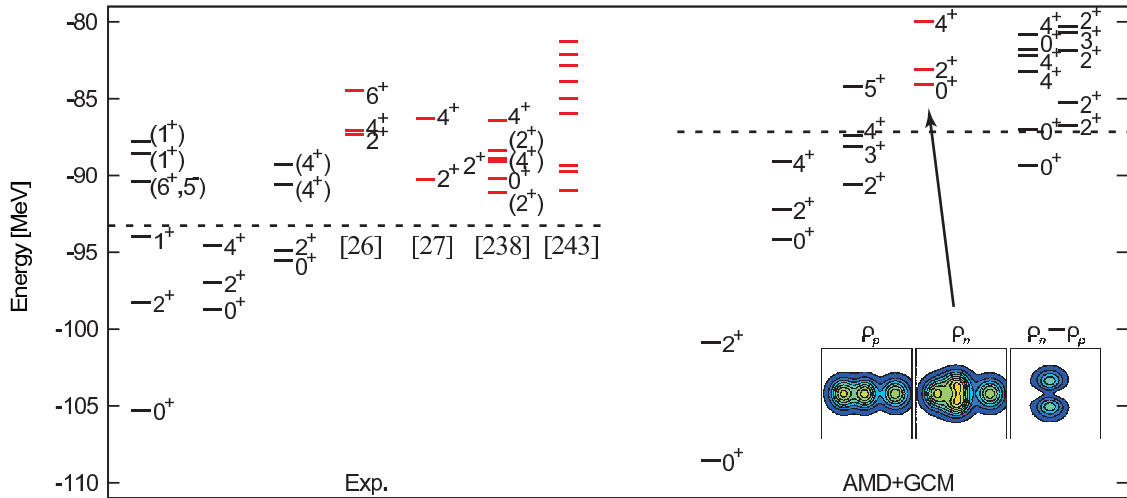


FIG. 34. Energy levels of the positive-parity states in  $^{14}\text{C}$ . The experimental data including the recently observed linear-chain candidates [26, 27, 238, 242] are shown on the left side, while the AMD result is shown on the right side. The observed and calculated linear-chain states (candidates) are shown by the red lines. Dotted lines show the experimental and theoretical  $^{10}\text{Be}+\alpha$  threshold energies, respectively. This figure is reconstructed from the data presented in Ref. [23].

In Ref. [23],  $^{14}\text{C}$  is investigated by using AMD combined with the two-dimensional GCM using quadrupole deformation parameters  $\beta$  and  $\gamma$  as the generator coordinates. In this calculation, we used the Volkov No. 2 interaction combined with the spin-orbit part of the G3RS interaction. The adopted parameters are  $m = 0.6$ ,  $b = h = 0.125$ , and  $u_1 = -u_2 = -1600$  MeV, which reproduce the binding energies of deuteron and  $^{12}\text{C}$ . Fig. 34 compares the observed positive-parity states with the calculation. In the left side of the figure, the black lines show the observed positive-parity states which are known long before [243], while the red lines show the candidates of the linear chain. Three different groups independently reported these candidates based on the  $^{10}\text{Be}+\alpha$  resonant scattering [26, 27, 238]. In the same energy region, another group [242] also reported the candidates based on the  $^{10}\text{Be}+\alpha$  breakup reaction, but the spin-parity assignment was not given. In the right hand side of the figure, we classified the calculated states into five groups by analyzing the intrinsic structures and  $E2$  transition strengths. The left most band shows the ground band and the next two bands are the  $K^\pi = 0^+$  and  $2^+$  bands with triangular configuration of  $3\alpha$  clusters. The calculated linear-chain states are shown by the red lines. We also show the intrinsic proton  $\rho_p$ , neutron densities  $\rho_n$  and their difference  $\rho_n - \rho_p$  for the linear-chain state. From the proton density, we clearly see the linear-chain formation; three  $\alpha$  clusters develop well and they are linearly aligned. It is also noted that the inter-cluster distance between  $3\alpha$  clusters are not equal showing somewhat asymmetric  $2\alpha+\alpha$  correlation. Corresponding to this asymmetry, the excess neutrons distribute around two of the three  $\alpha$  clusters, which have shorter inter-cluster distance. In short, these indicate  $^{10}\text{Be}+\alpha$  correlation in the linear-chain states.

When the excitation energies are measured from the  $\alpha$  threshold, the agreement between the calculated and observed linear-chain candidates looks reasonable. In particular, the spin-parity assignment and the large moment of inertia of  $\hbar^2/2I = 0.19$  MeV reported in Ref. [238] show very good agreement with the AMD. In addition to this, they also reported the large  $\alpha$  decay widths of these linear-chain candidates which are the same order of magnitude to the present result estimated by using the method give in the Ref. [244]. Hence, we conclude that the linear-chain formation in  $^{14}\text{C}$  is rather convincing.

Now, we discuss why the  $^{10}\text{Be}+\alpha$  correlation appears in the linear-chain states by using a generalized molecular orbital model [236]. Fig. 35 shows the calculated energy curves for the intrinsic, positive parity, and  $J^\pi = 0^+$  wave functions of  $^{14}\text{C}$  with the linear-chain

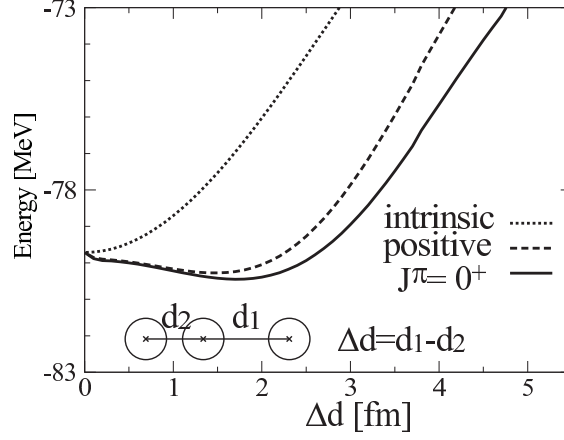


FIG. 35. Energy curves for the intrinsic, positive parity, and  $J^\pi = 0^+$  wave functions of  $^{14}\text{C}$  with the linear-chain configuration. The distance between two  $\alpha$  clusters at both end is fixed to 5.2 fm. The horizontal axis is the difference of the  $\alpha$ -cluster intervals,  $\Delta d$ . The intrinsic and positive parity energy curves are shifted by  $-6.9$  MeV to adjust with the  $J^\pi = 0^+$  energy curve at  $\Delta d = 0$  fm. This figure is reconstructed from the data presented in Ref. [236].

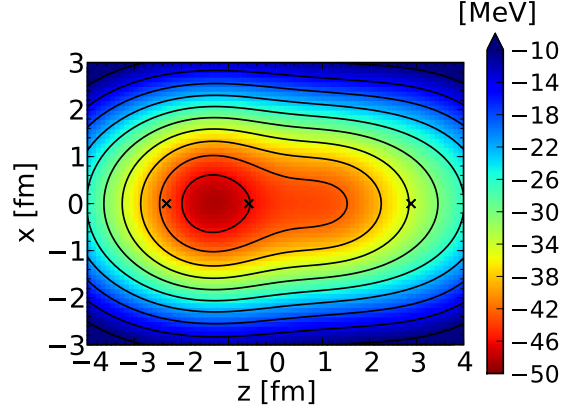


FIG. 36. The contour of the single-folding potential of three  $\alpha$  clusters with the linear-chain structure. The crosses show the positions of three  $\alpha$  clusters. This figure is taken from Ref. [236].

configuration. The intrinsic energy curve has the energy minimum at  $\Delta d = 0$  fm, while the positive-parity and the  $0^+$  energy curves have energy minima at  $\Delta d > 0$  fm. This indicates that the correlation between clusters is described by the parity projection and it induces  $2\alpha + \alpha$  correlation to gain more binding energy.

Then, we consider the motion of the excess neutrons around this asymmetric core. As already mentioned, the excess neutrons concentrate around the correlated  $2\alpha$  clusters. It is

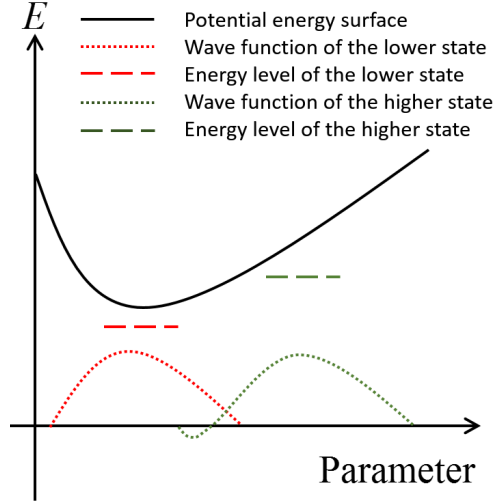


FIG. 37. A schematic figure for the stabilizing mechanism by the orthogonality.

different from a simple molecular orbital picture, where the excess neutrons are distributed widely surrounding all  $\alpha$  clusters to reduce the kinetic energy. This can be understood by a mean-field potential generated by the aligned three  $\alpha$  clusters. Fig. 36 shows a contour of the valence neutron potential which is obtained by the single-folding of three  $\alpha$  clusters with asymmetric linear alignment. The potential is deepest between the correlated  $\alpha$  clusters and becomes shallow around the isolated  $\alpha$  cluster. Therefore, the excess neutrons tend to gather around the correlated two  $\alpha$  clusters to gain potential energy. The detailed balance between the potential energy gain and kinetic energy loss determines the distribution of the excess neutrons. As a result, the  $^{10}\text{Be}+\alpha$  correlation appears in the linear-chain states of  $^{14}\text{C}$ .

Finally, we discuss the reason why the linear-chain states are stabilized in  $^{14}\text{C}$  in contradiction to the result of  $3\alpha+xn$  cluster model by Itagaki *et al.* [22] which reported the instability of the linear-chain in  $^{14}\text{C}$  against the bending motion. From the uncertainty principle, if  $\alpha$  clusters are fixed to the linear alignment, the kinetic energy must be increased. As a result, the bending motion which fluctuates the position of  $\alpha$  clusters and reduces the kinetic energy must be energetically favored. Therefore, for the stability of the linear-chain, an additional stabilizing mechanism is necessary. That is the orthogonality of the wave function to the lower energy states required in quantum mechanics. A schematic figure shown in Fig. 37 explains it. When the Schrödinger equation is solved on the potential surface as shown in the figure, the wave function of the lowest energy state concentrates around the

energy minimum. To satisfy the orthogonal condition to the lower state, the wave function of the excited state cannot have the amplitude near the energy minimum, and therefore, concentrates in the outer regions. In the case of  $^{14}\text{C}$ , the linear-chain states must be orthogonal to the ground band and  $K^\pi = 0^+$  and  $2^+$  bands with triangular configuration of  $3\alpha$  clusters. Note that the bending motion of linear chain makes the overlap between (bent-)linear-chain state and triangular state large that is forbidden by the orthogonality condition. Thus, behind the stability of the linear chain, the orthogonal condition in quantum mechanics plays a crucial role.

A similar mechanism was also discussed in  $^{12}\text{C}$  [245]. The  $0_1^+$  state have a compact triangle structure of three  $\alpha$  clusters with the significant mixing of the  $\alpha$  cluster breaking component. The  $0_2^+$  state is described by the superposition of various triangle configurations of three  $\alpha$  clusters. The compact triangle component in the  $0_2^+$  is hindered due to orthogonality to the  $0_1^+$  state. The details of the structure of the  $0_2^+$  is affected by the magnitude of the mixing of the  $\alpha$  cluster breaking component in the  $0_1^+$  state. The  $0_3^+$  is dominated by the open triangle configuration; therefore this state is considered to be a bent linear-chain states. The compact triangle and acute triangle configurations in the  $0_3^+$  is hindered due to orthogonality to the  $0_1^+$  and  $0_2^+$  states. The structure of the  $0_3^+$  is significantly affected by the magnitude of the mixing of the  $\alpha$  cluster breaking component in the  $0_1^+$  state. As same as  $^{14}\text{C}$ , to the appearance of the linear-chain state, the orthogonal condition plays key role in  $^{12}\text{C}$ . It is very interesting to extend the study to other C isotopes, in particular, to more neutron-rich isotopes. Because the number of excess neutrons is much larger, they can have different stabilization mechanism.

#### **D. Cluster aspects in neutron-rich nuclei**

As discussed in previous sections, a variety of clustering phenomena such as the cluster formation, molecular orbit structures, and di-cluster resonances are seen in neutron-rich nuclei. Be and Ne isotopes are the typical examples that show remarkable clustering phenomena. We here give more general discussions of cluster aspects in neutron-rich nuclei. In the clustering phenomena in nuclear system, many-body correlations as well as single-particle motions play essential roles. For instance, cluster formation originates from strong spatial correlations between nucleons, whereas molecular orbits are characterized by independent

single-particle motion of valence neutrons around a two-center cluster core.

### 1. Molecular orbits v.s. Nilsson orbits

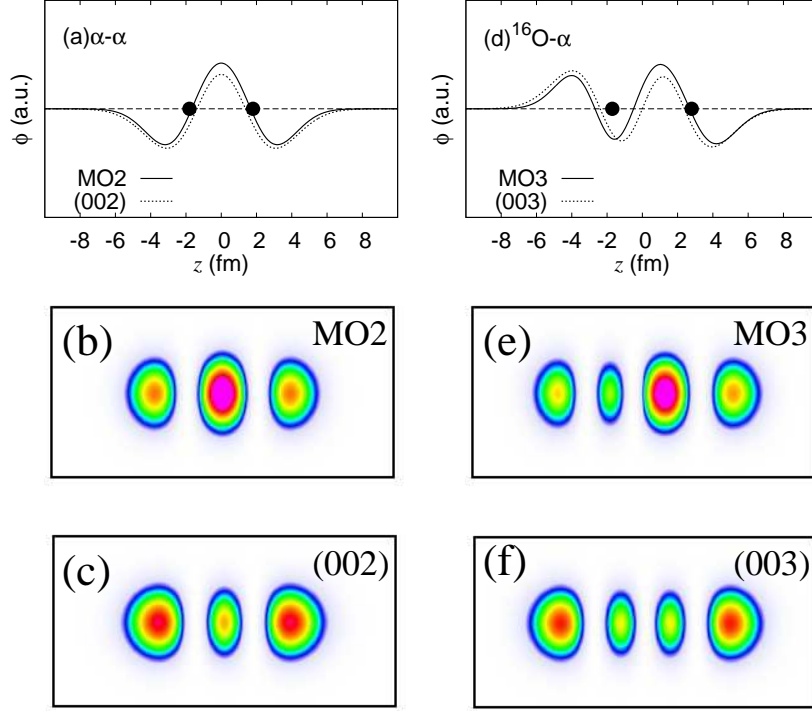


FIG. 38. Molecular  $\sigma$ -orbits and deformed shell-model orbits. (a-c) the  $\sigma$ -orbit (MO2) in the  $\alpha+\alpha$  system compared with the  $(002)_{\text{def}}$  orbit. (d-f) the  $\sigma$ -orbit (MO3) in the  $^{16}\text{O}+\alpha$  system compared with the  $(003)_{\text{def}}$  orbit. Upper panels: the single-particle wave functions on the  $z$  axis at  $x = y = 0$ . Middle and lower panels: the contour map of the density projected on the  $z$ - $y$  plane. The size parameter  $b$  is chosen to be  $b = 1.5$  fm for the  $\sigma$ -orbits,  $b_{\perp} = 1.5$  fm and  $b_z = 1.3b_{\perp}$  for the  $(002)_{\text{def}}$  and  $(003)_{\text{def}}$  orbits. The cluster positions are shown by filled circles.

Molecular orbits are sometimes associated with deformed shell-model (Nilsson) orbits because they are specified by quantum numbers similar to those of deformed shell-model orbits. For instance, the total node number  $N$ , the longitudinal node number  $n_z$ , and the  $z$ -component  $\Omega = j_z$  of the angular momentum are good quantum numbers for molecular orbits as well as deformed shell-model orbits because of the axial symmetry of systems. Indeed, in the case of a small inter-cluster distance, molecular orbits approximately correspond

to deformed shell-model orbits in the normal deformation. However, molecular orbits are not necessarily equivalent to deformed shell-model orbits except for the small inter-cluster distance case. For example, the  $\sigma$ -orbits around the  $2\alpha$  and  $^{16}\text{O}+\alpha$  cores have the quantum numbers same as those of  $(n_x n_y n_z) = (002)_{\text{def}}$  and  $(003)_{\text{def}}$  orbits in the deformed harmonic oscillator (h.o.) potential, however, they are quantitatively different from the deformed shell-model orbits. The  $\sigma$ -orbits typically have largest amplitudes in between clusters, whereas the  $(002)_{\text{def}}$  and  $(003)_{\text{def}}$  orbits have maximum amplitudes at the surface region and relatively smaller amplitudes in the inner region. In Fig. 38, we give a comparison between the  $\sigma$ -orbits and deformed shell-model orbits. Here the molecular  $\sigma$ -orbit (MO2) around the  $2\alpha$  is simply assumed to be a linear combination of the spherical h.o. orbit  $(001)$  around the left and right  $\alpha$  clusters ( $\alpha_1$  and  $\alpha_2$ ) as

$$\phi_{\text{MO2}} = n_0 \hat{P}_{\text{orth}} \{ (001)_{\alpha_1} - (001)_{\alpha_2} \}, \quad (25)$$

where  $n_0$  is the normalization factor and  $\hat{P}_{\text{orth}}$  is the projection operator for the orthogonal condition to the occupied orbits  $(000)_{\alpha_1}$  and  $(000)_{\alpha_2}$ . In a similar way, we also assume the molecular  $\sigma$ -orbit (MO3) around the  $^{16}\text{O}+\alpha$  with  $(002)_{^{16}\text{O}}$  and  $(001)_{\alpha}$  as

$$\phi_{\text{MO3}} = n_0 \hat{P}_{\text{orth}} \{ (002)_{^{16}\text{O}} - (001)_{\alpha} \}, \quad (26)$$

where the  $\hat{P}_{\text{orth}}$  is defined so as to satisfy the orthogonal condition to the occupied orbits  $(000)_{^{16}\text{O}}$ ,  $(001)_{^{16}\text{O}}$  and  $(000)_{\alpha}$ . (General molecular orbits in realistic systems are given by linear combination of any atomic orbits with coefficients optimized for each system, but here we simply consider a specific case of orbits and coefficients.) As shown in Fig. 38, amplitudes of the  $\sigma$ -orbits are enhanced in between two clusters differently from the  $(002)_{\text{def}}$  and  $(003)_{\text{def}}$  orbits, in which the inner amplitudes are remarkably suppressed. It means that, the probability of valence neutrons in the  $\sigma$  orbits is enhanced in the region between two clusters, because, neutrons feel attractive potentials from both clusters and less Pauli repulsion from core nucleons in this low-density region. As a result of the enhanced amplitude in between clusters,  $\sigma$ -orbit neutrons push outward the clusters bonding them at a moderate distance to form the MO  $\sigma$ -bond structure like a covalent bond in a molecule. This is one of the important differences of the molecular orbits in the two-center potential from the deformed shell-model orbits in the one-center potential.

## 2. *Molecular orbits v.s. atomic orbits (strong coupling v.s. weak coupling clustering)*

In the coexistence of the molecular orbit structures and di-cluster resonances in neutron-rich Be and Ne isotopes, valence neutrons play important roles. Valence neutrons in the molecular orbits move around whole the system connecting two cluster cores, whereas those in the di-cluster resonances are localized to one side (around one of the two cluster cores). The former is analogous to covalent orbits and the latter is associated with atomic orbits in ionic bonding. In a system consisting of two cluster cores and valence neutrons, appearance of the molecular orbit structures is not obvious. The first condition for the molecular orbit structure is formation of single-particle orbits surrounding both the clusters. The second condition is that the independent particle feature of valence neutrons dominates over many-body correlations which gathers neutrons to one of two clusters.

In the case of identical two clusters such as  $\alpha+\alpha$ , single-particle orbits are reflection symmetric because of the symmetry of the mean potential from two clusters. As a result, at a moderate inter-cluster distance, molecular orbits are favored to gain the kinetic energy provided that many-body correlations between valence neutrons are minor. However, in the asymptotic region of a large inter-cluster distance, valence neutrons localize to one side to gain the correlation energy, and the molecular orbits change to the atomic orbits. In such the case, the system separates into two clusters to form a di-nuclear structure, in which inter-cluster motion is decoupled from internal degrees of freedom of clusters, and then, di-cluster resonances arise from excitation of the inter-cluster motion. By means of the GTCM, Ito *et al.* solved valence neutron wave functions in  $2\alpha+2n$  with a fixed inter-cluster distance and demonstrated smooth transition of valence neutron orbits from the molecular(covalent) orbits at a moderate distance to atomic orbits at a large distance [57, 61, 66].

It is also important that different types of low-energy excitation modes appear in the molecular orbit and di-cluster structures. The low-energy modes in the molecular orbit structure are based on single-particle excitations in the molecular orbit configurations, whereas those in the di-nuclear structure originate from the inter-cluster excitation as well as internal excitations of clusters. In Be isotopes, the molecular orbits are favored at a moderate inter-cluster distance. As discussed previously, the low-energy excitations are described by single-particle excitations in the molecular orbit configurations, whereas the di-cluster resonances in the relatively higher energy region arise from the inter-cluster excitations. For



instance, in  $^{10}\text{Be}$ , the  $K^\pi = 0_2^+$  and  $K^\pi = 1^-$  bands are understood by the single-particle excitations in the molecular orbit configurations, whereas the  ${}^6\text{He}(2^+)+\alpha$  and  ${}^6\text{He}(0^+)+\alpha$  cluster resonances are expected in highly excited  $0^+$  states from the inter-cluster excitations with and without the internal excitation of the  ${}^6\text{He}$  cluster. The existence of two excitation modes are more clearly seen in the calculated negative-parity spectra of  $^{12}\text{Be}$ . The  $K^\pi = 1^-$  band arises from the single-particle excitation in the molecular orbit configurations, whereas the  $K^\pi = 0^-$  band appears from the negative-parity inter-cluster excitation between  ${}^8\text{He}$  and  $\alpha$  clusters.

It should be noted that, with the increase of valence neutrons, the effect of many-body correlations becomes no longer minor even at the moderate distance, and it increases asymmetry of the total system. In other words, the reflection symmetry is spontaneously broken by many-body correlations between valence neutrons as seen in the asymmetric intrinsic densities of Be isotopes as already shown in Fig. 19. Because of the asymmetry, the single-particle orbits somewhat deviate from ideal molecular orbits. It means mixing of di-cluster components, even though the low-lying states of Be isotopes can be qualitatively understood by dominant molecular orbit components.

Let us next consider the case that two cluster cores are not identical. In such the case of asymmetric two clusters with valence neutrons, reflection symmetry of the mean potential is explicitly broken, and hence, the formation of molecular orbits is not obvious. As an example, we consider  ${}^9\text{Li}$  as an  $\alpha + t$  core with two valence neutrons in analogy to  $^{10}\text{Be}$  having the  $2\alpha$  core with two valence neutrons. In the  $\alpha+t$  system at a moderate inter-cluster distance, valence neutrons feel stronger attraction from the  $\alpha$  cluster than that from the  $t$  cluster and tend to be localized around the  $\alpha$  cluster to form a  ${}^6\text{He}$  cluster. Moreover, the  $t$  cluster feels a weak attraction from the  ${}^6\text{He}$  cluster and therefore the system favors a di-cluster structure of  ${}^6\text{He}+t$ . It meant that the MO  $\sigma$ -bond structure is not favored in  ${}^9\text{Li}$ . Indeed, in the theoretical calculation of  ${}^9\text{Li}$  in Ref. [169],  ${}^6\text{He}+t$  cluster resonances are obtained but the MO  $\sigma$ -bond structure is not obtained in excited states of  ${}^9\text{Li}$ .

Neutron-rich B is another example, in which the molecular orbit picture is useful to understand the cluster structures as discussed in Refs. [174, 185]. In order to understand the formation of molecular orbits in  $^{13}\text{B}$ , it is better to consider the  $2\alpha$  core surrounded by valence nucleons (a proton and 4 neutrons) in the molecular orbits rather than a  $\text{Li}+\alpha$  core. Then, we can understand the appearance of the molecular orbits around the  $2\alpha$  core in  $^{13}\text{B}$

similarly to Be isotopes.

Now, a question is why molecular orbit structures appear in such *sd*-shell nuclei as F and Ne isotopes, which have further asymmetric two clusters. In the case of Ne isotopes, the  $\sigma$ -orbit is constructed by *sd* orbits around the  $^{16}\text{O}$  cluster and a *p* orbit around the  $\alpha$  cluster [11]. Even though the potential from the  $^{16}\text{O}$  cluster is stronger than that from the  $\alpha$  cluster, the lowest allowed orbits are *sd* orbits because of Pauli blocking from core nucleons. Consequently, valence neutrons in the higher-shell (*sd*) orbits feel effectively weak attraction and can contribute to form the molecular  $\sigma$ -orbit together with the *p* orbit around the  $\alpha$  cluster. The question to be answered is whether or not the formation of molecular orbits in the asymmetric cluster system is caused by accidental matching of the single-particle orbits around different clusters, probably, relating to matching condition of single-particle energies. The origin of molecular orbits is also discussed by von Oertzen from the view point of threshold energies [11, 14, 17]. To answer this question, further examples of molecular-orbit structures in various nuclei are required.

### 3. *Di-cluster resonances*

Di-cluster resonances have been well known in stable nuclei such as  $^{16}\text{O}+\alpha$  cluster states in  $^{20}\text{Ne}$  and  $^{12}\text{C}+\alpha$  cluster states in  $^{16}\text{O}$  (see Ref. [3] and references therein). In unstable nuclei, di-cluster resonances have been discovered by recent experimental and theoretical studies, as discussed previously for He+He cluster resonances in neutron-rich Be isotopes. Also in other unstable nuclei, di-cluster resonances containing an  $\alpha$  cluster are expected to appear near  $\alpha$ -decay threshold energies. Examples are  $^{10}\text{Be}+\alpha$  states in  $^{14}\text{C}$  [23, 26, 27, 242, 246–249],  $^9\text{Li}+\alpha$  states in  $^{13}\text{B}$  [174],  $^{14}\text{C}+\alpha$  states in  $^{18}\text{O}$  and their mirror states [196, 204–207, 210–212, 250, 251],  $^{18}\text{O}+\alpha$  states in  $^{22}\text{Ne}$  [194–198, 201, 210, 211]. These facts may imply that di-cluster resonances arising from  $\alpha$ -cluster excitations can be general phenomena in stable and unstable nuclei.

Experimental and theoretical efforts of searching for di-cluster resonances are being made. It is also an challenging problem to discover more exotic di-cluster resonances comprised by two exotic nuclei such as *t*,  $^6\text{He}$ ,  $^9\text{Li}$ ,  $^{10}\text{Be}$ ,  $^{13}\text{B}$ ,  $^{14}\text{C}$ , and  $^{18,20}\text{O}$  clusters. Examples are  $^8\text{He}+^6\text{He}$  in  $^{14}\text{Be}$  [54, 252] and  $^6\text{He}+t$  states in  $^9\text{Li}$  [169]. It is an important task to explore new cluster states near cluster-decay thresholds in excited states of various nuclei.

In systematics of di-cluster resonances in various unstable nuclei, we will obtain an answer to the question, whether Ikeda threshold rule can be extended to a wide region of the nuclear chart including unstable nuclei.

## V. MONOPOLE AND DIPOLE TRANSITIONS AS THE PROBE FOR CLUSTERING

In this section, we focus on the signature of the clustering. Experimentally, several observables have been utilized as the evidence of clustering. One of the important observable is the  $\alpha$  decay width from which the  $\alpha$  reduced amplitude or the preformation factor of  $\alpha$  particle at the nuclear surface can be extracted. The reduced width amplitudes including those for the non-alpha clustering can be also measured by the resonant scattering, cluster transfer and knock-out reactions. We have discussed that the behavior of the proton radii also indicates the clustering albeit indirectly. However, in general, the measurement of these quantities is not easy for unstable nuclei, although the rapid development of the experimental technique is enabling it. Therefore another observable will be very helpful for the discussion of the clustering in unstable nuclei.

In this decade, the monopole transition was found to be very sensitive probe for the clustering [253] and has been utilized to search for the cluster states in light stable nuclei such as  $^{11}\text{B}$  [254],  $^{12}\text{C}$  [255–257],  $^{16}\text{O}$  [258],  $^{24}\text{Mg}$  [259] and  $^{32}\text{S}$  [260]. Recently the discussion of the monopole transition and clustering was extended to the neutron-rich Be isotopes [84, 261]. In addition to the monopole transition, dipole transition is also expected as a promising and unique tool for the study of clustering [262–265]. Therefore, we briefly summarize the recent discussions on the monopole and dipole transitions. We first discuss the relationship between the clustering and these transitions in  $N \simeq Z$  nuclei and introduce several AMD calculations. Then, we discuss the monopole and dipole responses of neutron-rich nuclei.

### A. Clustering in stable nuclei and isoscalar monopole and dipole transitions

It has long been known that many cluster states in light stable nuclei have large monopole transition strengths from the ground state [42, 228, 229, 266–272]. Therefore, isoscalar (IS) monopole transition has been utilized as a probe to search for the cluster states. Later,

Yamada *et al.* [253] gave a clear explanation of the enhancement mechanism of the monopole transition. Recently, the enhancement of the IS dipole transition for the cluster states was also pointed out [263]. Here, we briefly outline these enhancement mechanism and introduce several AMD results for  $N \simeq Z$  nuclei.

### 1. Estimate of the transition strengths

It is well known that at the zero limit of the inter-cluster distance, the cluster model wave function and  $SU(3)$  shell model wave function [273, 274] become mathematically identical [275, 276]. This fact known as the Bayman-Bohr theorem plays a central role for the discussion of the IS monopole and dipole transitions and their relationship to the clustering. For example, the ground state of  $^{20}\text{Ne}$  is described well by a  $SU(3)$  shell model wave function. The Bayman-Bohr theorem guarantees that it can be equivalently rewritten in terms of the cluster model wave function,

$$\begin{aligned}\Phi(0_1^+) &= \mathcal{A} \{ (0s)^4(0p)^8(1s0d)^4 \}_{(8,0)} \\ &= n_{N_0} \mathcal{A} \{ R_{N_0 0}(r) Y_{00}(\hat{r}) \phi_\alpha \phi_O \},\end{aligned}\tag{27}$$

where the first and second lines are the shell model and cluster model representations, respectively. In the cluster model representation,  $\phi_\alpha$  and  $\phi_O$  denote the internal wave functions of clusters, and their relative motion is described by a Harmonic oscillator wave function  $R_{N_0 0}(r) Y_{00}(\hat{r})$  with the principal quantum number  $N_0 = 8$ . This equivalence implies that the degrees-of-freedom of cluster excitation is embedded even in an ideal shell model state; *i.e.* the excitation of the inter-cluster motion populates the cluster states from a shell model state. For example, if we increase the nodal quantum number, we get an excited  $0^+$  cluster state,

$$\Phi(0_{ex}^+) = \sum_{N=N_0+2}^{\infty} f_N n_N \mathcal{A} \{ R_{N 0}(r) Y_{00}(\hat{r}) \phi_\alpha \phi_O \},\tag{28}$$

which is a superposition of the wave functions with increased principal quantum number  $N$ . Another option is the increase of the orbital angular momentum. With increase by one, we obtain an excited  $1^-$  cluster state,

$$\Phi(1_{ex}^-) = \sum_{N=N_0+1}^{\infty} g_N n_N \mathcal{A} \{ R_{N 0}(r) Y_{10}(\hat{r}) \phi_\alpha \phi_O \}.\tag{29}$$

We call these excited cluster states “nodal excited” and “angular excited” states (Fig. 39). In the case of  $^{20}\text{Ne}$ , the  $0_4^+$  state at 8.7 MeV is the nodal excited state, while the  $1_1^-$  state at 5.8 MeV is the angular excited state [191]. As already explained in the section IV B, this  $1_1^-$  state has importance as the evidence for the parity asymmetric structure of  $\alpha+^{16}\text{O}$  [139].

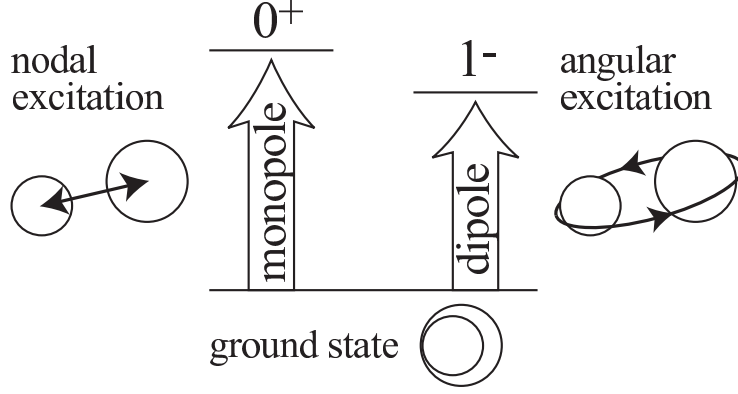


FIG. 39. Schematic figure for the nodal and angular excitations. IS monopole and dipole transitions strongly populates these cluster states.

By rewriting the IS monopole and dipole operators in terms of the cluster coordinates, it can be shown that the IS monopole and dipole transitions strongly induce the nodal and angular excitations. The IS monopole operator is rewritten as [253],

$$\begin{aligned}\mathcal{M}^{IS0} &= \sum_{i=1}^A (\mathbf{r}_i - \mathbf{r}_{\text{cm}})^2 \\ &= \sum_{i \in C_1} \xi_i^2 + \sum_{i \in C_2} \xi_i^2 + \frac{C_1 C_2}{A} r^2,\end{aligned}\tag{30}$$

where the first line shows the standard definition of the operator in terms of the single-particle coordinate  $\mathbf{r}_i$ , while the second line is the representation by the cluster coordinates which are defined as,

$$\xi_i = \begin{cases} \mathbf{r}_i - \mathbf{r}_{C_1}, & i \in C_1 \\ \mathbf{r}_i - \mathbf{r}_{C_2}, & i \in C_2, \end{cases} \quad \mathbf{r} = \mathbf{r}_{C_1} - \mathbf{r}_{C_2},\tag{31}$$

$$\mathbf{r}_{C_1} = \frac{1}{C_1} \sum_{i \in C_1} \mathbf{r}_i, \quad \mathbf{r}_{C_2} = \frac{1}{C_2} \sum_{i \in C_2} \mathbf{r}_i.\tag{32}$$

Here, we have assumed that the system is composed of the two clusters with masses  $C_1$  and  $C_2$  as shown in Fig. 40. Note that this expression makes it clear that  $\mathcal{M}^{IS0}$  will populate

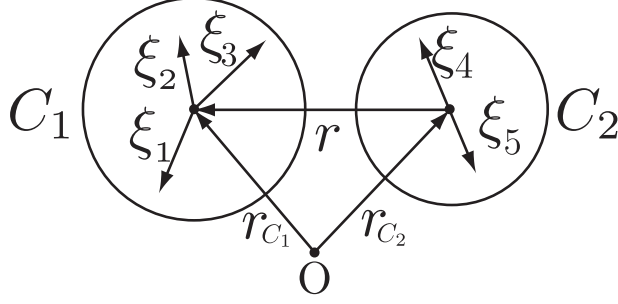


FIG. 40. Definition of the cluster coordinates.  $\xi_i$  denote the internal coordinates of clusters, while  $\mathbf{r}$  is the inter-cluster coordinate.

nodal excited states, because the last term proportional to  $r^2$  will induce the nodal excitation of the inter-cluster motion.

By a similar calculation, one finds that the IS dipole operator is rewritten as follows [263],

$$\begin{aligned}
\mathcal{M}_\mu^{IS1} &= \sum_{i=1}^A (\mathbf{r}_i - \mathbf{r}_{\text{c.m.}})^2 \mathcal{Y}_{1\mu}(\mathbf{r}_i - \mathbf{r}_{\text{c.m.}}) \\
&= \sum_{i \in C_1} \xi_i^2 \mathcal{Y}_{1\mu}(\xi_i) + \sum_{i \in C_2} \xi_i^2 \mathcal{Y}_{1\mu}(\xi_i) \\
&\quad - \frac{\sqrt{32\pi}}{3} \left[ \left( \frac{C_2}{A} \sum_{i \in C_1} \mathcal{Y}_2(\xi_i) - \frac{C_1}{A} \sum_{i \in C_2} \mathcal{Y}_2(\xi_i) \right) \mathcal{Y}_1(\mathbf{r}) \right]_{1\mu} \\
&\quad + \frac{5}{3} \left( \frac{C_2}{A} \sum_{i \in C_1} \xi_i^2 - \frac{C_1}{A} \sum_{i \in C_2} \xi_i^2 \right) \mathcal{Y}_{1\mu}(\mathbf{r}) \\
&\quad + \frac{C_1 C_2 (C_1 - C_2)}{A^2} r^2 \mathcal{Y}_{1\mu}(\mathbf{r}). \tag{33}
\end{aligned}$$

From this expression we see that the terms depending on  $\mathcal{Y}_{1\mu}(\mathbf{r})$  and  $r^2 \mathcal{Y}_{1\mu}(\mathbf{r})$  will induce the angular excitation to populate angular excited cluster states.

It is possible to derive analytic formulae for IS monopole and dipole transition matrices by using the wave functions Eqs. (27)-(30) and (33) [253, 263]. In the case of  $^{20}\text{Ne}$ , they

read

$$\begin{aligned}
M^{IS0} &= \langle \Phi(0_{ex}^+) | \mathcal{M}^{IS0} | \Phi(0_{gs}^+) \rangle \\
&= f_{N_0+2} \sqrt{\frac{\mu_{N_0}}{\mu_{N_0+2}}} \langle R_{N_0 0} | r^2 | R_{N_0+2 0} \rangle,
\end{aligned} \tag{34}$$

$$\begin{aligned}
M^{IS1} &= \sqrt{3} \langle \Phi(1_{ex}^-) | \mathcal{M}^{IS1} | \Phi(0_{gs}^+) \rangle \\
&= \sqrt{\frac{3}{4\pi}} \left[ g_{N_0+1} \sqrt{\frac{\mu_{N_0}}{\mu_{N_0+1}}} \left\{ \frac{48}{25} \langle R_{N_0 0} | r^3 | R_{N_0+1 1} \rangle \right. \right. \\
&\quad \left. \left. + \frac{16}{3} (\langle r^2 \rangle_\alpha - \langle r^2 \rangle_O) \langle R_{N_0 0} | r | R_{N_0+1 1} \rangle \right\} \right. \\
&\quad \left. + \frac{3}{5} g_{N_0+3} \sqrt{\frac{\mu_{N_0}}{\mu_{N_0+3}}} \langle R_{N_0 0} | r^3 | R_{N_0+3 1} \rangle \right],
\end{aligned} \tag{35}$$

where  $\langle r^2 \rangle_\alpha$  and  $\langle r^2 \rangle_O$  are the mean-square radii of the clusters.  $\mu_N$  is defined as,

$$\mu_N = \langle R_{Nl}(r) Y_{lm}(\hat{r}) \phi_\alpha \phi_O | \mathcal{A} \{ R_{Nl}(r) Y_{lm}(\hat{r}) \phi_\alpha \phi_O \} \rangle. \tag{36}$$

By using the amplitudes  $f_N$  and  $g_N$  calculated by AMD, the formulae can be easily estimated as

$$M^{IS0} = 7.67 f_{N_0+2} = 5.48 \text{ fm}^2, \tag{37}$$

$$M^{IS1} = 3.08 g_{N_0+1} - 7.36 g_{N_0+3} = 5.82 \text{ fm}^3, \tag{38}$$

which are as large as the Weisskopf estimates,

$$M_{\text{WU}}^{IS0} = \frac{3}{5} (1.2 A^{1/3})^2 \simeq 0.864 A^{2/3} \simeq 6.37 \text{ fm}^2, \tag{39}$$

$$M_{\text{WU}}^{IS1} = \sqrt{\frac{3}{4\pi}} \frac{3}{6} (1.2 A^{1/3})^3 \simeq 0.422 A \simeq 8.44 \text{ fm}^3. \tag{40}$$

Thus, the IS monopole and dipole transition strengths from the ground state to the excited cluster states are as strong as the Weisskopf estimates, even though the ground state is an ideal shell model state. It is well known that the giant resonances have very strong transition strengths and exhaust most of the sum rule. But, they cannot appear at small excitation energy because they involve the change of the matter density as illustrated in Fig. 1 (a). On the other hand, the cluster excitations illustrated in Fig. 1 (c) occur at relatively small energies, because their excitation energies are governed by Ikeda threshold rule (Fig. 2). This naturally explains why there exist many narrow resonances in the response functions of light nuclei in the IS monopole and dipole channels [255, 259, 260, 277–282]. Hence, the low-lying IS monopole and dipole strengths can be regarded as good signature of clustering.

## 2. AMD results for light stable nuclei

The discussion above neglects the cluster correlation in the ground state and the distortion of the clusters in the excited states, which will affect the transition strengths. To obtain accurate results by taking these effects into account, AMD calculations were performed for several nuclei [41, 262, 263]. As an example, Fig. 41 shows the observed and calculated  $\alpha + {}^{16}\text{O}$  cluster bands in  ${}^{20}\text{Ne}$ . Compared to the Brink-Bloch GCM which assumes the

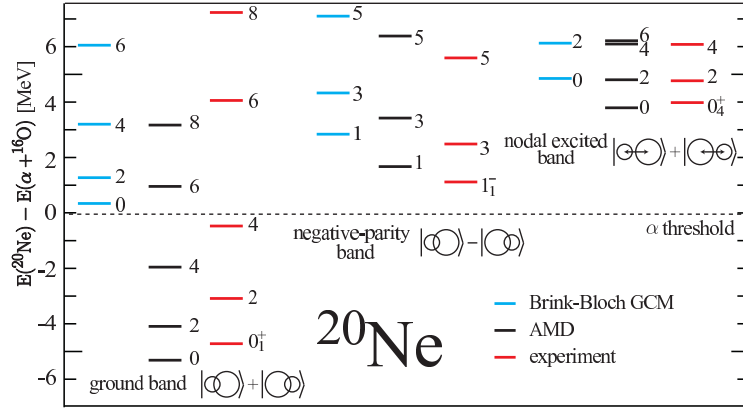


FIG. 41. Observed and calculated  $\alpha + {}^{16}\text{O}$  cluster bands in  ${}^{20}\text{Ne}$ . The Brink-Bloch GCM calculation assumes the  $\alpha + {}^{16}\text{O}$  cluster structure. This figure is reconstructed from the data presented in Ref. [263].

$\alpha + {}^{16}\text{O}$  cluster structure, AMD reasonably describes the ground band, which means that the distortion of clusters is important for the ground band. On the other hand, both models reasonably describe the excited cluster bands including the nodal and angular excited states. This indicates that these excited cluster bands have almost ideal  $\alpha + {}^{16}\text{O}$  cluster structure. It is also confirmed from the large distance between  $\alpha$  and  ${}^{16}\text{O}$  clusters listed in Tab. III which are estimated in the same way as explained in the section III B. The calculated transition matrices are also given in Tab. III. One sees that both of the IS monopole and dipole transitions are very strong and much more enhanced than the Weisskopf estimates and the cluster estimates given in Eqs. (37) and (38). This enhancement owes to the  $\alpha + {}^{16}\text{O}$  clustering in the ground state as we see from the large inter-cluster distance ( $R(0_1^+) = 4.0$  fm) in the ground state. As a result, the transition matrices are further amplified.

We also comment on the transitions in  ${}^{22}\text{Ne}$ . As already discussed in the section IV B, the valence neutrons yield two different kinds of cluster states; the molecular-orbit states



TABLE III. The estimated distances  $d$  between  $\alpha$  and  $^{16}\text{O}$  clusters in the ground state, nodal and angular excited states of  $^{20}\text{Ne}$  in unit of fm. The IS monopole and dipole transition matrices from the ground state to the nodal and angular excited states are given in units of  $\text{fm}^2$  and  $\text{fm}^3$ , respectively. Numbers in parenthesis are ratio to the Weisskopf estimates. The data is taken from Ref. [263].

$^{20}\text{Ne}$	$d(0_1^+)$	$d(0_4^+)$	$d(1_1^-)$	$M^{IS0}$	$M^{IS1}$
BB GCM	5.0	6.5	5.5	46 (7.3)	90 (11)
AMD	4.0	6.0	5.0	16 (2.5)	38 (4.5)

TABLE IV. The estimated distances between  $\alpha$  and  $^{18}\text{O}$  clusters in the ground state, molecular-orbit and atomic-orbit states of  $^{22}\text{Ne}$  in unit of fm. The IS monopole and dipole transition matrices from these cluster states are given in units of  $\text{fm}^2$  and  $\text{fm}^3$ , respectively. These results are obtained by AMD. Numbers in parenthesis are ratio to the Weisskopf estimates.

$^{22}\text{Ne}$	$0_1^+$	$0_2^+$	$1_1^-$	$1_2^-$	$0_3^+$	$1_3^-$
$d$	3.25	3.75	5.0	5.5	6.5	6.75
$M^{IS0/IS1}$		1.7	5.8	1.9	24	22
		(0.26)	(0.62)	(0.2)	(3.5)	(2.4)

( $0_2^+$ ,  $1_1^-$  and  $1_2^-$ ) and the atomic-orbit states ( $0_3^+$  and  $1_3^-$ ). Table IV summarizes the inter-cluster distances and transition strengths of these cluster states. The atomic-orbit states have large transition strengths from the ground state, because they are regarded as an ordinary di-cluster states composed of  $\alpha$  and  $^{18}\text{O}$  clusters, and hence, the discussion made in the previous section can be applied. On the other hand, the molecular-orbits states have hindered transition strengths in spite of their pronounced clustering. This difference is explained as follows. The transitions from the ground state to the molecular-orbit states involve the rearrangement of two valence neutron configuration in addition to the cluster excitation of the core. However, the IS monopole and dipole operators cannot excite the cluster core and valence neutrons simultaneously. As a result, the transitions to the  $\sigma$ -bond cluster states (the cluster states with the rearrangement of valence neutrons) are hindered. In other words, the IS monopole and dipole transitions are sensitive to the excitation of

the inter-cluster motion, but insensitive to the valence neutron excitation. These property has been utilized for the search of the atomic-orbit states in Be isotopes [84, 261], and also discussed in the next section.

### 3. *sAMD results for light stable nuclei*

In IS monopole strengths in  $^{16}\text{O}$ , significant percentages of the energy-weighted sum rule (EWSR) has been found in a low-energy region. Yamada *et al.* pointed out that two different types of IS monopole excitations exist in  $^{16}\text{O}$  [271]: the low-energy IS monopole strengths of excitations into cluster states in  $E \lesssim 16$  MeV are separated from high-energy IS monopole strengths for the IS giant monopole resonance (ISGMR) in  $E > 16$  MeV, which corresponds to the collective vibration mode described by coherent one-particle and one-hole (1p-1h) excitations in a mean field. The separation of the low-energy IS monopole strengths from the ISGMR was also found in  $^{12}\text{C}$  [283, 284]. In order to theoretically describe these two kinds of monopole modes, the cluster excitation and collective breathing mode (coherent 1p-1h excitations), an extended version of antisymmetrized molecular dynamics called “shifted basis AMD (sAMD)” combined with the cluster GCM has been constructed and applied to IS monopole and dipole excitations in light nuclei [264, 285].

Figure 42 shows IS monopole and dipole strengths for  $^{12}\text{C}$  calculated using the sAMD with the  $3\alpha$  GCM, and IS monopole strengths for  $^{16}\text{O}$  calculated using the sAMD with the  $^{12}\text{C}+\alpha$  GCM. The MV1 ( $m = 0.62$ ,  $b = h = 0$ ) central and G3RS ( $u_1 = -u_2 = -3000$  MeV) spin-orbit interactions are used. Experimental data measured by  $(\alpha, \alpha')$ [279, 284] and  $(e, e')$ [269] scatterings are also shown in the figure.

In the calculated IS monopole strengths of  $^{12}\text{C}$ , we found two kinds of excitations: low-energy strengths around  $E_x = 10$  MeV for cluster excitations and high-energy strengths of the ISGMR for the collective breathing mode. The experimentally observed IS monopole strengths of  $^{12}\text{C}$  show that the low-energy IS monopole strengths in  $E \lesssim 12$  MeV exhaust significant percentages of the EWSR comparable to the high-energy strengths in  $E > 12$  MeV of the ISGMR. The calculation describes this separation of the low-energy cluster modes and the high-energy ISGMR. Although the quantitative reproduction of the ISGMR energy and width is not satisfactory, the ratio of the IS monopole strengths of the low-energy to high-energy parts is reproduced well in the present calculation. Also in the IS

dipole strengths of  $^{12}\text{C}$ , we obtain low-energy strengths in  $E_x = 10 - 15$  MeV which are contributed by  $1^-$  states of cluster excitations. These strengths may correspond to the significant IS dipole strengths experimentally measured in  $E_x = 10 - 20$  MeV region.

In the calculated IS monopole strengths of  $^{16}\text{O}$ , three peaks for cluster states are obtained in the low-energy part ( $E_x < 16$  MeV). This is consistent with the  $4\alpha$  orthogonality condition model calculation by Yamada *et al.* [271]. In the high-energy part, significant strengths exist in  $E_x = 20 - 25$  MeV region corresponding to the ISGMR for the collective breathing mode.

## B. Monopole and dipole transitions in neutron-rich nuclei

### 1. Isovector dipole excitations in Be isotopes

Low-energy isovector (IV) dipole excitation is one of the current issues concerning exotic excitation modes in neutron-rich nuclei. In neutron-rich nuclei, low-energy IV dipole resonances (LEIVDRs) are expected to arise from excess neutron motion against a core nucleus. On the other hand, IV giant dipole resonances (IVGDRs), which have been systematically observed in stable nuclei, are understood as a collective mode of the opposite motion between protons and neutrons. In prolately deformed stable nuclei, a two peak structure of the IVGDRs has been observed because of longitudinal and transverse oscillations. In deformed neutron-rich nuclei such as Be isotopes, a variety of dipole excitation modes may exist because of excess neutron motions on the top of the deformed ground states. Questions to be answered are whether LEIVDRs appear and how the IVGDR is affected in the presence of excess neutrons.

The IV and IS dipole excitations in  $^9\text{Be}$  and  $^{10}\text{Be}$  have been investigated using the sAMD+GCM [265]. IV dipole excitations for  $^8\text{Be}(0_1^+) \rightarrow ^8\text{Be}(1^-)$ ,  $^9\text{Be}(3/2_1^-) \rightarrow ^9\text{Be}(1/2^+, 3/2^+, 5/2^+)$ , and  $^{10}\text{Be}(0_1^+) \rightarrow ^{10}\text{Be}(1^-)$  calculated by the sAMD using the MV1 ( $m = 0.62$ ,  $b = h = 0$ ) central and G3RS ( $u_1 = -u_2 = -3000$  MeV) spin-orbit interactions are shown in Fig. 43(a)-(c). In Fig. 43 (d), the calculated  $E1$  cross sections of  $^9\text{Be}$  are compared with the experimental photonuclear cross sections.

The IVGDR in  $^8\text{Be}$  splits into two peaks as expected from the  $2\alpha$  cluster structure with a prolate deformation. The lower peak of the IVGDR at  $E = 20 - 25$  MeV is contributed by the longitudinal mode, whereas the higher peak of the IVGDR around  $E = 30$  MeV

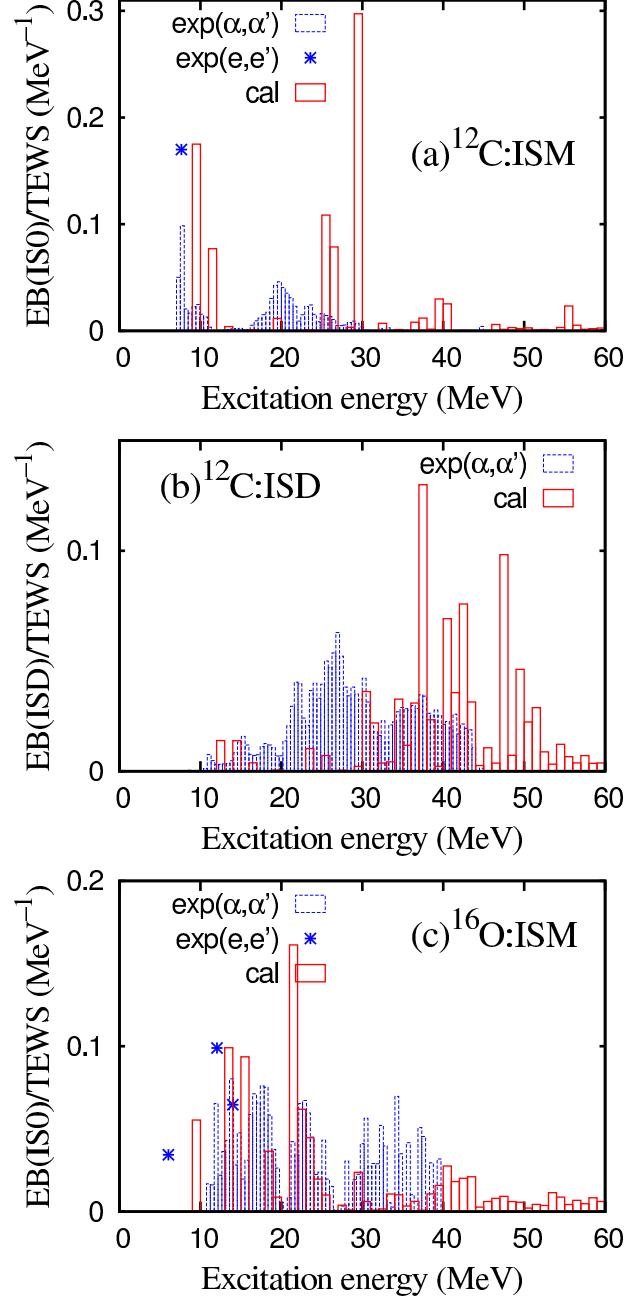


FIG. 42. Energy-weighted strengths of IS monopole and dipole transitions of  $^{12}\text{C}$  and  $^{16}\text{O}$  calculated using the sAMD combined with the cluster GCM, and those measured by  $(\alpha, \alpha')$ [279, 284] and  $(e, e')$ [269] scatterings. Figures are taken from Refs. [264, 285].

comes from the transverse mode of the  $2\alpha$  cluster. In  ${}^9\text{Be}$  and  ${}^{10}\text{Be}$ , the  $E1$  strengths for the IVGDR are obtained in the  $E > 20$  MeV region. The IVGDRs in  ${}^9\text{Be}$  and  ${}^{10}\text{Be}$  are contributed by the IV dipole strengths in the  $2\alpha$  core, and they show the two peak structure because of the prolately deformed core. However, the higher peak for the transverse mode is significantly affected by excess neutrons. The higher peak somewhat broadens in  ${}^9\text{Be}$  and it is highly fragmented in  ${}^{10}\text{Be}$ . In contrast, the shape of the lower peak is almost same as that of  ${}^8\text{Be}$  indicating that excess neutrons do not affect so much the longitudinal mode. In the ground states of  ${}^9\text{Be}$  and  ${}^{10}\text{Be}$ , excess neutrons dominantly occupy the  $\pi$  orbits as discussed previously. The  $\pi$ -orbit neutrons are distributed in the transverse region, and therefore they affect only the transverse mode but not the longitudinal mode in the IVGDR strengths.

In the  $E < 20$  MeV region below the IVGDR energy, the low-energy IV dipole strengths appear in  ${}^9\text{Be}$  and  ${}^{10}\text{Be}$  because of the valence neutron motion against the  $2\alpha$  core. In  ${}^9\text{Be}$ , the low-energy IV dipole strengths are well separated from the IVGDR strengths and exhaust about 10% of the energy weighted sum of the calculated  $E1$  strengths (20% of the Thomas-Reiche-Kuhn sum rule). This result is consistent with the experimental strength distributions, though the calculation underestimates the width of the IVGDR (see Fig. 43 (d)). In  ${}^{10}\text{Be}$ , the strong IV dipole excitation is found at  $E \sim 15$  MeV. This IV dipole resonance is caused by the negative-parity excitation of the inter-cluster motion between  ${}^6\text{He}$  and  $\alpha$  clusters and regarded as the parity partner of the  $0^+$  state of the  ${}^6\text{He}+\alpha$  cluster resonance predicted in  $10 < E < 15$  MeV. In single-particle description, the  $E1$  strength from the ground state to the dipole resonance is enhanced remarkably by the coherent contribution of two valence neutrons.

It should be noted that there are low-lying states having relatively weak  $E1$  strengths,  ${}^9\text{Be}(1/2_1^+)$ ,  ${}^9\text{Be}(3/2_1^+)$ , and  ${}^9\text{Be}(5/2_1^+)$  in  $E < 5$  MeV and  ${}^{10}\text{Be}(1_1^-)$  in  $E < 10$  MeV. These low-lying states are dominated by single-particle excitations from the  $\pi_{3/2}$  orbit to the  $\sigma_{1/2}$  orbit in the molecular orbit configurations. Since the  $\pi_{3/2}$  and  $\sigma_{1/2}$  orbits have different node numbers for the transverse ( $n_\perp$ ) and longitudinal ( $n_z$ ) directions: the  $\pi_{3/2}$  orbit has node numbers  $(n_\perp, n_z) = (1, 0)$ , whereas the  $\sigma_{1/2}$  orbit has  $(n_\perp, n_z) = (0, 2)$ . From the difference in the node numbers, it is clear that  $E1$  transition is forbidden between these orbits.

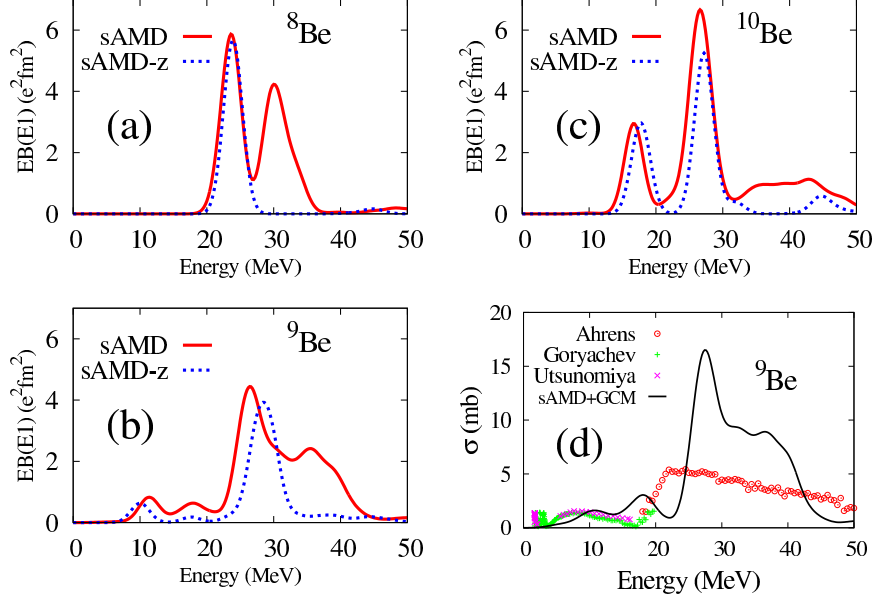


FIG. 43. Energy-weighted E1 strengths of (a) $^8\text{Be}$ , (b) $^9\text{Be}$ , and (c) $^{10}\text{Be}$  obtained by the sAMD calculations using the MV1 ( $m = 0.62$ ,  $b = h = 0$ ) central and G3RS ( $u_1 = -u_2 = -3000$  MeV) spin-orbit interactions. Results of the truncated calculations for the longitudinal mode (sAMD-z) are also shown. (d) The E1 cross sections of  $^9\text{Be}$  calculated by sAMD+ $\alpha$ GCM+cfg [265] compared with the experimental photonuclear cross sections. The experimental data are those by Ahrens *et al.* [286], Goryachev *et al.* [287], and Utsunomiya *et al.* [288]. The theoretical strengths are smeared by Gaussian with a width  $\gamma = 2$  MeV. Figures are taken from Ref. [265].

## 2. Isoscalar monopole and dipole excitations in $^{10}\text{Be}$

IS monopole excitations are more direct probes for cluster states because the IS monopole operator strongly excites the inter-cluster mode as discussed previously. The IS dipole excitations can be also useful probes to search for cluster states, because the IS dipole operator excites compressive modes similar to the IS monopole operator and it is expected to cause strong transitions into opposite parity cluster states [263, 264].

The IS monopole, E1, and IS dipole excitations from the  $^{10}\text{Be}$  ground state are investigated with the  $^6\text{He}+\alpha$  GCM model using the Volkov No.2 ( $m = 0.6$ ,  $b = h = 0.125$ ) central and G3RS ( $u_1 = -u_2 = -1600$  MeV) spin-orbit interactions. In the calculation, the inter-cluster distance  $R$  between  $^6\text{He}$  and  $\alpha$  is treated as the generator coordinate, and  $p$ -shell configurations of  $^6\text{He}$  are taken into account. At a moderate inter-cluster distance,

the  ${}^6\text{He}+\alpha$  GCM model describes approximately the molecular orbit configuration because of the antisymmetrization between single-particle wave functions. It also contains  ${}^6\text{He}+\alpha$  cluster resonances and discretized continuum in a finite box boundary,  $R \leq 15$  fm. The details of the  ${}^6\text{He}+\alpha$  GCM calculation are described in Refs. [169, 289]. The calculated IS monopole,  $E1$ , and IS dipole strengths are shown in Fig. 44.  ${}^6\text{He}+\alpha$  cluster resonances above the  $\alpha$ -decay threshold (10.1 MeV) are fragmented into several states because of coupling with discretized continuum states as well as channel coupling. Nevertheless, the IS monopole strengths are concentrated around  $E \sim 15$  MeV. The peak in the IS monopole strengths is dominantly contributed by the  ${}^6\text{He}(0^+)+\alpha$  resonance, whereas the broad distribution in  $E = 12 \sim 20$  MeV contains contributions from both  ${}^6\text{He}(0^+)+\alpha$  and  ${}^6\text{He}(2^+)+\alpha$  cluster resonances. It should be commented that the  ${}^6\text{He}(0^+)+\alpha$  and  ${}^6\text{He}(2^+)+\alpha$  channels can be excited by the IS monopole operator because both components are already contained in the  ${}^{10}\text{Be}$  ground state. In contrast to the significant IS monopole strengths for the cluster resonances, the IS monopole strength for the  $0_2^+$  state with the dominant  $\sigma_{1/2}^2$  configuration is relatively weak because the IS monopole operator does not excite the  $\sigma_{1/2}^2$  configuration from the ground state  $\pi_{3/2}^2$  configuration. The small but finite IS monopole strength for the  $0_2^+$  state originates in a minor component of  ${}^6\text{He}(0^+)+\alpha$  cluster mixed in the dominant  $\sigma_{1/2}^2$  configuration.

In the  $E1$  strength distribution, remarkable strengths in  $E = 10 - 20$  MeV correspond to the LEIVDR of the  ${}^6\text{He}+\alpha$  cluster mode, which is obtained at  $E \sim 15$  MeV in the sAMD calculation shown in Fig. 43 (b). In the  ${}^6\text{He}+\alpha$  GCM calculation, this IV dipole resonance spreads over the  $E = 10 - 20$  MeV region. From the point of view of neutron configurations, the enhanced  $E1$  strength for the  ${}^6\text{He}+\alpha$  cluster mode can be understood by coherent contributions of two valence neutrons around the  $2\alpha$ . For the lowest  $1^-$  state at  $E = 8$  MeV, which is assigned to the experimental  $1^-$  state at 5.96 MeV, the  $E1$  strength is relatively weak consistently with the sAMD result because the state is dominated by the  $\pi_{3/2}\sigma_{1/2}$  configuration, for which the  $E1$  transition is suppressed, as mentioned previously.

A more direct probe for negative-parity cluster resonances is the IS dipole excitation. Similarly to the IS monopole operator, the IS dipole operator contains the  $r^3$  term as the leading order contribution, and hence, the IS dipole strength is sensitively enhanced by the excitation of the inter-cluster motion. As expected, the IS dipole strengths are remarkable in  $E = 10 - 15$  MeV for the  ${}^6\text{He}+\alpha$  cluster resonances. Also for the  $1_1^-$  state at  $E = 8$  MeV, the

IS dipole strength is significant because of some mixing of the  ${}^6\text{He}+\alpha$  cluster component in the dominant  $\pi_{3/2}\sigma_{1/2}$  configuration in the  $1_1^-$  state. Consequently, the low-energy IS dipole strengths for the  ${}^6\text{He}+\alpha$  cluster mode are distributed in several states in the  $E = 5 - 15$  MeV region including the  $1_1^-$  state through the state mixing.

The present results indicate that the di-cluster resonances in  ${}^{10}\text{Be}$  shows the enhanced IS monopole,  $E1$ , and IS dipole strengths. Similar discussions of the enhanced IS monopole strengths for di-cluster resonances have been made for the  ${}^8\text{He}+\alpha$  cluster resonance in  ${}^{12}\text{Be}(0_3^+)$  by Ito *et al.* [290]. In contrast to the di-cluster resonances in highly excited states, the strengths to low-lying states are relatively suppressed because they are dominated by the particle-hole excitations in the molecular orbit configurations and have neutron configurations different from the initial ground states. In general, even though an excited state in neutron-rich nuclei has a developed cluster structure, the IS monopole and dipole strengths can be relatively weak if the excited state has an excited neutron configuration. It means that the IS monopole and dipole strengths are useful observables to identify excitation modes of cluster states; the single-particle excitation on the top of the cluster state or the excitation of the inter-cluster motion. We can conclude that the IS monopole and dipole strengths can be good probes for mode analysis of cluster states and also useful to discover new cluster states in neutron-rich nuclei as well as stable nuclei.

## VI. SUMMARY

In summary, we have reviewed the clustering phenomena in unstable nuclei from a point-of-view provided by the studies based on AMD. In particular, we put focus on the molecule-like states generated by the excess neutrons.

Whether the excess neutrons (protons) will reduce or enhance the clustering of unstable nuclei is non-trivial and important question, because the ordinary Ikeda threshold rule cannot be applied to unstable nuclei.

The AMD studies showed that all Be isotopes have  $2\alpha$  cluster core surrounded by the excess neutrons, and the degree of the  $2\alpha$  clustering (inter-cluster distance between  $2\alpha$  clusters) are changed depending on the neutron number. The clustering is first reduced toward  $N = 6$  system, but then, it is enhanced from  $N = 7$  system toward neutron drip line. It is also shown that the clustering plays an important role for the breaking of the neutron



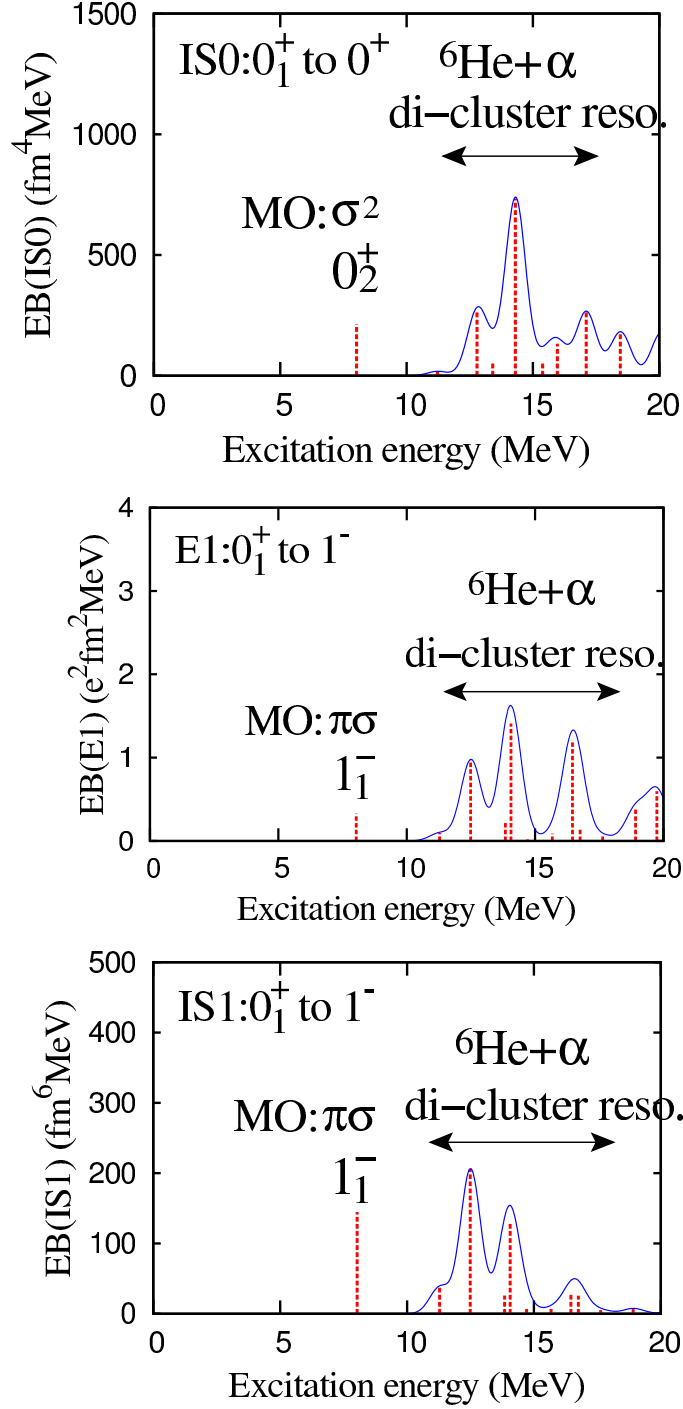


FIG. 44. IS monopole,  $E1$ , and IS dipole strengths of  $^{10}\text{Be}$  obtained by the  $^6\text{He}+\alpha$  cluster model calculation using the Volkov No.2 ( $m = 0.6$ ,  $b = h = 0.125$ ) central and G3RS ( $u_1 = -u_2 = -1600$  MeV) spin-orbit interactions [169, 289]. Energy weighted strengths are shown by dashed lines. For states above the  $\alpha$ -decay energy (10.1 MeV), energy weighted strength distributions,  $EB(IS0, E1, IS1)$ , smeared by Gaussian with  $\gamma = 1/\sqrt{\pi}$  MeV are shown by solid lines. The figures are taken from Ref. [289].

magic number  $N = 8$  in  $^{11}\text{Be}$  and  $^{12}\text{Be}$ . The B isotopes manifest more drastic change. The stable nucleus  $^{11}\text{B}$  has a compact shell model like ground state. But the addition of excess neutrons induces the clustering toward the neutron drip line. Thus, the excess neutrons reduce the clustering near the  $N = Z$  nuclei, but enhance it toward neutron drip line. It is pointed out that these reduction and enhancement of the clustering are well correlated to the behavior of the proton radii. The proton radii is also reduced near the  $N = Z$  nuclei, then it is increased toward the drip line. The experiments are now confirming this characteristic behavior of proton radii in Be and B isotopes.

The discussion is also extended to the Ne and Mg isotopes in which the breaking of the  $N = 20$  magic number is well known. By combining the AMD and the density-folding model, it is shown that the reaction cross section, the matter radii and quadrupole deformation are correlated to each other. They are reduced toward the  $N = 14$  and 16 isotones, then they are enhanced toward the island of inversion and the trend continues until the neutron drip line. The discontinuous behavior of the reaction cross section at  $N = 19$  isotones shows that the west border of the island of inversion is located at  $N = 19$ . On the other hand, no discontinuity was found in the neutron-rich side indicating that the island of inversion ( $N \simeq 20$ ) and the other region of deformation ( $N \simeq 28$ ) are merged. It is also noted that an extended version of AMD called AMD+RGM reasonably explains the observed reaction cross section of  $^{31}\text{Ne}$  and the formation of the neutron halo. Similar to the Be isotopes, the deformation change in Ne isotopes as function of neutron number is attributed to the clustering. By the estimation of the overlap between proton distributions, it is shown that the inter-cluster distance between  $\alpha$  and O clusters are reduced toward  $N = 16$ , but enlarged in the island of inversion. Again the AMD predicts that the proton radii is well correlated with the clustering.

Behind the change of the clustering in the ground states of unstable nuclei, the excess neutrons play the central role. The AMD studies showed the formation of the molecular-orbits around  $2\alpha$  cluster core in Be isotopes without any *a priori* assumption. The molecular-orbits are classified to so-called  $\pi$ - and  $\sigma$ -orbits. The former reduces the clustering, while the latter enhances it. The combinations of molecular-orbits naturally explain the reduction and enhancement of the clustering in Be isotopes mentioned above. In addition to the clustering of the ground states, the AMD study predicted many excited rotational bands with different configurations of excess neutrons, and showed that the concept of the molecular-orbits is

applicable and useful for the understanding of the excited states. By further increase of the excitation energy, the existence of the di-cluster bands is also predicted in which the excess neutrons are confined either of the clusters analogous to the ionic bonding of molecules.

The concept is also successful for the O, Ne and F isotopes. In the  $^{22}\text{Ne}$ , it is found that the excess neutrons in  $\sigma$ -orbit induce the clustering of the excited states. Analogous molecular-orbits are also predicted in O isotopes. Evolution of the molecular orbits in the island of inversion is examined in the F isotopes. It is pointed out that the cooperative effects of the clustering and the quenching of  $N = 20$  shell gap greatly reduce the energies of the molecular-orbit states near the neutron drip line of F isotopes. The extension of the molecular-orbit to the three center system is also discussed for the case of C isotopes. The linear-chain formation in  $^{14}\text{C}$  having the  $^{10}\text{Be} + \alpha$  intrinsic structure is predicted, which looks consistent with the recent observations. It is also found that the orthogonality effect is important for the stabilization of the linear chain.

We also discussed the monopole and dipole transitions as probe for nuclear clustering in the excited states. It was shown that the monopole and dipole transitions strongly and selectively populate the excited cluster states in the stable nuclei. To describe the monopole and dipole responses, an extended version of AMD named shifted-basis AMD is introduced. The application of the shifted-basis AMD to neutron-rich Be isotopes revealed that the coupling of the inter-cluster motion and valence neutrons yields novel types of the excitation modes.

## ACKNOWLEDGMENTS

We would like to thank A. Doté, Y. Taniguchi, A. Ono and H. Horiuchi for fruitful discussions and collaborations. Part of the numerical calculations were performed by using the supercomputers at RCNP in Osaka University, in the High Energy Accelerator Research Organization (KEK), and at Yukawa Institute for Theoretical Physics (YITP) in Kyoto University. The supports by the Grants-in-Aid for Scientific Research on Innovative Areas from MEXT Grant No. 2404:24105008 and JSPS KAKENHI Grant Nos. 16K05339, 26400270

and 15K17662 are acknowledged.

- 
- [1] K. Ikeda, H. Horiuchi, and N. Takigawa, Prog. Theor. Phys. Suppl. Extra Number **68**, 464 (1968).
  - [2] K. Wildermuth and C. Y. Tang, Unified Theory of the Nucleus, Clustering Phenomena in Nuclei (Vieweg, Braunschweig) (1977).
  - [3] Y. Fujiwara *et al.*, Prog. Theor. Phys. Suppl. **68**, 29 (1980).
  - [4] H. Furutani *et al.*, Prog. Theor. Phys. Suppl. **68**, 193 (1980).
  - [5] F. Michel, S. Ohkubo, and G. Reidemeister, Prog. Theor. Phys. Suppl. **132**, 7 (1998).
  - [6] T. Yamaya, K. Katori, M. Fujiwara, S. Kato, and S. Ohkubo, Prog. Theor. Phys. Suppl. **132**, 73 (1998).
  - [7] H. Horiuchi, Lecture Notes in Physics **818**, 57 (2010).
  - [8] I. Tanihata, H. Hamagaki, O. Hashimoto, Y. Shida, N. Yoshikawa, K. Sugimoto, O. Yamakawa, T. Kobayashi, and N. Takahashi, Phys. Rev. Lett. **55**, 2676 (1985).
  - [9] I. Tanihata, H. Savajols, and R. Kanungo, Prog. Part. Nucl. Phys. **68**, 215 (2013).
  - [10] O. Sorlin and M. G. Porquet, Prog. Part. Nucl. Phys. **61**, 602 (2008), arXiv:0805.2561 [nucl-ex].
  - [11] W. von Oertzen, Eur. Phys. J. **A11**, 403 (2001).
  - [12] H. Horiuchi, Proceedings of the 7th International Conference on Clustering Aspects of Nuclear Structure and Dynamics, ed. by M. Korolija, Z.A. Basrak and R. Caplar, 405 (2000).
  - [13] M. Seya, N. Kohno, and S. Nagata, Prog. Theor. Phys. **65**, 204 (1981).
  - [14] W. von Oertzen, Z. Phys. **A354**, 37 (1996).
  - [15] W. von Oertzen, Nuovo Cimento **110**, 895 (1997).
  - [16] W. von Oertzen and H. Bohlen, C. R. Physique **4**, 465 (2003).
  - [17] W. von Oertzen, M. Freer, and Y. Kanada-En'yo, Phys. Rep. **432**, 43 (2006).
  - [18] M. Freer, Rep. Prog. Phys. **70**, 2149 (2007).
  - [19] H. Morinaga, Phys. Rev. **101**, 254 (1956).
  - [20] H. Morinaga, Phys. Lett. **21**, 78 (1966).
  - [21] W. von Oertzen *et al.*, Eur. Phys. J. **A21**, 193 (2004).
  - [22] N. Itagaki, S. Okabe, K. Ikeda, and I. Tanihata, Phys. Rev. **C64**, 014301 (2001), arXiv:nucl-th/0103047 [nucl-th].

- [23] T. Suhara and Y. Kanada-En'yo, Phys. Rev. **C82**, 044301 (2010), arXiv:1004.4954 [nucl-th].
- [24] J. A. Maruhn, N. Loebl, N. Itagaki, and M. Kimura, Nucl. Phys. **A833**, 1 (2010).
- [25] T. Baba, Y. Chiba, and M. Kimura, Phys. Rev. **C90**, 064319 (2014), arXiv:1410.0789 [nucl-th].
- [26] M. Freer *et al.*, Phys. Rev. **C90**, 054324 (2014).
- [27] A. Fritsch *et al.*, Phys. Rev. **C93**, 014321 (2016).
- [28] Y. Kanada-En'yo, M. Kimura, and H. Horiuchi, Lecture Notes in Physics **818**, 129 (2010).
- [29] K. Ikeda *et al.*, Lecture Notes in Physics **818**, 165 (2010).
- [30] W. von Oertzen, Lecture Notes in Physics **875**, 147 (2014).
- [31] Y. Kanada-En'yo and H. Horiuchi, Prog. Theor. Phys. Suppl. **142**, 205 (2001), arXiv:nucl-th/0107044 [nucl-th].
- [32] Y. Kanada-En'yo, M. Kimura, and H. Horiuchi, Comptes Rendus Physique **4**, 497 (2003).
- [33] Y. Kanada-En'yo, M. Kimura, and A. Ono, PTEP **2012**, 01A202 (2012), arXiv:1202.1864 [nucl-th].
- [34] Y. Kanada-En'yo and H. Horiuchi, Prog. Theor. Phys. **93**, 115 (1995).
- [35] A. Volkov, Nucl. Phys. **74**, 33 (1965).
- [36] R. Tamagaki, Prog. Theor. Phys. **39**, 91 (1968).
- [37] T. Ando, K. Ikeda, and A. Tohsaki-Suzuki, Prog. Theor. Phys. **64**, 1608 (1980).
- [38] J. F. Berger, M. Girod, and D. Gogny, Comput. Phys. Comm. **63**, 365 (1991).
- [39] H. Feldmeier and J. Schnack, Rev. Mod. Phys. **72**, 655 (2000), arXiv:cond-mat/0001207 [cond-mat].
- [40] T. Neff and H. Feldmeier, Eur. Phys. J. Special Topics **156**, 69 (2008).
- [41] M. Kimura, Phys. Rev. **C69**, 044319 (2004), arXiv:nucl-th/0311062 [nucl-th].
- [42] Y. Kanada-En'yo, Phys. Rev. Lett. **81**, 5291 (1998), arXiv:nucl-th/0204039 [nucl-th].
- [43] D. L. Hill and J. A. Wheeler, Phys. Rev. **89**, 1102 (1953).
- [44] A. Dote, H. Horiuchi, and Y. Kanada-En'yo, Phys. Rev. **C56**, 1844 (1997).
- [45] Y. Kanada-En'yo, H. Horiuchi, and A. Ono, Phys. Rev. **C52**, 628 (1995).
- [46] K. Arai, Y. Ogawa, Y. Suzuki, and K. Varga, Phys. Rev. **C54**, 132 (1996), arXiv:nucl-th/9604009 [nucl-th].
- [47] Y. Ogawa, K. Arai, Y. Suzuki, and K. Varga, Nucl. Phys. **A673**, 122 (2000).
- [48] Y. Kanada-En'yo, H. Horiuchi, and A. Doté, Phys. Rev. **C60**, 064304 (1999),

- arXiv:nucl-th/9905048 [nucl-th].
- [49] N. Itagaki and S. Okabe, Phys. Rev. **C61**, 044306 (2000).
  - [50] N. Itagaki, S. Okabe, and K. Ikeda, Phys. Rev. **C62**, 034301 (2000), arXiv:nucl-th/0003059 [nucl-th].
  - [51] N. Itagaki, S. Hirose, T. Otsuka, S. Okabe, and K. Ikeda, Phys. Rev. **C65**, 044302 (2002), arXiv:nucl-th/0109039 [nucl-th].
  - [52] P. Descouvemont and D. Baye, Phys. Lett. **B505**, 71 (2001).
  - [53] P. Descouvemont, Nucl. Phys. **A699**, 463 (2002).
  - [54] Y. Kanada-En'yo, Phys. Rev. **C66**, 011303 (2002), arXiv:nucl-th/0204063 [nucl-th].
  - [55] Y. Kanada-En'yo and H. Horiuchi, Phys. Rev. **C66**, 024305 (2002), arXiv:nucl-th/0204041 [nucl-th].
  - [56] Y. Kanada-En'yo and H. Horiuchi, Phys. Rev. **C68**, 014319 (2003), arXiv:nucl-th/0301059 [nucl-th].
  - [57] M. Ito, K. Kato, and K. Ikeda, Phys. Lett. **B588**, 43 (2004), arXiv:nucl-th/0310037 [nucl-th].
  - [58] T. Neff and H. Feldmeier, *Clustering aspects of nuclear structure and dynamics. Proceedings, 8th International Conference, CLUSTER'03, Nara, Japan, November 24-29, 2003*, Nucl. Phys. **A738**, 357 (2004), arXiv:nucl-th/0312130 [nucl-th].
  - [59] K. Arai, Phys. Rev. **C69**, 014309 (2004).
  - [60] M. Ito, Phys. Lett. **B636**, 293 (2006), arXiv:nucl-th/0508032 [nucl-th].
  - [61] M. Ito, N. Itagaki, H. Sakurai, and K. Ikeda, Phys. Rev. Lett. **100**, 182502 (2008).
  - [62] T. Suhara and Y. Kanada-En'yo, Prog. Theor. Phys. **123**, 303 (2010), arXiv:0909.2218 [nucl-th].
  - [63] M. Dufour, P. Descouvemont, and F. Nowacki, Nucl. Phys. **A836**, 242 (2010).
  - [64] M. Ito, N. Itagaki, and K. Ikeda, Phys. Rev. **C85**, 014302 (2012).
  - [65] Y. Kanada-En'yo, Phys. Rev. **C85**, 044320 (2012), arXiv:1203.2398 [nucl-th].
  - [66] M. Ito and K. Ikeda, Rep. Prog. Phys. **77**, 096301 (2014).
  - [67] S. Hamada, M. Yasue, S. Kubono, M. H. Tanaka, and R. J. Peterson, Phys. Rev. **C49**, 3192 (1994).
  - [68] N. Soic *et al.*, Europhys. Lett. **34**, 7 (1996), arXiv:nucl-ex/9509001 [nucl-ex].
  - [69] N. Curtis, D. D. Caussyn, N. R. Fletcher, F. Marechal, N. Fay, and D. Robson,

- Phys. Rev. **C64**, 044604 (2001).
- [70] N. R. Fletcher, D. D. Caussyn, F. Marechal, N. Curtis, and J. A. Liendo, Phys. Rev. **C68**, 024316 (2003).
  - [71] N. Curtis, N. I. Ashwood, N. M. Clarke, M. Freer, C. J. Metelko, N. Soic, W. N. Catford, D. Mahboub, S. Pain, and D. C. Weissner, Phys. Rev. **C70**, 014305 (2004).
  - [72] S. Ahmed *et al.*, Phys. Rev. **C69**, 024303 (2004).
  - [73] M. Milin *et al.*, Nucl. Phys. **A753**, 263 (2005).
  - [74] M. Freer *et al.*, Phys. Rev. Lett. **96**, 042501 (2006).
  - [75] H. G. Bohlen, T. Dorsch, T. Kokalova, W. v. Oertzen, C. Schulz, and C. Wheldon, Phys. Rev. **C75**, 054604 (2007).
  - [76] N. Curtis *et al.*, J. Phys. **G36**, 015108 (2009).
  - [77] D. Suzuki *et al.*, Phys. Rev. **C87**, 054301 (2013).
  - [78] H. Bohlen *et al.*, Nuovo Cimento **A111**, 841 (1998).
  - [79] H. Bohlen *et al.*, Phys. Atom. Nucl. **65**, 603 (2002).
  - [80] A. A. Korshennikov *et al.*, Phys. Lett. **B343**, 53 (1995).
  - [81] M. Freer *et al.*, Phys. Rev. Lett. **82**, 1383 (1999).
  - [82] M. Freer *et al.*, Phys. Rev. **C63**, 034301 (2001), [Erratum: Phys. Rev. **C64**, 019904 (2001)].
  - [83] A. Saito *et al.*, Nucl. Phys. **A738**, 337 (2004).
  - [84] Z. H. Yang *et al.*, Phys. Rev. Lett. **112**, 162501 (2014).
  - [85] F. C. Barker, J. Phys. **G2**, L45 (1976).
  - [86] T. Suzuki and T. Otsuka, Phys. Rev. **C56**, 847 (1997).
  - [87] D. E. Alburger, D. P. Balamuth, J. M. Lind, L. Mulligan, K. C. Young, R. W. Zurmuhle, and R. Middleton, Phys. Rev. **C17**, 1525 (1978).
  - [88] H. T. Fortune, G. B. Liu, and D. E. Alburger, Phys. Rev. **C50**, 1355 (1994).
  - [89] H. Iwasaki *et al.*, Phys. Lett. **B481**, 7 (2000).
  - [90] H. Iwasaki *et al.*, Phys. Lett. **B491**, 8 (2000).
  - [91] A. Navin *et al.*, Phys. Rev. Lett. **85**, 266 (2000).
  - [92] S. Shimoura *et al.*, Phys. Lett. **B560**, 31 (2003).
  - [93] S. D. Pain *et al.*, Phys. Rev. Lett. **96**, 032502 (2006), arXiv:nucl-ex/0510048 [nucl-ex].
  - [94] N. Imai *et al.*, Phys. Lett. **B673**, 179 (2009).
  - [95] R. Meharchand *et al.*, Phys. Rev. Lett. **108**, 122501 (2012).

- [96] Y. Kanada-En'yo and H. Horiuchi, Phys. Rev. **C52**, 647 (1995).
- [97] G. Thiamova, N. Itagaki, T. Otsuka, and K. Ikeda, Eur. Phys. J. **A22**, 461 (2004).
- [98] Y. Kanada-En'yo, Phys. Rev. **C71**, 014310 (2005), arXiv:nucl-th/0408071 [nucl-th].
- [99] Y. Kanada-En'yo, Phys. Rev. **C91**, 014315 (2015), arXiv:1411.0765 [nucl-th].
- [100] Y. Kanada-En'yo and H. Horiuchi, Phys. Rev. **C55**, 2860 (1997).
- [101] H. Okuno *et al.*, Phys. Lett. **B354**, 41 (1995).
- [102] H. Ueno *et al.*, Phys. Rev. **C53**, 2142 (1996).
- [103] H. Izumi *et al.*, Phys. Lett. **B366**, 51 (1996).
- [104] H. Ogawa *et al.*, Phys. Rev. **C67**, 064308 (2003).
- [105] D. R. Tilley, J. H. Kelley, J. L. Godwin, D. J. Millener, J. E. Purcell, C. G. Sheu, and H. R. Weller, Nucl. Phys. **A745**, 155 (2004).
- [106] F. Ajzenberg-Selove and J. H. Kelley, Nucl. Phys. **A506**, 1 (1990).
- [107] W. Nortershauser *et al.*, Phys. Rev. Lett. **102**, 062503 (2009), arXiv:0809.2607 [nucl-ex].
- [108] A. Krieger *et al.*, Phys. Rev. Lett. **108**, 142501 (2012), arXiv:1202.4873 [physics.atom-ph].
- [109] T. Yamaguchi, I. Hachiuma, A. Kitagawa, K. Namihira, S. Sato, T. Suzuki, I. Tanihata, and M. Fukuda, Phys. Rev. Lett. **107**, 032502 (2011).
- [110] A. Estradé *et al.*, Phys. Rev. Lett. **113**, 132501 (2014).
- [111] S. Terashima *et al.*, PTEP **2014**, 101D02 (2014).
- [112] I. Angeli, At. Data Nucl. Data Tables **87**, 185 (2004).
- [113] L. V. Chulkov *et al.*, Nucl. Phys. **A674**, 330 (2000).
- [114] C. Thibault, R. Klapisch, C. Rigaud, A. M. Poskanzer, R. Prieels, L. Lessard, and W. Reisdorf, Phys. Rev. **C12**, 644 (1975).
- [115] G. Huber *et al.*, Phys. Rev. **C18**, 2342 (1978), [Erratum: Phys. Rev.C20,2457(1979)].
- [116] E. K. Warburton, J. A. Becker, and B. A. Brown, Phys. Rev. **C41**, 1147 (1990).
- [117] M. Kimura and H. Horiuchi, Prog. Theor. Phys. **107**, 33 (2002).
- [118] M. Kimura and H. Horiuchi, Prog. Theor. Phys. **111**, 841 (2004), arXiv:nucl-th/0404032 [nucl-th].
- [119] M. Kimura, Phys. Rev. **C75**, 041302 (2007), arXiv:nucl-th/0702012 [nucl-th].
- [120] M. Takechi *et al.*, Phys. Lett. **B707**, 357 (2012).
- [121] M. Takechi *et al.*, Phys. Rev. **C90**, 061305 (2014).
- [122] K. Marinova *et al.*, Phys. Rev. **C84**, 034313 (2011).



- [123] D. T. Yordanov *et al.*, Phys. Rev. Lett. **108**, 042504 (2012).
- [124] I. Angeli and K. P. Marinovab, At. Data Nucl. Data Tables **99**, 69 (2013).
- [125] T. Sumi, K. Minomo, S. Tagami, M. Kimura, T. Matsumoto, K. Ogata, Y. R. Shimizu, and M. Yahiro, Phys. Rev. **C85**, 064613 (2012), arXiv:1201.2497 [nucl-th].
- [126] S. Watanabe *et al.*, Phys. Rev. **C89**, 044610 (2014), arXiv:1404.2373 [nucl-th].
- [127] K. Minomo, T. Sumi, M. Kimura, K. Ogata, Y. R. Shimizu, and M. Yahiro, Phys. Rev. Lett. **108**, 052503 (2012), arXiv:1110.3867 [nucl-th].
- [128] T. Motobayashi *et al.*, Phys. Lett. **B346**, 9 (1995).
- [129] B. V. Pritychenko *et al.*, Phys. Lett. **B461**, 322 (1999), [Erratum: Phys. Lett. **B467**, 309 (1999)].
- [130] Y. Yanagisawa *et al.*, Phys. Lett. **B566**, 84 (2003).
- [131] H. Iwasaki *et al.*, Phys. Lett. **B620**, 118 (2005).
- [132] J. Gibelin *et al.*, Phys. Rev. **C75**, 057306 (2007).
- [133] B. Pritychenko, M. Birch, B. Singh, and M. Horoi, Atom. Data Nucl. Data Tabl. **107**, 1 (2016), arXiv:1312.5975 [nucl-th].
- [134] S. Raman, C. W. G. Nestor, Jr, and P. Tikkanen, Atom. Data Nucl. Data Tabl. **78**, 1 (2001).
- [135] K. Yoneda *et al.*, Phys. Lett. **B499**, 233 (2001).
- [136] A. Gade *et al.*, Phys. Rev. Lett. **99**, 072502 (2007).
- [137] C. Detraz, D. Guillemaud, G. Huber, R. Klapisch, M. Langevin, F. Naulin, C. Thibault, L. C. Carraz, and F. Touchard, Phys. Rev. **C19**, 164 (1979).
- [138] D. Guillemaud-Mueller, C. Detraz, M. Langevin, F. Naulin, M. de Saint-Simon, C. Thibault, F. Touchard, and M. Epherre, Nucl. Phys. **A426**, 37 (1984).
- [139] H. Horiuchi and K. Ikeda, Prog. Theor. Phys. **40**, 277 (1968).
- [140] M. Dufour, P. Descouvemont, and D. Baye, Phys. Rev. **C50**, 795 (1994).
- [141] R. Batchelor, A. J. Ferguson, H. E. Gove, and A. E. Litherland, Nucl. Phys. **16**, 38 (1960).
- [142] M. Girod and B. Grammaticos, Phys. Rev. **C27**, 2317 (1983).
- [143] M. Bender and P.-H. Heenen, Phys. Rev. **C78**, 024309 (2008), arXiv:0805.4383 [nucl-th].
- [144] K. Masaaki, Y. Ryosuke, and I. Masahiro, Prog. Theor. Phys. **127**, 287 (2012).
- [145] N. Fukunishi, T. Otsuka, and T. Sebe, Phys. Lett. **B296**, 279 (1992).
- [146] N. Hinohara, K. Sato, K. Yoshida, T. Nakatsukasa, M. Matsuo, and K. Matsuyanagi,

- Phys. Rev. **C84**, 061302 (2011), arXiv:1109.2060 [nucl-th].
- [147] J. M. Yao, H. Mei, H. Chen, J. Meng, P. Ring, and D. Vretenar, Phys. Rev. **C83**, 014308 (2011), arXiv:1006.1400 [nucl-th].
- [148] O. Sorlin *et al.*, Phys. Rev. **C47**, 2941 (1993).
- [149] B. Bastin *et al.*, Phys. Rev. Lett. **99**, 022503 (2007), arXiv:0705.4526 [nucl-ex].
- [150] C. Force *et al.*, Phys. Rev. Lett. **105**, 102501 (2010), arXiv:1007.4943 [nucl-ex].
- [151] D. Santiago-Gonzalez *et al.*, Phys. Rev. **C83**, 061305 (2011).
- [152] S. Takeuchi *et al.*, Phys. Rev. Lett. **109**, 182501 (2012), arXiv:1207.6191 [nucl-ex].
- [153] H. L. Crawford *et al.*, Phys. Rev. **C89**, 041303 (2014).
- [154] J. Retamosa, E. Caurier, F. Nowacki, and A. Poves, Phys. Rev. **C55**, 1266 (1997), arXiv:nucl-th/9608003 [nucl-th].
- [155] Z. P. Li, J. M. Yao, D. Vretenar, T. Niksic, H. Chen, and J. Meng, Phys. Rev. **C84**, 054304 (2011), arXiv:1209.6074.
- [156] M. Kimura, Y. Taniguchi, Y. Kanada-En'yo, H. Horiuchi, and K. Ikeda, Phys. Rev. **C87**, 011301 (2013).
- [157] Y. Utsuno, N. Shimizu, T. Otsuka, T. Yoshida, and Y. Tsunoda, Phys. Rev. Lett. **114**, 032501 (2015), arXiv:1407.0444 [nucl-th].
- [158] P. Doornenbal *et al.*, Phys. Rev. Lett. **111**, 212502 (2013).
- [159] P. Doornenbal *et al.*, Phys. Rev. **C93**, 044306 (2016).
- [160] K. Minomo, T. Sumi, M. Kimura, K. Ogata, Y. R. Shimizu, and M. Yahiro, Phys. Rev. **C84**, 034602 (2011), arXiv:1104.1856 [nucl-th].
- [161] D. M. Brink, Proc. Int. School of Physics Enrico Fermi, Course 36, Varenna, ed. C. Bloch (Academic Press, New York, 1966) (1966).
- [162] T. Yoshida, N. Shimizu, T. Abe, and T. Otsuka, *Proceedings, 3rd International Workshop on State of the Art in Nuclear Cluster Physics (SOTANCP3)*, J. Phys. Conf. Ser. **569**, 012063 (2014).
- [163] S. Okabe, Y. Abe, and H. Tanaka, Prog. Theory. Phys. **57**, 866 (1977).
- [164] S. Okabe, Y. Abe, and H. Tanaka, Prog. Theory. Phys. **59**, 315 (1978).
- [165] S. Okabe and Y. Abe, Prog. Theory. Phys. **61**, 1049 (1979).
- [166] Y. Kanada-En'yo, M. Kimura, and H. Horiuchi, *4th International Conference on Exotic Nuclei and Atomic Masses (ENAM 04) Callaway Gardens, Pine Mountain, Georgia, September*

- 12-16, 2004, Eur. Phys. J. **A25**, 305 (2005), arXiv:nucl-th/0410039 [nucl-th].
- [167] J. H. Kelley, E. Kwan, J. E. Purcell, C. G. Sheu, and H. R. Weller, Nucl. Phys. **A880**, 88 (2012).
- [168] S. Shimoura *et al.*, Phys. Lett. **B654**, 87 (2007).
- [169] Y. Kanada-En'yo and T. Suhara, Phys. Rev. **C85**, 024303 (2012), arXiv:1109.4293 [nucl-th].
- [170] F. Kobayashi and Y. Kanada-En'yo, Phys. Rev. **C86**, 064303 (2012), arXiv:1208.0387 [nucl-th].
- [171] D. R. Thompson, M. Lemere, and Y. C. Tang, Nucl. Phys. **A286**, 53 (1977).
- [172] A. N. Kuchera *et al.*, Phys. Rev. **C84**, 054615 (2011), [Erratum: Phys. Rev. **C88**, no.3, 039901(2013)], arXiv:1111.3341 [nucl-ex].
- [173] J. M. Eisenberg and W. Greiner, Nuclear Theory 1, Nuclear Models **A506** (1975).
- [174] Y. Kanada-En'yo, Y. Kawanami, Y. Taniguchi, and M. Kimura, Prog. Theor. Phys. **120**, 917 (2008).
- [175] Y. Kondo *et al.*, Phys. Lett. **B690**, 245 (2010).
- [176] A. Ostrowski, Z. Phys. **A343**, 489 (1992).
- [177] A. Belozerov *et al.*, Nucl. Phys. **A636**, 419 (1998).
- [178] M. Thoennessen, S. Yokoyama, and P. G. Hansen, Phys. Rev. **C63**, 014308 (2001).
- [179] J. L. Lecouey (LPC-CHARISSA-DEMON), *ECT\* International Workshop on Critical Stability of Few-Body Quantum Systems Trento, Italy, September 1-5, 2003*, Few Body Syst. **34**, 21 (2004), arXiv:nucl-ex/0310027 [nucl-ex].
- [180] H. Simon *et al.*, Nucl. Phys. **A734**, 323 (2004).
- [181] H. Simon *et al.*, Nucl. Phys. **A791**, 267 (2007).
- [182] H. Al Falou, A. Leprince, and N. A. Orr (LPC-CHARISSA-DEMON), in *International Symposium on Forefronts of Researches in Exotic Nuclear Structures: Niigata 2010 Tokamachi* (2010) arXiv:1004.3233 [nucl-ex].
- [183] H. T. Fortune and R. Sherr, Phys. Rev. **C82**, 064302 (2010).
- [184] G. Randisi *et al.*, Phys. Rev. **C89**, 034320 (2014), arXiv:1312.2360 [nucl-ex].
- [185] T. Suhara and Y. Kanada-En'yo, Phys. Rev. **C85**, 054320 (2012), arXiv:1203.1582 [nucl-th].
- [186] B. Roth and K. Wildermuth, Nucl. Phys. **20**, 10 (1960).
- [187] A. Arima, H. Horiuchi, and T. Sebe, Phys. Lett. **B24**, 129 (1967).
- [188] Y. Suzuki, Prog. Theor. Phys. **55**, 1751 (1976).

- [189] D. R. Tilley, H. R. Weller, and C. M. Cheves, Nucl. Phys. **A564**, 1 (1993).
- [190] D. R. Tilley, H. R. Weller, C. M. Cheves, and R. M. Chasteler, Nucl. Phys. **A595**, 1 (1995).
- [191] D. R. Tilley, C. M. Cheves, J. H. Kelley, S. Raman, and H. R. Weller, Nucl. Phys. **A636**, 249 (1998).
- [192] C. Wheldon *et al.*, Eur. Phys. J. **A26**, 321 (2005).
- [193] W. Scholz, P. Neogy, K. Bethge, and R. Middleton, Phys. Rev. Lett. **22**, 949 (1969).
- [194] W. Scholz, P. Neogy, K. Bethge, and R. Middleton, Phys. Rev. **C6**, 893 (1972).
- [195] G. V. Rogachev, V. Z. Goldberg, T. Lonnroth, W. H. Trzaska, S. A. Fayans, K. M. Kallman, J. J. Kolata, M. Mutterer, M. V. Rozhkov, and B. B. Skorodumov, Phys. Rev. **C64**, 051302 (2001).
- [196] N. Curtis, D. D. Caussyn, C. Chandler, M. W. Cooper, N. R. Fletcher, R. W. Laird, and J. Pavan, Phys. Rev. **C66**, 024315 (2002).
- [197] V. Z. Goldberg *et al.*, Phys. Rev. **C69**, 024602 (2004).
- [198] M. Kimura, Phys. Rev. **C75**, 034312 (2007).
- [199] P. Neogy, R. Middleton, and W. Scholz, Phys. Rev. **C6**, 885 (1972).
- [200] S. Y. Torilov *et al.*, Eur. Phys. J. **A47**, 158 (2011).
- [201] P. Descouvemont, Phys. Rev. **C38**, 2397 (1988).
- [202] M. Dufour and P. Descouvemont, Nucl. Phys. **A726**, 53 (2003).
- [203] M. Dufour and P. Descouvemont, Nucl. Phys. **A738**, 447 (2004).
- [204] N. Furutachi, S. Oryu, M. Kimura, A. Doté, and Y. Kanada-En'yo, Prog. Theor. Phys. **119**, 403 (2008), arXiv:0706.0145 [nucl-th].
- [205] W. von Oertzen *et al.*, Eur. Phys. J. **A43**, 17 (2010).
- [206] M. Gai, M. Ruscev, A. C. Hayes, J. F. Ennis, R. Keddy, E. C. Schloemer, S. M. Sterbenz, and D. A. Bromley, Phys. Rev. Lett. **50**, 239 (1983).
- [207] M. Gai, R. Keddy, D. A. Bromley, J. W. Olness, and E. K. Warburton, Phys. Rev. **C36**, 1256 (1987).
- [208] M. Gai, M. Ruscev, D. A. Bromley, and J. Olness, Phys. Rev. **C43**, 2127 (1991).
- [209] V. Z. Goldberg *et al.*, Phys. At. Nucl. **68**, 1079 (2005).
- [210] N. I. Ashwood *et al.*, J. Phys. **G32**, 463 (2006).
- [211] S. Yildiz *et al.*, Phys. Rev. **C73**, 034601 (2006).
- [212] E. D. Johnson *et al.*, Eur. Phys. J. **A42**, 135 (2009), arXiv:0906.3556 [nucl-ex].

- [213] M. L. Avila, G. V. Rogachev, V. Z. Goldberg, E. D. Johnson, K. W. Kemper, Yu. M. Tchuvil'sky, and A. S. Volya, Phys. Rev. **C90**, 024327 (2014), arXiv:1406.6734 [nucl-ex].
- [214] S. LaFrance, H. T. Fortune, S. Mordechai, M. E. Cobern, G. E. Moore, R. Middleton, W. Chung, and B. H. Wildenthal, Phys. Rev. **C20**, 1673 (1979).
- [215] M. Wiedeking *et al.*, Phys. Rev. Lett. **94**, 132501 (2005), arXiv:nucl-ex/0412028 [nucl-ex].
- [216] H. G. Bohlen *et al.*, Eur. Phys. J. **A47**, 44 (2011).
- [217] C. R. Hoffman *et al.*, Phys. Rev. **C85**, 054318 (2012).
- [218] M. Kimura and N. Furutachi, Phys. Rev. **C83**, 044304 (2011).
- [219] G. T. Kaschl, G. J. Wagner, G. Mairle, U. Schmidt-Rohr, and P. Turek, Nucl. Phys. **A155**, 417 (1970).
- [220] G. Mairle, G. J. Wagner, K. T. Knoepfle, L. K. Pao, H. Riedesel, V. Bechtold, and L. Friedrich, Nucl. Phys. **A363**, 413 (1981).
- [221] S. Michimasa *et al.*, Phys. Lett. **B638**, 146 (2006).
- [222] S. Shimoura, *NUSTAR 05: Nuclear Structure, Astrophysics and Reactions Surrey, England, January 5-8, 2005*, J. Phys. **G31**, S1759 (2005).
- [223] N. Frank *et al.*, Phys. Rev. **C84**, 037302 (2011).
- [224] J. K. Smith *et al.* (MoNA), Phys. Rev. **C86**, 057302 (2012).
- [225] Z. Elekes *et al.*, Phys. Lett. **B599**, 17 (2004).
- [226] H. Horiuchi, Prog. Theor. Phys. **51**, 1266 (1974).
- [227] H. Horiuchi, Prog. Theor. Phys. **53**, 447 (1975).
- [228] E. Uegaki, S. Okabe, Y. Abe, and H. Tanaka, Prog. Theor. Phys. **57**, 1262 (1977).
- [229] M. Kamimura, Nucl. Phys. **A351**, 456 (1981).
- [230] Y. Kanada-En'yo, Prog. Theor. Phys. **117**, 655 (2007), [Erratum: Prog. Theor. Phys.121,895(2009)], arXiv:nucl-th/0605047 [nucl-th].
- [231] T. Suhara, Y. Funaki, B. Zhou, H. Horiuchi, and A. Tohsaki, Phys. Rev. Lett. **112**, 062501 (2014), arXiv:1310.7684 [nucl-th].
- [232] W. von Oertzen, Z. Phys. **A357**, 355 (1997).
- [233] N. Itagaki, W. v. Oertzen, and S. Okabe, Phys. Rev. **C74**, 067304 (2006).
- [234] N. Furutachi and M. Kimura, Phys. Rev. **C83**, 021303 (2011).
- [235] P. W. Zhao, N. Itagaki, and J. Meng, Phys. Rev. Lett. **115**, 022501 (2015), arXiv:1410.3986 [nucl-th].

- [236] T. Suhara and Y. Kanada-En'yo, Phys. Rev. **C84**, 024328 (2011), arXiv:1103.1358 [nucl-th].
- [237] T. Baba and M. Kimura, (2016), arXiv:1605.05567 [nucl-th].
- [238] H. Yamaguchi *et al.*, (2016), arXiv:1610.06296 [nucl-ex].
- [239] Z. Y. Tian *et al.*, (2016), 10.1088/1674-1137/40/11/111001, arXiv:1607.00157 [nucl-ex].
- [240] D. Dell'Aquila *et al.*, Phys. Rev. **C93**, 024611 (2016).
- [241] S. Koyama *et al.*, Private communication.
- [242] P. J. Haigh *et al.*, Phys. Rev. **C78**, 014319 (2008).
- [243] F. Ajzenberg-Selove, Nucl. Phys. **A523**, 1 (1991).
- [244] Y. Kanada-En'yo, T. Suhara, and Y. Taniguchi, PTEP **2014**, 073D02 (2014), arXiv:1404.6016 [nucl-th].
- [245] T. Suhara and Y. Kanada-En'yo, Phys. Rev. **C91**, 024315 (2015), arXiv:1411.1240 [nucl-th].
- [246] N. Soic *et al.*, Phys. Rev. **C68**, 014321 (2003), arXiv:nucl-ex/0306018 [nucl-ex].
- [247] W. von Oertzen *et al.*, Eur. Phys. J. **A21**, 193 (2004).
- [248] D. L. Price *et al.*, Phys. Rev. **C75**, 014305 (2007).
- [249] J. D. Malcolm *et al.*, *Proceedings, Rutherford Centennial Conference on Nuclear Physics*, J. Phys. Conf. Ser. **381**, 012077 (2012).
- [250] P. Descouvemont and D. Baye, Phys. Rev. **C31**, 2274 (1985).
- [251] C. Fu *et al.*, Phys. Rev. **C77**, 064314 (2008).
- [252] M. Ito, *5th international Conference FUSION11 Saint Malo, France, May 2-6, 2011*, EPJ Web Conf. **17**, 07003 (2011).
- [253] T. Yamada, Y. Funaki, H. Horiuchi, I. K., and T. A., Prog. Theor. Phys. **120**, 1139 (2008).
- [254] T. Kawabata *et al.*, Phys. Lett. **B646**, 6 (2007), arXiv:nucl-ex/0512040 [nucl-ex].
- [255] M. Itoh *et al.*, Phys. Rev. **C84**, 054308 (2011).
- [256] M. Freer *et al.*, Phys. Rev. **C86**, 034320 (2012).
- [257] M. Itoh *et al.*, Phys. Rev. Lett. **113**, 102501 (2014).
- [258] T. Wakasa *et al.*, Phys. Lett. **B653**, 173 (2007), arXiv:nucl-ex/0611021 [nucl-ex].
- [259] T. Kawabata *et al.*, *Proceedings, 5th Asia-Pacific Conference on Few-Body Problems in Physics 2011 (APFB2011): Seoul, Korea, August 22-26, 2011*, Few Body Syst. **54**, 93 (2013).
- [260] M. Itoh *et al.*, Phys. Rev. **C88**, 064313 (2013), arXiv:1310.0169 [nucl-ex].
- [261] Z. H. Yang *et al.*, Phys. Rev. **C91**, 024304 (2015).

- [262] Y. Chiba and M. Kimura, Phys. Rev. **C91**, 061302 (2015), arXiv:1502.06325 [nucl-th].
- [263] Y. Chiba, M. Kimura, and Y. Taniguchi, Phys. Rev. **C93**, 034319 (2016), arXiv:1512.08214 [nucl-th].
- [264] Y. Kanada-En'yo, Phys. Rev. **C93**, 054307 (2016), arXiv:1512.03619 [nucl-th].
- [265] Y. Kanada-En'yo, Phys. Rev. **C93**, 024322 (2016), arXiv:1511.08530 [nucl-th].
- [266] P. Descouvemont and D. Baye, Phys. Rev. **C36**, 54 (1987).
- [267] A. Tohsaki, H. Horiuchi, P. Schuck, and G. Ropke, Phys. Rev. Lett. **87**, 192501 (2001), arXiv:nucl-th/0110014 [nucl-th].
- [268] Y. Funaki, A. Tohsaki, H. Horiuchi, P. Schuck, and G. Ropke, Phys. Rev. **C67**, 051306 (2003), arXiv:nucl-th/0302017 [nucl-th].
- [269] M. Chernykh, H. Feldmeier, T. Neff, P. von Neumann-Cosel, and A. Richter, Phys. Rev. Lett. **105**, 022501 (2010), arXiv:1004.3877 [nucl-ex].
- [270] Y. Suzuki and S. Hara, Phys. Rev. **C39**, 658 (1989).
- [271] T. Yamada, Y. Funaki, T. Myo, H. Horiuchi, K. Ikeda, G. Ropke, P. Schuck, and A. Tohsaki, Phys. Rev. **C85**, 034315 (2012), arXiv:1110.6509 [nucl-th].
- [272] Y. Suzuki, Nucl. Phys. **A470**, 119 (1987).
- [273] J. P. Elliott, Proc. Roy. Soc. Lond. **A245**, 128 (1958).
- [274] J. P. Elliott, Proc. Roy. Soc. Lond. **A245**, 562 (1958).
- [275] J. K. Perring and T. H. R. Skyrme, Proc. Roy. Soc. Lond. **69**, 600 (1956).
- [276] B. F. Bayman and A. Bohr, Nucl. Phys. **9**, 596 (1958/59).
- [277] D. H. Youngblood, Y. W. Lui, and H. L. Clark, Phys. Rev. **C55**, 2811 (1997).
- [278] D. H. Youngblood, H. L. Clark, and Y. W. Lui, Phys. Rev. **C57**, 1134 (1998).
- [279] Y. W. Lui, H. L. Clark, and D. H. Youngblood, Phys. Rev. **C64**, 064308 (2001).
- [280] X. Chen, Y. W. Lui, H. L. Clark, Y. Tokimoto, and D. H. Youngblood, Phys. Rev. **C80**, 014312 (2009).
- [281] Y. K. Gupta *et al.*, Phys. Rev. **C93**, 044324 (2016).
- [282] T. Peach *et al.*, Phys. Rev. **C93**, 064325 (2016).
- [283] D. H. Youngblood, Y. W. Lui, and H. L. Clark, Phys. Rev. **C57**, 2748 (1998).
- [284] B. John, Y. Tokimoto, Y. W. Lui, H. L. Clark, X. Chen, and D. H. Youngblood, Phys. Rev. **C68**, 014305 (2003).
- [285] Y. Kanada-En'yo, Phys. Rev. **C89**, 024302 (2014), arXiv:1308.0392 [nucl-th].

- [286] J. Ahrens *et al.*, Nucl. Phys. **A251**, 479 (1975).
- [287] A. Goryachev, G. Zalesnyy, I. Pozdnev, and I. Rossiiskoi, Akademii Nauk, Ser.Fiz. **56**, 159 (1992).
- [288] H. Utsunomiya, S. Katayama, I. Gheorghe, S. Imai, H. Yamaguchi, D. Kahl, Y. Sakaguchi, T. Shima, K. Takahisa, and S. Miyamoto, Phys. Rev. **C92**, 064323 (2015).
- [289] Y. Kanada-En'yo, Phys. Rev. **C94**, 024326 (2016), arXiv:1604.01453 [nucl-th].
- [290] M. Ito, Phys. Rev. **C83**, 044319 (2011).